Tampere University

Arttu Nieminen

EXCITON DYNAMICS IN TRANSITION METAL DICHALCOGENIDES EXCITED BY CYLINDRICALLY POLARISED LIGHT BEAMS

Master's thesis
Faculty of Engineering and Natural Sciences
Examiners: Asst. Prof. Marco Ornigotti
Dr. Godofredo Bautista
April 2022

ABSTRACT

Arttu Nieminen: Exciton dynamics in transition metal dichalcogenides excited by cylindrically polarised light beams
Master's thesis
Tampere University
Master's Programme in Science and Engineering
April 2022

In this thesis, we investigate the exciton dynamics in monolayer transition metal dichalcogenides (TMDs) when excited by cylindrically polarised light. We observe how the complex polarisation structure will excite transitions in the fine structure of exciton states in TMDs, also when an external magnetic field is present. Finally, we discuss how the tightly cylindrically polarised modes themselves could be used to create strong enough magnetic field needed to couple these dark excitons with light.

Our results indicate, that the co-rotating cylindrically polarised modes selectively excite the bright exciton bands, namely radially polarised beam only excites transitions rates into the linear light-like band and azimuthally polarised beam into the parabolic particle-like band, giving the possibility to control the exciton states with the choice of a polarisation mode. In the case when out-of-plane magnetic field is present, the spectrum of the parabolic band is broadened significantly, and, moreover, both co-rotating modes can excite both bands, contrary to the case when there is not an out-of-plane magnetic field.

When the in-plane magnetic field is present, we can excite transitions into the dark exciton states. The results lead to small amount of excitation of dark excitons, about 0.2% of the bright exciton amount, a similar result to other works done on brightening of dark excitons. The counter-rotating azimuthally polarised field has smaller total transition rate of the dark excitons compared to the co-rotating ones, whereas counter-rotating radially polarised field has a larger transition rate, but these differences are small. When the out-of-plane magnetic field is also taken into account, we disregard, for simplicity, the valley exchange interactions, and only look at the single valley optical response, which leads to all cylindrical polarisations having the same optical transitions, whose magnitude is about the same as when the out-of-plane magnetic field is not present.

Last, we discuss how the tightly focused cylindrically polarised modes can be used in creating the strong magnetic fields, which then could be used to brighten the dark exciton states and cause change in the optical transitions by the out-of-plane field. This, however, might be a challenging task, as the peak power needed for the optical pulse to create the strong enough magnetic fields could damage the TMD sample upon impact. The magnetic fields for these modes are larger than for uniformly polarised beams, though, and using them to brighten the dark excitons would be desirable.

This analysis is purely done in the paraxial approximation of optical fields. Future work would include doing the same analysis for nonparaxial fields, where we would need to redefine the vector potential, to account for the nonparaxiality of the field, and redo the calculations with that potential, which could lead to different results compared to the paraxial case.

Keywords: 2D materials, transition metal dichalcogenides, cylindrically polarised light, excitons, light-matter interaction

TIIVISTELMÄ

Arttu Nieminen: Eksitonien dynamiikka sylinterisymmetrisesti polarisoituneen valonsäteen virittämissä siirtymämetallidikalkogenideissa
Diplomityö
Tampereen yliopisto
Teknis-luonnontieteellinen DI-ohjelma
Huhtikuu 2022

Tässä työssä tutkimme eksitonien dynamiikkaa monokerroksisten sylinterisymmetrisesti polarisoituneitten valonsäteiden virittämissä siirtymämetallidikalkogenideissa (transition metal dichalcogenide, TMD), myös kun ulkoinen magneettikenttä on läsnä. Me myös katsomme mahdollisuutta käyttää voimakkaasti kohdennetun sylinterisymmetrisesti polarisoituneen valon magneettikentää tähän tarkoitukseen.

Tuloksemme näyttävät, että myötäpyörivät sylinterisymmetrisesti polarisoituneet valonsäteet valikoivat kumman eksitonin tilaa virittävät: Radiaalisesti polarisoitunut valo virittää vain lineaarista eksitonitilaa ja azimutaalisesti polarisoitunutta vain parabolista vastaavaa, antaen mahdollisuuden kontroilloida näiden tilojen populaatiota. Kun tason normaalinsuuntainen magneettikenttä on läsnä, silloin tämän parabolisen tilan optisen transition spektri levenee huomattavasti, sekä tässä tilanteessa molemmat myötäpyörivät polarisaatiot pystyvät virittämään tiloja siitä eksitoni tilasta, joihin eivät pystyneet ilman magneettikenttää. Zeeman-vuorovaikutus myös aiheuttaa näiden kahden eksitonitilan erkaantumisen, kun muuten nämä tilojen reunat olisivat samalla kohdalla.

Kun TMD-kerroksen määräämän tason suuntainen magneettikenttä on läsnä, pystymme virittämään myös pimeitä eksitonitiloja. Tämä johtaa pieneen viritysmäärään, noin 0.2% valkeiden tilojen vastaavasta, mikä on samanlainen tulos kuin muissakin vastaavissa julkaistuissa tutkimuksissa. Vastapyörivä azimutaalisesti polarisoitunut valo virittää himeman vähemmän ja radiaalisesti polarisoitunut hieman enemmän kuin myötäpyörivät vastaavat, mutta erot ovat pieniä. Silloin kun tason normaalisuuntainen magneettikenttä on myös läsnä, jätämme ottamatta laaksojen vaihtovuorovaikutukset huomioon, ja tarkastelemme vain yhdessä laaksossa tapahtuvia optisia virityksiä, jolloin kaikilla sylinterisymmersisillä polarisaatioilla on sama optinen transitiospektri, jonka suuruus on samaa luokkaa kuin ilman normaalisuuntaista magneettikenttää.

Lopuksi myös tutkimme kuinka voimakkaasti kohdennettua sylinterisymmetrisesti polarisoitunutta valoa voisi käyttää magneettikentän luonnissa. Tämän saavuttamiseen pitäisi käyttää lyhyttä valopulssia, jonka huipputeho tulisi olla todella korkea saavuttaakseen muutaman Teslan magneettikentän. Tämä saattaisi tuhota TMD-näytteen. Magneettikenttä on kuitenkin korkeampi näillä valonsäteillä kuin tasaisesti polarisoituneissa vastaavissa, joten tämän magneettikentän mahdollinen hyödyntäminen on kiinnostava tutkimuksen kohde.

Tässä työssä oletamme toimivamme paraksiaalisella valolla. Tulevaisuuden työssä voitaisiin käyttää epäparaksiaalista, fokusoitua valoa, jolloin vektoripotentiaali pitäisi määrittää uudelleen, ja laskut tehdä sillä, joka voisi johtaa erilaisiin tuloksiin paraksiaaliseen tilanteeseen verrattuna.

Avainsanat: 2D-materiaalit, siirtymämetallidikalkogenidit, sylinterisymmetrisesti polarisoitunut valo, eksitonit, valon ja aineen vuorovaikutus

PREFACE

I have had a great time working on theoretical optics in the Theoretical Optics and Photonics group of Tampere University. Huge thanks to my supervisor Marco Ornigotti for giving me the knowledge in physics and optics well beyond what we have been taught in the university courses, as well as supervising this thesis, giving me all the help I needed to finalise this work.

I also want to thank all my friends in- and outside the university, and last, but not least, special thanks go to my family.

Tampere, 19th April 2022

Arttu Nieminen

CONTENTS

1. Introduction 1
2. Transition metal dichalcogenides 3
2.1 Crystal structure of TMDs 3
2.2 Excitons in TMDs. 4
2.2.1 Bright excitons in TMDs 9
2.2.2 Bright exciton states in the presence of out-of-plane magnetic field . 10
2.2.3 Dark excitons in TMDs 11
2.3 Brightening of spin-dark exciton states in TMDs. 12
2.3.1 Brightened dark exciton states without the presence of out-of-plane magnetic field 14
2.3.2 Brightened dark exciton states in the presence of out-of-plane magnetic field 15
3. Paraxial optical beams and polarisation structures 16
3.1 Maxwell's equations and vector potentials 16
3.2 Paraxial optical beams 17
3.3 Angular spectrum of optical fields 19
3.4 Cylindrically polarised fields 21
4. Exciton-light interaction with cylindrically polarised beams 24
4.1 Exciton interaction with cylindrically polarised light. 24
4.2 Spectral functions of bright excitons excited by cylindrically polarised light . 26
4.3 Spectral functions of dark excitons excited by cylindrically polarised light . . 32
5. Tightly focused cylindrically polarised fields 37
5.1 Full vector solutions of tightly focused cylindrically polarised light 37
6. Conclusion and outlook 43
References 46
Appendix A: Exciton basis functions from second quantisation language 53
Appendix B: Calculating the expectation values of the interaction Hamiltonian . . . 55
Appendix C: Electric dipole approximation of the interaction Hamiltonian 56

LIST OF SYMBOLS AND ABBREVIATIONS

2D	Two-dimensional
3D	Three-dimensional
$\boldsymbol{\mathscr{A}}$	Vector potential
$\mathbf{B}$	Magnetic field
$\mathbf{B}_{\parallel}$	In-plane magnetic field
$\mathbf{B}_{\perp}$	Out-of-plane magnetic field
BSE	Bethe-Salpeter equation
$\hat{c}(\hat{c}^{\dagger})$	Annihilation (Creation) operator
c	Speed of light in vacuum
CPM	Cylindrically polarised mode
CVD	Chemical vapor decomposition
Δ	Bright and dark exciton splitting
δ	Dark and grey exciton splitting
$\mathbf{D}$	Dipole moment
d	Magnitude of dipole moment
$\delta(x)$	Dirac delta function
$\delta_{x,x'}$	Kronecker delta
DFT	Density-functional theory
E_g	Band gap
$\mathscr{E}$	Scalar electric field
$\boldsymbol{\mathscr{E}}$	Electric field vector
E	Energy
ϵ	Dielectric function
$\hat{\mathbf{f}}$	Polarisation unit vector
g	g-factor
$\mathscr{g}$	Exciton band spectral density function
$\|GS\rangle$	Semiconductor ground state

H_n	Hermite polynomial
$\hat{\mathbf{h}}_{\pm}$	Left (Right)-handed circular polarisation unit vector
HG	Hermite-Gaussian
$\mathbf{K}$	Transverse wavevector
$\{K, K', \Lambda\}$	Points of high symmetry in the Brillouin zone
ϕ	Angle of the transverse wave vector
$k_{\perp}$	Norm of the transverse wave vector
$\mathbf{k}$	Wavevector
k_0	Wavenumber
$\Lambda^S_{vc,\mathbf{Q}}(\mathbf{k})$	Electron-hole pair amplitude
$u^{HG}_{n,m}$	Hermite-Gaussian mode of order $n+m$, with horizontal index n and vertical index m
$u^{LG}_{\ell,p}$	Laguerre Gaussian mode with radial index p and azimuthal index ℓ
$L_p^{\lvert\ell\rvert}$	Generalised Laguerre polynomial
LG	Laguerre-Gaussian
LMI	Light-matter interaction
M	Transition metal atom
M_τ	Exciton effective mass
ML	Monolayer
Mo	Molybdenum
μ_B	Bohr magneton
μ	Radial/Azimuthal polarisation index
$\mathbb{N}_0$	Set of nonnegative integers
$\mathcal{N}$	Normalisation constant
$\nabla^2_{\perp}$	Transverse Laplacian operator
Ω	Area of TMD
ω	Frequency
OAM	Orbital angular momentum
$\lvert\psi_{n,\mathbf{k}}\rangle$	Quasiparticle Bloch-wavefunction
$\lvert\Psi^S_{\mathbf{Q}}\rangle$	Exciton state
ϕ_B	Polar angle of magnetic field
φ_Q	Polar angle of exciton center-of-mass momentum

$\hat{\mathbf{p}}$	Linear momentum operator
Q	Modulus of exciton center-of-mass momentum
$\mathbf{Q}$	Exciton center-of-mass momentum
$\mathbf{R}$	Transverse position vector
$\{r, \theta, z\}$	Cylindrical coordinates
r	Polar coordinate radius
$\mathbf{r}$	Position vector
S	Sulphur
SAM	Spin angular momentum
Se	Selenium
SOC	Spin-orbit coupling
SOI	Spin-orbit interaction
TAM	Total angular momentum
τ	Bright/Dark exciton index
TE	Transverse electric
Te	Tellurium
θ	Polar coordinate angle
TM	Transverse magnetic
TMD	Transition metal dichalcogenide
$\widetilde{u}$	Angular spectrum
u	Complex amplitude
$V_{\tau}^{\xi,\xi'}$	Valley exchange interaction potential
W	Tungsten
W	Transition rate of an exciton state
w_0	Beam waist
X	Chalcogen atom
$\{x, y, z\}$	Cartesian coordinates
$\{\hat{\mathbf{x}}, \hat{\mathbf{y}}, \hat{\mathbf{z}}\}$	Unit vectors of Cartesian coordinates
ξ	Valley index
$\mathbb{Z}$	Set of integers
z_R	Rayleigh range

1. INTRODUCTION

The discovery of atomically thin, two dimensional (2D) materials, prompted by the discovery of graphene in 2004 [1, 2], has raised massive interest in the academic research community, as their electronical, optoelectronical and optical properties cover a broad range of applications. Graphene alone exhibits extraordinary mechanical, thermal and optical qualities [3–5], and there also has already been discovered tens of another promising class of 2D materials, known as the transition metal dichalcogenides (TMDs) [6, 7], with varying electrical properties [8–11], and usually band gap situated in the optical or near infrared range. Group VI semiconducting TMDs, i.e., tungsten- and molybdenum-based compounds, are among the most studied compounds in the 2D class of materials, due to them sharing intriguing optical and electronic properties, especially in the valley and spin dynamics [12, 13]. TMDs have been known and researched for decades in their bulk and many layer form [8, 10], but the discovery of monolayer (ML) MoS_2 in 2010 [14], which was confirmed to be a direct band gap semiconductor, sparked renewal of interest in this class of materials, due to the physical properties of monolayer TMD differing so much from its bulk form, such as the aforementioned transition from indirect- to direct band gap, combined with the breaking of the inversion symmetry of the material [15, 16].

Light-matter interaction (LMI) has served a crucial part in understanding the optical and optoelectronical behaviour of TMDs. Moreover, the discovery of monolayer TMDs and their extraordinary properties, such as emerging of photoluminescence (PL) [17] and strong light-matter coupling [18–20] has given more reason to explore the possibilities of excitations with light in TMDs, to test the properties of TMDs predicted by theory and also discover new peculiar behaviours which could be used in optical applications. The PL spectra of various TMDs have been investigated under a magnetic field to optically otherwise inaccessible exciton states [21–27], as well as using phonons to assist indirect transitions [21, 28], revealing otherwise unseen states in TMD structure. Interaction with structured light has also been investigated in TMDs, like revealing the theoretically predicted light-like exciton band dispersion of the bright excitons in monolayer TMDs [29], and investigating the PL spectra of TMD heterostructures via cylindrically polarised beams [30], and also using the dark exciton states as source for the radially polarised beams [31]. To the author's knowledge, though, no works have yet done a theoretical investigation on how the cylindrically polarised vector beams interact with the fine structure of the

exciton states, which have been shown to be quite complex [32]. The complex polarisation structure of these beams could lead to interesting behaviour on the exciton dynamics, and the aim of this thesis is to explore this possibility.

The beams with nonuniform polarisation pattern across the transverse profile of the beam are under particular interest in the field of structured light research. The complex field configuration has been proven to give rise to many applications in various fields, one of few is their ability to generate strong axial electric [33] and magnetic [34] fields when focused. The research of these kind of beams are mainly concentrated on the cylindrically polarised modes (CPM), which in the paraxial approximation are given as a superposition of Hermite-Gaussian (HG) beams with linear polarisations which are orthogonal to each other [35], or, equivalently, Laguerre-Gaussian (LG) beams with orthogonal circular polarisation vectors, which can be either parallel or antiparallel to the topological charge of the orbital angular momentum (OAM) of an LG-beam, leading to different polarisation structures [36].

In this thesis, we investigate the light-matter interaction of cylindrically polarised light with TMDs, via looking at the excitations of the lowest-energy exciton states. The results show that the complex, nonuniform polarisation pattern leads to selective excitations of different exciton states, depending on which polarisation mode is employed. We also show, that when an external magnetic field is applied on the TMD monolayer, we have the possibility to excite otherwise optically inaccessible exciton states, thus leading to more complex transition rate spectrum, as the cylindrically polarised modes interact with the fine structure of TMD excitons. We also discuss the possibility of using tightly focused cylindrically polarised beam to provide the external magnetic field, as they have been shown to have such in their optical focus [36].

This thesis is organised as follows: In Chapter 2, we give an introduction to TMDs and all the relevant theoretical framework of their crystal structure, and describe their electronic and optical properties by the presence of stable excitons. Chapter 3 introduces the theory of paraxial light and the formation of cylindrically polarised fields via paraxial optical beams. Chapter 4 combines the last two chapters, and investigates fully how cylindrically polarised beams control the dynamics of excitons in TMDs, and how introducing a magnetic field can lead to more complex interactions and optical spectra. In Chapter 5, we discuss going beyond the paraxial beams and using tightly focused cylindrically polarised beams in the light-matter interaction of TMDs, particularly using the strong magnetic field it produces at its optical focus. Finally, in Chapter 6, we provide the conclusions and outlook based on the results given in this thesis, and discuss the possible future research on this topic.

2. TRANSITION METAL DICHALCOGENIDES

While graphene alone has attracted massive interest in the scientific community, its lack of a band gap and weak spin-orbit coupling (SOC) [37] limits its use in electronic and digital applications. However, the TMD family of materials provide more favourable electronic and optical properties, and they can be used to produce atomically thin electronic and photonic devices, such as field-effect transistors, light emitting diodes and photo detectors [6, 13, 38–40], to name a few.

In this chapter, we will first introduce the general crystal structure of TMDs, then we will discuss the excitons in TMDs and calculate both optically accessible and inaccessible exciton states and discuss how TMDs are characterised by their eigenenergies. Finally, we will show how the initially optically inaccessible states, namely the dark exciton states, can be coupled with light via external magnetic field, by mixing the eigenstates of bright and dark excitons.

2.1 Crystal structure of TMDs

TMD molecules are presented with a general chemical composition MX_2 , where M is a transition metal (e.g., Mo or W), and X is a chalcogen element (S,Se or Te) [41]. The transition metal layer is sandwiched between two planes of chalcogen atoms, where M atom is bonded by covalent forces to six X atoms [20]. Adjacent layers are vertically stacked together with weak van der Waals bonds [8]. A single layer of TMD forms a honeycomb lattice similar to graphene [42], leading to hexagonal Brillouin zone, with inequivalent K and K' valleys. A schematic view of the crystal structure of monolayer TMDs are shown in Fig. 2.1.

Monolayer TMDs are among the most intensively researched 2D materials. A technique to produce monolayers is to thin down a bulk- or multilayer TMD via chemical vapor deposition (CVD) [43]. In their bulk form, TMDs are indirect-gap semiconductors [44, 45], but when thinned down to a monolayer (ML), TMDs transform into a direct band gap material, situated in optical/near-infrared range [38, 46, 47], with conduction (valence) band minima (maxima) at the K and K' valleys, leading to massive rise in the optical absorption of the material [48], emerging of strong photoluminescence (PL) [17], and efficient light-matter coupling [18–20]. In contrast to graphene, monolayer TMDs have broken inversion

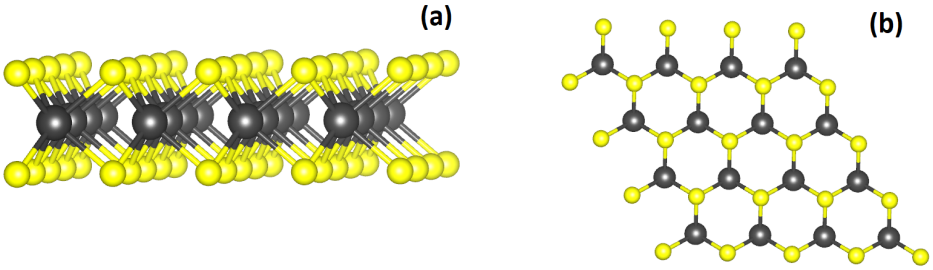

Figure 2.1. *Schematic view of the crystal structure of a monolayer TMD, with side view in panel (a) and top view in panel (b), which shows the hexagonal structure of the monolayer. Black atoms represent transition metals and yellow atoms chalcogens.*

symmetry and strong spin-orbit interaction (SOI) [15, 16], which lead to nontrivial, valley dependent optical selection rules, where electron only couples with left (right)-circularly polarised light at the K (K') valley, as well as lifting the spin degeneracy of the bands in these valleys, leading to fully spin-resolved conduction- and valence bands in both valleys, giving the possibility to access both the spin degree of freedom and the pseudospin of valley degree of freedom [49–52]. This gives the possibility to design spintronic [53, 54] and valleytronic [55, 56] devices, which exploit and control the spin- and valley- index of excitons. The valleys K and K' are related together via time-reversal symmetry, which leads to the bands having reversed order of spin splitting in the inequivalent valleys, called the spin-valley coupling [56]. When TMDs are in their 2D limit, the vertical confinement induces a strong coulomb interaction, which gives rise to possibility to excite quasiparticles, which are composed of bound states of a electron and a hole, called excitons [57], which will be discussed more detail in the next section.

2.2 Excitons in TMDs

An exciton is a quasiparticle composed of electrons and holes, which are strongly bound together by Coulomb interaction in hydrogen-like states [58–62]. These states can be thought of as intermediate states between the valence- and conduction band, where electron is excited into states where it is not free from the coulomb interaction coming from the vacancy of the electron, namely the hole. The same applies for the hole, as it cannot escape from the coulomb potential of the electron. This system resembles the aforementioned hydrogen-atom problem, which in the semiconductor physics is called the Wannier equation, whose solutions are the series of Rydberg-like excitonic quasiparticle states. With large enough excitation energy, the electron and hole become unbound, free particles, in the continuum of states in the conduction band. When the electron is excited into the exciton states, the electron and hole and bound together, and thus the composed quasiparticle itself is neutral, i.e., not a charge carrier. However, the electron-hole pair can also capture another electron or hole, which then forms a charged quasiparticle

called trion [61], which can act as an charge carrier, and also biexcitons can be formed, which are bound states of two neutral excitons [12]. These higher-order excitons are out of the scope of this thesis, and only single neutral excitons are considered from now on. The optical bandgap of a semiconductor is the energy needed to excite the lowest energy exciton state, namely the 1s-states [63], and the energy needed to excite electron in to the free and continuum of states in the conduction band is called the free particle bandgap, and the difference between the optical bandgap and the free particle bandgap is the exciton binding energy, indicating the strength of the bound state between the electron and hole. [12]

In three dimensional (3D) bulk semiconductors, exciton dynamics are not generally observed, because the exciton binding energy in them is of the order of meVs, which means that these states are unstable at room temperature. In the monolayer TMDs, the exciton binding energies are two orders of magnitude larger, several hundred meVs, leading to really stable excitons, even at room temperature [62, 64, 65]. Thus, for bulk semiconductors, the continuum of states are really close to the excitation energy of the exciton, whereas there is a huge gap between the continuum states and the first exciton states for monolayer TMDs, and this can be seen in the optical absorption spectra [12, 62]. Thus, the optical and optoelectronic properties of monolayer TMDs are dominated by the excitons. The reasons for much higher exciton binding energies are due to the spatial confinement, leading to strong Coulombic electron-electron and electron-hole interaction caused by the reduced dielectric screening [57]. The formulation of exciton states as Rydberg states, the reduced dielectric screening of a monolayer TMD and the optical absorption spectrum are illustrated in Fig. 2.2.

The complex electronic band strucure of TMDs gives rise to variety of exciton states, some of which are shown in Fig. 2.3: Intervalley excitons, where the electron and hole reside in the different valleys (K, K', Λ). These excitons are not optically active, as a photon does not carry enough momentum to excite these states, to preserve the conservation of momentum. These are called optically momentum-dark excitons, and one way to access these states is with assistance of phonons [21, 28]. In this thesis, we are not investigating phonon-assisted excitations, thus we will not consider momentum-dark excitons, but are described here for completeness. Other class of excitons are the intra-valley excitons, where the electron and hole reside in the same valley (K or K'). In this case, we can have the electron and hole with different spins (spin-unlike excitons), which corresponds to spin-dark exciton, because a spin flip is needed to induce this transition, which cannot be induced by photons [63]. Finally, when the electron and the hole are in the same valley, and have the same spin (spin-like excitons), the states are called bright exciton states, as they can be directly accessed by light, and are seen in optical spectra without any need of external fields [12]. The TMDs are characterised by the ordering of the conduction bands at the K and K' valleys, where the spin-up and spin-down sub-bands are separated by

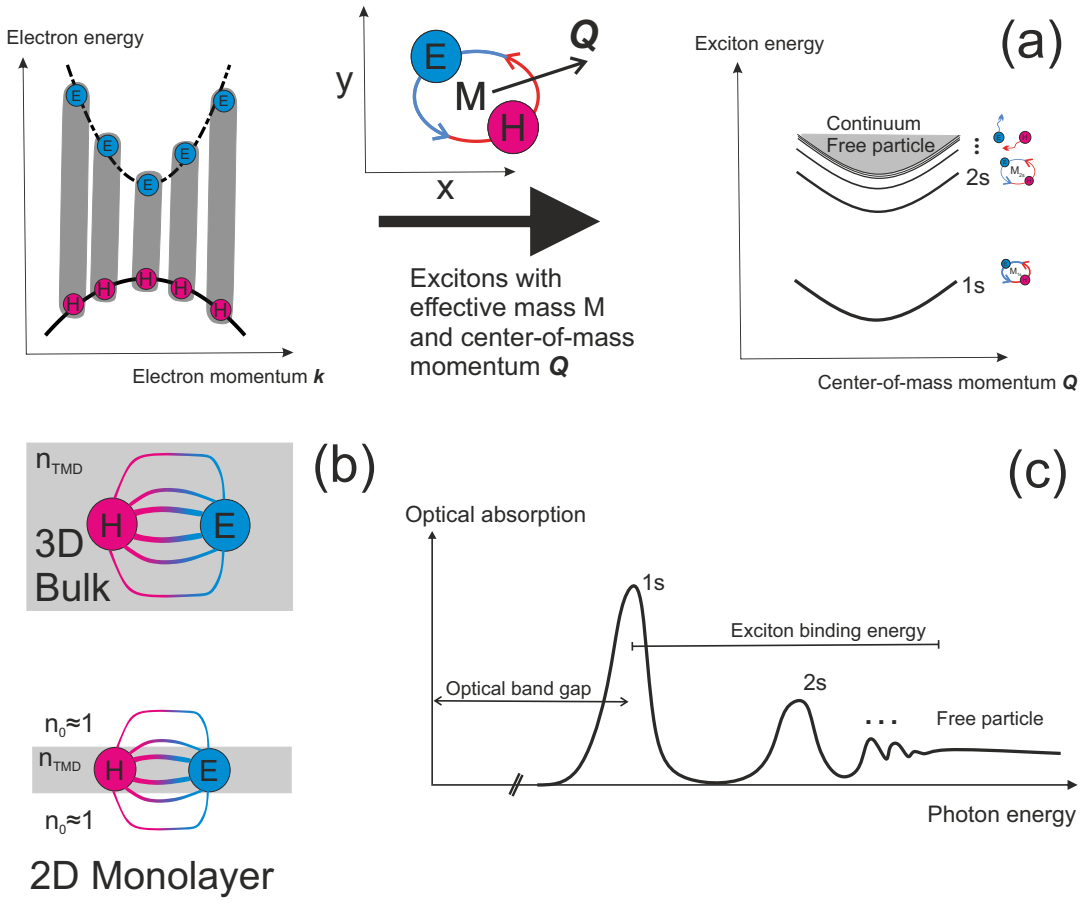

Figure 2.2. *(a) Schematic illustration of representing excitons as bound electrons and holes in the conduction and valence bands in left, and then changing the basis into Rydberg-like exciton states, with exciton effective mass M and center-of-mass momentum $\mathbf{Q}$. (b) Illustration of the reduced dielectric screening in monolayer TMD, compared to the one in bulk material, due to the electric field lines being completely in the TMD with high refractive index, significantly weakening the Coulomb force between the electron and hole. In monolayer TMDs, however, the field lines are mostly outside the TMD, in material with lower refractive index (e.g., air), thus the dielectric screening is much lower, and Coulomb interaction is stronger. (c) Schematic representation of the optical absorption in monolayer TMD. The absorption spectrum shows the excitation of the lowest energy bright exciton state "1s", which gives the optical band gap of the TMD. After that there are the rest of the Rydberg states, until reaching the free-particle bandgap, after which there is mostly constant absorption. The absorption in the continuum states is higher compared to the ones in 3D semiconductors due to the stronger Coulomb interaction, indicated in Ref. [12]. The binding energy of exciton is defined as the difference between the optical bandgap and the free-particle bandgap.*

a small SOI splitting term of the order of tens of meV. If the bottom conduction band has the same spin as the top valence band, the lowest-energy exciton is bright, otherwise it is dark. The former is the case in TMDs such as $MoSe_2$ [66] and $MoTe_2$ [67]. However, in some TMDs, e.g, WSe_2 [25, 68] and MoS_2 [22], the lowest energy exciton states are the spin-dark excitons, making them have a significant impact on the optical response, and the efficiency of light emission, thus accessing them is essential for TMD research. For the valence bands, the SOI splitting is order of magnitude larger, hundreds of meV [12, 63], thus we only consider the higher one of the valence bands, namely the spin-up(down) band in the K (K') valley.

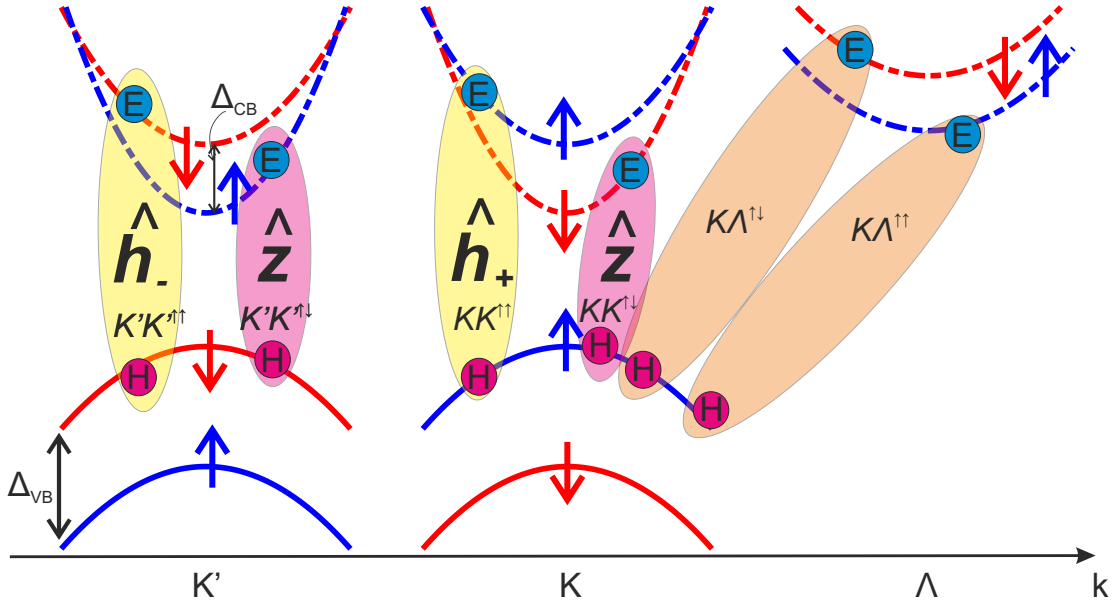

Figure 2.3. *Electronic band structure of a monolayer TMD in the points of high symmetry (K, K', Λ), and the optical selection rules for exciton transition, and formation of bright (yellow) excitons, spin-dark (red) excitons and momentum-dark (brown) excitons. The intravalley transitions between the bands with the same spin (like-spin transitions) are only excited by photons with in-plane circular polarisations $\hat{\mathbf{h}}_{\pm}$, whereas the transitions between different spins (unlike-spin transitions) are only excited by out-of-plane $\hat{\mathbf{z}}$-polarised photons. The spin-resolved bands are split by Δ_{VB} in the valence band, and Δ_{CB} in the conduction band, and Δ_{VB} is usually larger than Δ_{CB} by two orders of magnitude.*

As the bands in the K (K') valleys couple with circularly polarised light, accordingly, the dipole moments of the bright excitons are also circularly polarised, in the plane of the TMD layer, thus these excitons couple to light in the out-of-plane direction. The dark excitons have a transition dipole moment that causes spin-flips, which is polarised in the direction perpendicular to the TMD layer [23, 24]. Thus, there is radiative decay for these dark excitons along the TMD plane, but still, they are not optically active for light coming in with normal incidence, and, moreover, this out-of-plane dipole moment of dark excitons $d_{\perp}$ is weak, when compared to the strong in-plane dipole moments of bright excitons $d_{\parallel}$, indicated by their ratio $d_{\perp}/d_{\parallel} = 0.0035$ [24]. However, if the dark exciton is the lowest energy state, then, in low temperatures, even this low coupling of light can lead to considerable light emission due to much higher dark exciton population compared to bright ones, explained by Boltzmann statistics, assuming we are at the thermal equilibrium [25]. Fig. 2.3 gives the schematic picture of the electronic band structure of a monolayer TMD, and the possible formation of excitons in the bands. There are ways to couple spin-dark excitons with in-plane polarised light, by introducing mixing between the bright and dark exciton states via external fields, giving the possibility to observe them in PL spectra. This is discussed in more detail in Section 2.3.

The natural basis for describing exciton wavefunctions with center-of-mass momentum $\mathbf{Q}$ are written as coupled configurations of electron-hole pairs, in the language of second

quantisation, as follows [29, 69, 70]:

$$|\Psi^S_{\mathbf{Q}}\rangle = \frac{1}{\sqrt{\Omega}} \sum_{vc} \sum_{\mathbf{k}} \Lambda^S_{vc,\mathbf{Q}}(\mathbf{k}) \hat{c}^\dagger_{c,\mathbf{k}+\mathbf{Q}} \hat{c}_{v,\mathbf{k}} |GS\rangle, \tag{2.1}$$

where c and v denote the conduction and valence band, respectively, $\hat{c}$ and $\hat{c}^\dagger$ are the electron annihilation and creator operators, acting on the valence and conduction bands, respectively. $\Lambda^S_{vc,\mathbf{Q}}(\mathbf{k})$ is the amplitude of the electron-hole pair with a electron in the conduction band with wavevector $\mathbf{k}+\mathbf{Q}$ and a missing electron in the valence band with wavevector $\mathbf{k}$. $|GS\rangle$ is the ground state of the semiconductor, and Ω is the area of TMD material. These exciton states are interpreted as linear combination of free electron-hole pairs, where we remove an electron (i.e., create a hole) with wavevector $\mathbf{k}$ from the valence band via the annihilation operator $\hat{c}$, and then add an electron in the conduction band with wavevector $\mathbf{k}+\mathbf{Q}$ via creation operator $\hat{c}^\dagger$. The probability of creating an electron-hole pair for given wavevector $\mathbf{k}$ and center-of-mass momentum $\mathbf{Q}$ is determined by the amplitude term $\Lambda^S_{vc,\mathbf{Q}}(\mathbf{k})$.

The dipole moments of states in the same formalism are explicitly given as [29, 70]:

$$\frac{im_0 E_g}{e\hbar} \mathbf{D}^S_{\mathbf{Q}} \approx \frac{1}{\sqrt{\Omega}} \sum_{vc} \sum_{\mathbf{k}} \Lambda^S_{vc,\mathbf{Q}}(\mathbf{k}) \langle \psi_{v,\mathbf{k}} | \hat{\mathbf{p}} | \psi_{c,\mathbf{k}} \rangle, \tag{2.2}$$

where $|\psi_{n,\mathbf{k}}\rangle$ are the Bloch-wavefunctions of the quasiparticles in band n, E_g is the band gap of TMD, $\hat{\mathbf{p}}$ is the linear momentum operator, m_0 is the free electron mass, and e is the electron charge.

In general, exciton states are not described in their operator form given in Eq. (2.1). Instead, semi-analytical model of the exciton band structure in the K and K' valleys is used, assuming small exciton momentum $||\mathbf{Q}|| \ll 1$. These are determined by first solving the amplitude terms $\Lambda^S_{vc,\mathbf{Q}}(\mathbf{k})$ and the electron band energies in Bethe-Salpeter equation (BSE) via Density-functional theory (DFT)- and GW- based calculations and also using $\mathbf{k}\cdot\mathbf{p}$-expansion [7, 12, 63, 69–72] at the valleys of the Brillouin zone. These fitted models are then used in formulating the effective exciton band Hamiltonians and eigenstates, simplifying the analysis. In Appendix A, we show how the excitons states given in Eq. (2.1) into solving the amplitude terms $\Lambda^S_{vc,\mathbf{Q}}(\mathbf{k})$ in BSE, and finally deriving the effective form of the Hamiltonians as superposition of basis functions in the points of high symmetry, namely in valleys K and K', determined by the solutions of BSE.

In the next sections, our basis functions will be the single-valley excitons $|\Psi^\xi_{\tau,\mathbf{Q}}\rangle$, where $\xi = \{+,-\} \equiv \{K, K'\}$ is the valley index, and $\tau = \{b, d\}$ is the index separating bright and dark excitons. The effective Hamiltonians are derived by the aforementioned BSE solutions accompanied with $\mathbf{k}\cdot\mathbf{p}$-expansion and group theory analysis. We have, in general, four exciton functions as a basis, two at each valley, namely the bright and

dark excitons at K and K' valley, and thus, 4x4 effective Hamiltonian, which sometimes, depending on the situation, can be factored into 2x2 pseudospin Hamiltonians, if external potentials that couple the bright and dark excitons together are not present. More detailed description of these are given in Refs. [23, 24, 63, 70, 71, 73].

2.2.1 Bright excitons in TMDs

When working in the basis of intravalley exciton states, the first bright exciton states are given as intermixed states of $\{|\Psi^K_{b,\mathbf{Q}}\rangle, |\Psi^{K'}_{b,\mathbf{Q}}\rangle\}$, for which, in the presence of electron-hole exchange interaction, can be described by the following 2x2 pseudospin Hamiltonian [29]:

$$\hat{H}_b = \begin{pmatrix} E_0 + \frac{\hbar^2}{2M_b}Q^2 + V_b^{K,K} & V_b^{K,K'} \\ V_b^{K',K} & E_0 + \frac{\hbar^2}{2M_b}Q^2 + V_b^{K',K'} \end{pmatrix}, \tag{2.3}$$

where M_b is the bright exciton effective mass, $\mathbf{Q} = \{Q, \varphi_Q\}$ is the exciton center-of-mass momentum in polar coordinates, and E_0 is an arbitrary real-valued constant defining the zero-point of energy, i.e., the reference level. The terms $V_b^{\xi,\xi'}$ in the diagonal(antidiagonal) arise from the intra (inter)-valley exhcange interaction, and are explicitly given as $V_b^{K,K} = V_b^{K',K'} = \gamma Q$ and $V_b^{K,K'} = \left(V_b^{K',K}\right)^* = e^{-2i\varphi_Q}\gamma Q$, where $\gamma = 1.47$ eV $\cdot$ Å [29].

When solving the eigenvalues of (2.3), we see that first bright exciton states are split into two bands, when in presence of electron-hole exchange interaction, one with standard parabolic Q-dependence, $E^{\xi^-}_{\mathbf{Q}}$, and another one with almost linear dependence, $E^{\xi^+}_{\mathbf{Q}}$, distinguished by the pseudospin index $\xi^\pm$. These are called the particle-like and light-like energy dispersion bands, respectively [63]:

$$E^{\xi^-}_{b,\mathbf{Q}} = E_0 + \frac{\hbar^2 Q^2}{2M_b}, \tag{2.4a}$$

$$E^{\xi^+}_{b,\mathbf{Q}} \approx E_0 + 2\gamma Q, \tag{2.4b}$$

where we have neglected the quadratic term $\hbar^2 Q^2/2M_b$ in the linear band due to heavy effective mass of TMDs, of the order of an electron mass [26, 63]. The solved eigenstates are obtained as intermixed states of K and K' exciton states:

$$|\Psi^{\xi^-}_{b,\mathbf{Q}}\rangle = \frac{1}{\sqrt{2}}\big(|\Psi^K_{b,\mathbf{Q}}\rangle - e^{2i\varphi_Q}|\Psi^{K'}_{b,\mathbf{Q}}\rangle\big), \tag{2.5a}$$

$$|\Psi^{\xi^+}_{b,\mathbf{Q}}\rangle = \frac{1}{\sqrt{2}}\big(|\Psi^K_{b,\mathbf{Q}}\rangle + e^{2i\varphi_Q}|\Psi^{K'}_{b,\mathbf{Q}}\rangle\big), \tag{2.5b}$$

Dipole moments of the bright K and K' valley excitons, in monolayer TMDs, are polarised along the left- and right-handed circular polarisation unit vectors $\hat{\boldsymbol{h}}_\pm = (\hat{\mathbf{x}} \pm i\hat{\mathbf{y}})/\sqrt{2}$,

respectively [24, 29]: [1]

$$\mathbf{D}_b^{\xi} = \xi i\sqrt{2\Omega}\, d_{\parallel}\hat{\boldsymbol{h}}_{\xi}, \tag{2.6}$$

where $d_{\parallel} = 0.128|e|$. Now, in the case of E-H exchange interaction, similar to the eigenstates, the dipole moments of exciton states are given as intermixed of K and K' valley dipole moments:

$$\mathbf{D}_{b,\mathbf{Q}}^{\xi\pm} = \frac{1}{\sqrt{2}}\big(\mathbf{D}_b^{K} \pm e^{2i\varphi_Q}\mathbf{D}_b^{K'}\big) = i\sqrt{\Omega}\, d_{\parallel}\big(\hat{\boldsymbol{h}}_{+} \mp e^{2i\varphi_Q}\hat{\boldsymbol{h}}_{-}\big) \tag{2.7}$$

2.2.2 Bright exciton states in the presence of out-of-plane magnetic field

When an out-of-plane magnetic field is present, we need to add a term in the Hamiltonian to account for the interaction of the electron spin with the external magnetic field, leading to Zeeman shift term in our Hamiltonian [24]:

$$\hat{H}_b = \begin{pmatrix} E_0 + \frac{\hbar^2}{2M_b}Q^2 + V_b^{K,K} + g_b\mathscr{B}_{\perp} & V_b^{K,K'} \\ V_b^{K',K} & E_0 + \frac{\hbar^2}{2M_b}Q^2 + V_b^{K',K'} - g_b\mathscr{B}_{\perp} \end{pmatrix}, \tag{2.8}$$

where $\mathscr{B}_{\perp} = \mu_B|\mathbf{B}_{\perp}|/2$, where μ_B is the Bohr magneton. The Hamiltonian's eigenvalues are

$$E_b^{\xi^-} = \frac{\hbar^2}{2M_b}Q^2 + \gamma Q - \sqrt{(g_b\mathscr{B}_{\perp})^2 + \gamma^2Q^2}, \tag{2.9a}$$

$$E_b^{\xi^+} = \frac{\hbar^2}{2M_b}Q^2 + \gamma Q + \sqrt{(g_b\mathscr{B}_{\perp})^2 + \gamma^2Q^2}, \tag{2.9b}$$

and the eigenvectors are

$$\mathscr{N}_{b,\mathbf{Q}}^{\xi^-}|\Psi_{b,\mathbf{Q}}^{\xi^-}\rangle = \kappa_1(Q)|\Psi_{b,\mathbf{Q}}^{K}\rangle - e^{2i\varphi_Q}|\Psi_{b,\mathbf{Q}}^{K'}\rangle, \tag{2.10a}$$

$$\mathscr{N}_{b,\mathbf{Q}}^{\xi^+}|\Psi_{b,\mathbf{Q}}^{\xi^+}\rangle = |\Psi_{b,\mathbf{Q}}^{K}\rangle + \kappa_2(Q)e^{2i\varphi_Q}|\Psi_{b,\mathbf{Q}}^{K'}\rangle, \tag{2.10b}$$

where $\mathscr{N}_{b,\mathbf{Q}}^{\xi\pm}$ are the renormalisation constants, and

$$\kappa_1(Q) = \frac{\sqrt{(g_b\mathscr{B}_{\perp})^2 + \gamma^2Q^2} - g_b\mathscr{B}_{\perp}}{\gamma Q}, \tag{2.11a}$$

$$\kappa_2(Q) = \frac{\gamma Q}{\sqrt{(g_b\mathscr{B}_{\perp})^2 + \gamma^2Q^2} + g_b\mathscr{B}_{\perp}}, \tag{2.11b}$$

[1] Throughout this thesis, we are assuming the TMD layer to lie in the xy-plane.

where g_b is the bright exciton g-factor, which for MoS_2 is $g_b = -1.8$ [32]. and the dipole moments follow accordingly:

$$\mathscr{N}^{\xi^-}_{b,\mathbf{Q}}\mathbf{D}^{\xi^-}_{b,\mathbf{Q}} = i\sqrt{2\Omega}\, d_{\parallel}\big(\kappa_1 \hat{\boldsymbol{h}}_+ + e^{2i\varphi_Q}\hat{\boldsymbol{h}}_-\big), \tag{2.12a}$$

$$\mathscr{N}^{\xi^+}_{b,\mathbf{Q}}\mathbf{D}^{\xi^+}_{b,\mathbf{Q}} = i\sqrt{2\Omega}\, d_{\parallel}\big(\hat{\boldsymbol{h}}_+ - \kappa_2 e^{2i\varphi_Q}\hat{\boldsymbol{h}}_-\big). \tag{2.12b}$$

Note, that in the limit $|\mathbf{B}_\perp| = 0$ the equations above reduce into ones in Subsection 2.2.1, as they should.

2.2.3 Dark excitons in TMDs

The dark exciton Hamiltonian can be described, similarly to the bright exciton counterpart, with a 2x2 pseudospin Hamiltonian [24, 25, 63]:

$$\hat{H}_d = \begin{pmatrix} E_1 + \frac{\hbar^2}{2M_d}Q^2 + V_d^{K,K} & V_d^{K,K'} \\ V_d^{K',K} & E_1 + \frac{\hbar^2}{2M_d}Q^2 + V_d^{K',K'} \end{pmatrix}, \tag{2.13}$$

where $E_1 = E_0 - \Delta$, where Δ is the energy difference between the excitation energies of the bright and dark excitons, i.e., bright and dark exciton splitting energy. Now, in contrast to bright exciton Hamiltonian, the exchange interaction terms are not momentum-dependent, but a constant term instead, namely $V_d^{\xi,\xi'} = \delta/2$, which lift the valley degeneracy of dark excitons and mix the K and K' valleys in the eigenstates, leading to eigenvalues

$$E^{\xi^-}_{d,\mathbf{Q}} = \frac{\hbar^2}{2M_d}Q^2, \tag{2.14a}$$

$$E^{\xi^+}_{d,\mathbf{Q}} = \frac{\hbar^2}{2M_d}Q^2 + \delta, \tag{2.14b}$$

and the eigenstates corresponding to the eigenvalues are

$$|\Psi^{\xi^-}_{d,\mathbf{Q}}\rangle = \frac{1}{\sqrt{2}}\big(|\Psi^{K}_{d,\mathbf{Q}}\rangle - |\Psi^{K'}_{d,\mathbf{Q}}\rangle\big), \tag{2.15a}$$

$$|\Psi^{\xi^+}_{d,\mathbf{Q}}\rangle = \frac{1}{\sqrt{2}}\big(|\Psi^{K}_{d,\mathbf{Q}}\rangle + |\Psi^{K'}_{d,\mathbf{Q}}\rangle\big), \tag{2.15b}$$

and because the transition dipole moments of the dark excitons are $\mathbf{D}^{K(K')}_{d,\mathbf{Q}} = i\sqrt{\Omega}d_\perp\hat{\mathbf{z}}$, we see that the exchange interaction gives rise to one "grey" and one truly "dark" state:

$$\mathbf{D}^{\xi^-}_{d,\mathbf{Q}} = 0, \tag{2.16a}$$

$$\mathbf{D}^{\xi^+}_{d,\mathbf{Q}} = 2i\sqrt{\Omega}d_\perp\hat{\mathbf{z}}. \tag{2.16b}$$

Thus, the state with higher energy can couple to out-of-plane polarised light, and is called "grey", while the lower energy state is completely uncoupled from light, namely truly "dark".

2.3 Brightening of spin-dark exciton states in TMDs

The interplay between the first bright and dark exciton states and the exciton fine structure are important to understand, in order to effectively develop optoelectronic and valleytronic applications, as dark excitons might have a significant impact on the optical properties of TMDs, especially in the lower temperatures. In tungsten-based compounds, WS_2 and WSe_2, the lowest exciton state being dark is both theoretically well understood and experimentally verified [25, 32, 74], but for molybdenum-based ones, especially MoS_2, theoretical studies have arrived in conflicting and inconsistent results on the ordering of the spin-polarised conduction bands [63, 68, 71, 73, 75]. To experimentally confirm the ordering of the exciton states, one needs to be able to control photon emission from these states and observe the energies of the states from the PL spectrum, and recently, these kinds of experiments have managed to verify the ordering for some of these compounds [21, 22, 26, 66], but even these have had differing results, especially for MoS_2. For these experiments, one needs to be able to couple the dark excitons with light, and there are mechanisms to "brighten" the dark states, namely induce mixing between the dark and bright exciton states, which lead to relaxation of optical selection rules, and light emission can be observed from the dark states. One possibility is with an external out-of-plane electric field via Rashba-type coupling between the bright and dark states, which, however, has been proven to be weak in TMDs, resulting in negligible effect on radiative decay from dark excitons [23, 73]. More practical way is with an in-plane magnetic field via Zeeman coupling, which has been shown to have a noticeable effect on the PL spectra [21, 22, 24, 25]. Fig. 2.4 shows schematically the mixing of the bright and dark excitons due to external in-plane magnetic field, and the resulting modification in the PL spectrum.

The total Hamiltonian, in the basis $\{|\Psi^K_{b,\mathbf{Q}}\rangle, |\Psi^{K'}_{b,\mathbf{Q}}\rangle, |\Psi^K_{d,\mathbf{Q}}\rangle, |\Psi^{K'}_{d,\mathbf{Q}}\rangle\}$, in the presence of in-plane magnetic field $B_\parallel$ and out-of-plane magnetic field, is given in block-Hamiltonian form as follows:

$$\hat{H} = \begin{pmatrix} \hat{H}_b + \hat{H}_{b,Z_\perp} & \hat{H}_{Z_\parallel} \\ \hat{H}^\dagger_{Z_\parallel} & \hat{H}_d + \hat{H}_{d,Z_\perp} \end{pmatrix}, \tag{2.17}$$

where $\hat{H}_b$ is given by (2.3) and $\hat{H}_d$ is given by (2.13), and here, for simplicity, we impose $E_0 = \Delta$, which means that we have set the reference energy level at the dark exciton excitation energies.

The diagonal blocks $\hat{H}_{\tau,Z_\perp}$, where $\tau = \{b, d\}$ is the index separating bright and dark

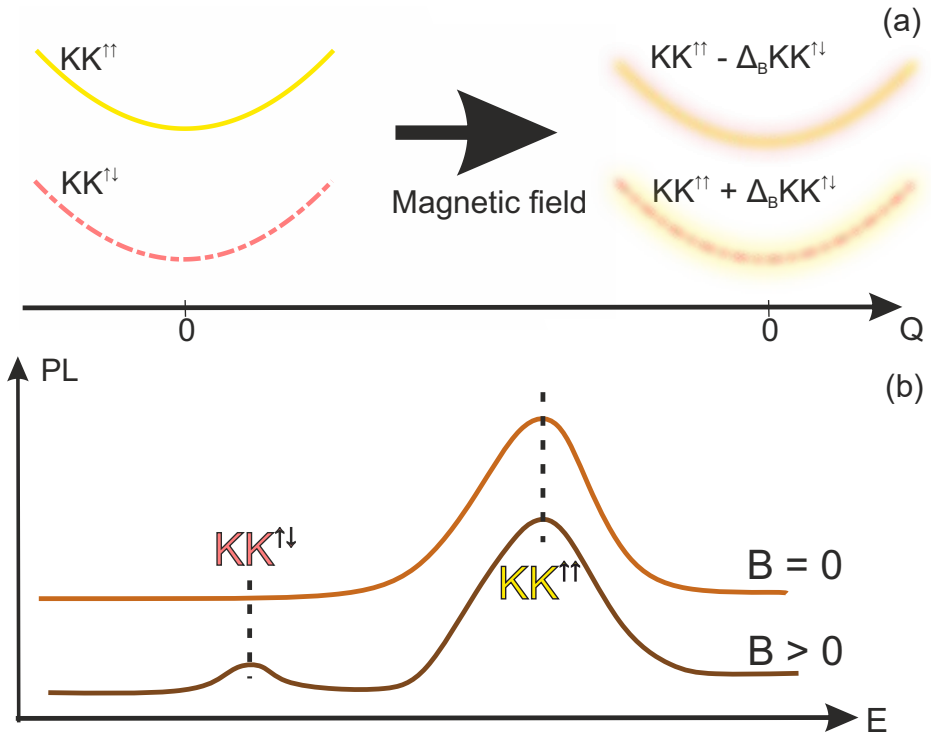

Figure 2.4. *Brightening of a spin-dark exciton via external magnetic field. Panel (a) shows schematically how the like-spin and unlike-spin single-valley states mix together in the presence of a (in-plane) magnetic field, indicated by the term Δ_B. Panel (b) shows how the PL spectra will be modified when magnetic field is applied in TMD, giving rise to an extra peak at the excitation energy of the dark exciton.*

excitons, describe the Zeeman shift term, which was described above, now interacting with electrons of both bright and dark excitons [24]:

$$\hat{H}_{\tau,Z_\perp} = \begin{pmatrix} g_\tau \mathscr{B}_\perp & 0 \\ 0 & -g_\tau \mathscr{B}_\perp \end{pmatrix}, \tag{2.18}$$

where g_d is now the dark exciton g-factor, which for MoS_2 is $g_d = -6.5$ [24].

Finally, the antidiagonal block $\hat{H}_{Z_\parallel}$ is the Zeeman coupling between the conduction band spin states, given rise by the in-plane magnetic field, and it is given by [24]

$$\hat{H}_{Z_\parallel} = \begin{pmatrix} g_\parallel \mathscr{B}_\parallel e^{-i\phi_B} & 0 \\ 0 & g_\parallel \mathscr{B}_\parallel e^{i\phi_B} \end{pmatrix}, \tag{2.19}$$

where $g_\parallel = 2$ is the in-plane conduction band g-factor [27], $\mathscr{B}_\parallel = \mu_B |\mathbf{B}_\parallel|/2$ and $\phi_B = \arg\{|\mathbf{B}_x| + i|\mathbf{B}_y|\}$. This Zeeman coupling term gives rise to the mixing of the bright and dark exciton states, leading to the possibility of coupling in-plane polarised light with otherwise dark excitons.

2.3.1 Brightened dark exciton states without the presence of out-of-plane magnetic field

We now assume that out-of-plane magnetic field is absent, i.e., $|\mathbf{B}_\perp| = 0$, thus we neglect $\hat{H}_{\tau,Z_\perp}$ terms in Eq. (2.17). Still, for the simplicity of our analysis, we will consider the Zeeman coupling term in (2.17) as a perturbative Hamiltonian on the free Hamiltonian composed by $\hat{H}_b$ and $\hat{H}_d$, giving small correction terms on the energies and eigenstates of free bright exciton states given by Eqs. (2.4) and (2.5), and dark excitons states given by Eqs. (2.14) and (2.15).

We will be limiting our scope to the first-order corrections to the free exciton states, for which the corrections to the energies are zero, and the mixed dark exciton eigenstates are

$$\widetilde{\mathcal{N}}^{\xi^-}_{d,\mathbf{Q}}|\widetilde{\Psi}^{\xi^-}_{d,\mathbf{Q}}\rangle = |\Psi^{\xi^-}_{d,\mathbf{Q}}\rangle + \big(-\alpha(\mathbf{Q})|\Psi^{K}_{b,\mathbf{Q}}\rangle + \alpha(\mathbf{Q})^*|\Psi^{K'}_{b,\mathbf{Q}}\rangle\big), \tag{2.20a}$$

$$\widetilde{\mathcal{N}}^{\xi^+}_{d,\mathbf{Q}}|\widetilde{\Psi}^{\xi^+}_{d,\mathbf{Q}}\rangle = |\Psi^{\xi^+}_{d,\mathbf{Q}}\rangle + \big(\beta(\mathbf{Q})|\Psi^{K}_{b,\mathbf{Q}}\rangle + \beta(\mathbf{Q})^*|\Psi^{K'}_{b,\mathbf{Q}}\rangle\big), \tag{2.20b}$$

where the renormalisation constants $\widetilde{\mathcal{N}}^{\xi^\pm}_{d,\mathbf{Q}} \approx 1$, and $\alpha(\mathbf{Q})$ and $\beta(\mathbf{Q})$ are explicitly given as

$$\alpha(\mathbf{Q}) = g_\parallel \mathscr{B}_\parallel \frac{e^{-i\phi_B}\left(\Delta + \nu Q^2 + \gamma Q\right) + e^{i\phi_B}\gamma Q e^{-2i\varphi_Q}}{\sqrt{2}\left(\Delta + \nu Q^2\right)\left(\Delta + \nu Q^2 + 2\gamma Q\right)}, \tag{2.21a}$$

$$\beta(\mathbf{Q}) = g_\parallel \mathscr{B}_\parallel \frac{-e^{-i\phi_B}\left(\Delta_1 + \nu Q^2 + \gamma Q\right) + e^{i\phi_B}\gamma Q e^{-2i\varphi_Q}}{\sqrt{2}\left(\Delta_1 + \nu Q^2\right)\left(\Delta_1 + \nu Q^2 + 2\gamma Q\right)}, \tag{2.21b}$$

where $\nu = \frac{\hbar^2}{2}(1/M_b - 1/M_d)$, and $\Delta_1 = \Delta - \delta$.

We can now determine the transition dipole moments of these brightened states, given by

$$\widetilde{\mathcal{N}}^{\xi^-}_{d,\mathbf{Q}}\widetilde{\mathbf{D}}^{\xi^-}_{d,\mathbf{Q}} = i\sqrt{2\Omega}\, d_\parallel\big(-\alpha(\mathbf{Q})\hat{\boldsymbol{h}}_+ - \alpha(\mathbf{Q})^*\hat{\boldsymbol{h}}_-\big), \tag{2.22a}$$

$$\widetilde{\mathcal{N}}^{\xi^+}_{d,\mathbf{Q}}\widetilde{\mathbf{D}}^{\xi^+}_{d,\mathbf{Q}} = 2i\sqrt{\Omega} d_\perp \hat{\mathbf{z}} + i\sqrt{2\Omega}\, d_\parallel\big(\beta(\mathbf{Q})\hat{\boldsymbol{h}}_+ - \beta(\mathbf{Q})^*\hat{\boldsymbol{h}}_-\big), \tag{2.22b}$$

We would get similar results for the corrected bright states, but, for the moment, we are only interested in the brightened dark excitons, thus we will not report them here. In the first order approximation, the energies of these mixed states are the same as the ones for free bright and dark excitons, and the second order corrections would be of magnitude $(g_\parallel \mu_B \mathscr{B}_\parallel)^2/\Delta \ll 1$, even for large magnetic fields like $|\mathbf{B}| = 30$ T. However, the modulus of the mixing terms $|\alpha(\mathbf{Q})|$ and $|\beta(\mathbf{Q})|$ are of order $g_\parallel \mu_B \mathscr{B}_\parallel/\Delta$, which, although pretty small, are considerably higher than the shift in energies and mix the bright and dark exciton states, leading to in-plane dipole moments for brightened dark excitons which are

comparable to the dark exciton out-of-plane dipole moments [23]. As mentioned above, due to the much larger thermal population of dark excitons in some TMDs, this coupling leads to photon emission from the dark exciton states which can be observed in the PL spectra [21, 22, 25, 27].

2.3.2 Brightened dark exciton states in the presence of out-of-plane magnetic field

We now consider the case where out-of-plane magnetic field is present. However, for the simplicity of our analysis, we will only consider one valley at a time, thus neglecting the terms $V_\tau^{\xi,\xi'}$ in Eqs. (2.3) and (2.13). In this case, the valleys are decoupled from each other, so we can factor out the valley degree of freedom by introducing single valley bright and dark excitons $|\Psi_\tau^\xi\rangle$, and consider only the 2x2 single-valley Hamiltonian

$$\hat{H}^\xi = \begin{pmatrix} \Delta + \frac{\hbar^2}{2M_b}Q^2 + \xi g_b \mathscr{B}_\perp & g_\parallel \mathscr{B}_\parallel e^{-\xi i\phi_B} \\ g_\parallel \mathscr{B}_\parallel e^{i\xi\phi_B} & \frac{\hbar^2}{2M_d}Q^2 + \xi g_d \mathscr{B}_\perp \end{pmatrix}. \tag{2.23}$$

We simplify this problem further and consider the in-plane magnetic field term $g_\parallel \mathscr{B}_\parallel$ perturbatively, leading to free Hamiltonian to be in diagonalised form, with eigenvalues given by the diagonal terms:

$$E_b^\xi = \Delta + \frac{\hbar^2}{2M_b}Q^2 + \xi g_b \mathscr{B}_\perp, \tag{2.24a}$$

$$E_d^\xi = \frac{\hbar^2}{2M_d}Q^2 + \xi g_d \mathscr{B}_\perp, \tag{2.24b}$$

and trivially, corresponding eigenstates are $|\Psi_b^\xi\rangle$ and $|\Psi_d^\xi\rangle$, respectively.

We again limit ourselves to first-order corrections, where the eigenvalues remain unchanged, and the corrected dark state is

$$\widetilde{\mathscr{N}}_{d,\mathbf{Q}}^\xi |\widetilde{\Psi}_d^\xi\rangle = |\Psi_d^\xi\rangle + \Delta_B^\xi |\Psi_b^\xi\rangle, \tag{2.25}$$

where, again, $\widetilde{\mathscr{N}}_{d,\mathbf{Q}}^\xi \approx 1$, and

$$\Delta_B^\xi(\mathbf{Q}) = \frac{-g_\parallel \mathscr{B}_\parallel e^{-\xi i\phi_B}}{\nu Q^2 + \Delta + \xi(g_b - g_d)\mathscr{B}_\perp} \tag{2.26}$$

Thus, the dipole moment of this brightened single-valley dark state is

$$\widetilde{\mathscr{N}}^\xi \widetilde{\mathbf{D}}_{d,\mathbf{Q}}^\xi = 2i\sqrt{\Omega} d_\perp \hat{\mathbf{z}} + \xi i\sqrt{2\Omega}\, d_\parallel \Delta_B^\xi \hat{\boldsymbol{h}}_\xi. \tag{2.27}$$

3. PARAXIAL OPTICAL BEAMS AND POLARISATION STRUCTURES

In this chapter, we will cover the paraxial beam modes which satisfy the scalar Helmholtz equation, namely the Hermite-Gaussian (HG) and Laguerre-Gaussian (LG) solutions. These solutions are then used to define the cylindrically polarised vector beams as superpositions of these modes accompanied with suitable polarisation vectors. We also look at plane wave expansions of optical fields, namely the angular spectrum representation, which will be used in the next chapter for LG beams.

3.1 Maxwell's equations and vector potentials

Electric and magnetic fields must satisfy Maxwell's equations. They can also be described conveniently in terms of a vector potential $\boldsymbol{\mathscr{A}}$ and a scalar potential Φ. Maxwell's equations, and other properties of an electromagnetic field, such as interaction with matter, can be described by these potentials. These potentials do not uniquely determine the electric and magnetic field, but belong to a equivalence class of gauge functions that are related to each other via gauge transformation. Imposing conditions for these electromagnetic potentials is called gauge fixing. [76, 77]

The basis of classical theory of electromagnetic field is given by the Maxwell's equations, which in the vaccuum, are given as follows [76–78]:

$$\nabla \cdot \boldsymbol{\mathscr{E}} = 0, \tag{3.1a}$$

$$\nabla \times \boldsymbol{\mathscr{E}} = -\frac{\partial \mathbf{B}}{\partial t}, \tag{3.1b}$$

$$\nabla \cdot \mathbf{B} = 0, \tag{3.1c}$$

$$\nabla \times \mathbf{B} = \frac{1}{c^2}\frac{\partial \boldsymbol{\mathscr{E}}}{\partial t}, \tag{3.1d}$$

where $\boldsymbol{\mathscr{E}}$ is the electric field, $\mathbf{B}$ is the magnetic field, and c is the speed of light in vacuum. In Coulomb gauge, electric and magnetic field are defined solely in terms of a vector potential $\boldsymbol{\mathscr{A}}$ [76, 77]:

$$\boldsymbol{\mathscr{E}} = -\frac{\partial \boldsymbol{\mathscr{A}}}{\partial t}, \tag{3.2a}$$

$$\mathbf{B} = \nabla \times \boldsymbol{\mathscr{A}}, \tag{3.2b}$$

and, by inserting Eq. (3.2a) and (3.2b) into (3.1a) and (3.1d), we have

$$\nabla \cdot \boldsymbol{\mathscr{A}} = 0 \tag{3.3a}$$

$$\nabla^2 \boldsymbol{\mathscr{A}} - \frac{1}{c^2}\frac{\partial^2 \boldsymbol{\mathscr{A}}}{\partial t^2} = 0. \tag{3.3b}$$

In the Coulomb gauge, the vector potential $\boldsymbol{\mathscr{A}}$ is completely transverse, and it satisfies the wave equation by Eq. (3.3b). Therefore, the vector potential has the form of a harmonic wave.

Vector potential for a monochromatic, time harmonic electromagnetic field can be written as $\boldsymbol{\mathscr{A}}(\mathbf{r}, t) = \mathbf{A}(\mathbf{r})e^{-i\omega t}$, where $\mathbf{r}$ is the position vector, ω is the frequency, and t is the time. Inserting this into Eq. (3.2a), we have that $\boldsymbol{\mathscr{E}}(\mathbf{r}, t) = i\omega\boldsymbol{\mathscr{A}}(\mathbf{r}, t)$, i.e., the electric field and the vector potential are related together via a multiplicative constant $i\omega$. Inserting this definition of vector potential into Eq. (3.3b), we see that $\mathbf{A}(\mathbf{r})$ must satisfy the Helmholtz equation: [79]

$$\nabla^2 \mathbf{A}(\mathbf{r}) + k_0^2 \mathbf{A}(\mathbf{r}) = 0, \tag{3.4}$$

where $k_0 = c\,\omega$ is the wavenumber.

3.2 Paraxial optical beams

A particular class of solutions to the Helmholtz equation (3.4) are the so-called paraxial optical beams, i.e., fields which propagate primarily in a fixed direction, usually denoted as the z-direction. In this case, the vector potential associated to that field can be written as

$$\mathbf{A}(\mathbf{r}) = A_0 u(\mathbf{r}) e^{ik_0 z}\hat{\mathbf{f}}, \tag{3.5}$$

where A_0 is the amplitude, and $\hat{\mathbf{f}} = \{f_x, f_y\}$ is a unit vector determining the polarisation. These optical beams can be intuitively seen as plane waves propagating in z-direction, but instead of a constant complex amplitude, the transverse profile is determined by the complex envelope $u(\mathbf{r})$. By substituting (3.5) into Eq. (3.4), we obtain

$$\nabla_\perp^2 u(\mathbf{r}) + 2ik_0\frac{\partial u(\mathbf{r})}{\partial z} + \frac{\partial^2 u(\mathbf{r})}{\partial z^2} = 0, \tag{3.6}$$

where $\nabla_\perp^2$ is the transverse Laplacian operator. Assuming that the field is paraxial, i.e.,

$$\left|\frac{\partial^2 u(\mathbf{r})}{\partial z^2}\right| \ll k_0 \left|\frac{\partial u(\mathbf{r})}{\partial z}\right|, \nabla_\perp^2 u(\mathbf{r}), \tag{3.7}$$

we obtain the paraxial Helmholtz equation:

$$\nabla_\perp^2 u(\mathbf{r}) + 2ik_0 \frac{\partial u(\mathbf{r})}{\partial z} = 0. \tag{3.8}$$

In the Cartesian coordinates $\mathbf{r} = \{x, y, z\}$, the solutions satisfying (3.8) are given as Hermite-Gaussian (HG) modes of order $M = n + m$: [79, 80]

$$u_{n,m}^{HG}(\mathbf{r}) = \mathscr{N}_{n,m}^{HG} \frac{w_0}{w(z)} H_n\left(\frac{\sqrt{2}x}{w(z)}\right) H_m\left(\frac{\sqrt{2}y}{w(z)}\right) e^{-\frac{x^2+y^2}{w^2(z)} + ik_0\frac{x^2+y^2}{2R(z)} - i(1+n+m)\varphi(z)}, \tag{3.9}$$

where $\mathscr{N}_{n,m}^{HG} = \sqrt{\frac{2}{2^{n+m} n! m! \pi w_0^2}}$, $H_n(u)$ are the Hermite polynomials of order n [81]. Other parameters are the beam width $w(z)$, wavefront curvature $R(z)$, Gouy phase $\varphi(z)$ and Rayleigh range z_R, which are defined as follows:

$$w(z) = w_0\sqrt{1 + z^2/z_R^2} \tag{3.10a}$$

$$R(z) = z(1 + z_R^2/z^2) \tag{3.10b}$$

$$\varphi(z) = \arctan(z/z_R) \tag{3.10c}$$

$$z_R = k_0 w_0^2/2 \tag{3.10d}$$

where w_0 is the Gaussian beam waist, namely the beam width at $z = 0$, which defines all the other parameters, along with the wavenumber k_0. HG beams are the complete set of orthogonal solutions to the Helmholtz equation, namely they span the whole paraxial domain, which means that every paraxial beam can be presented as a superposition of solutions defined by (3.9), with different n and m.

There is an alternative family of orthogonal solutions that span the whole paraxial beam domain, which are the solutions of the Helmholtz equation in the cylindrical coordinates $\mathbf{r} = \{r, \theta, z\}$, and these are the Laguerre-Gaussian (LG) modes, given as follows: [79, 80]

$$u_{\ell,p}^{LG}(\mathbf{r}) = \mathscr{N}_{\ell,p}^{LG} \frac{w_0}{w(z)} \left[\frac{\sqrt{2}r}{w(z)}\right]^{|\ell|} L_p^{|\ell|}\left(\frac{2r^2}{w^2(z)}\right) e^{-\frac{r^2}{w^2(z)} + ik_0\frac{r^2}{2R(z)} + i\ell\theta - i(1+2p+|\ell|)\varphi(z)}, \tag{3.11}$$

where $\mathscr{N}_{\ell,p}^{LG} = \sqrt{\frac{2p!}{\pi w_0^2 (p+|\ell|)!}}$, $L_p^{|\ell|}(u)$ is the generalised Laguerre polynomial [81], defined by the radial index $p \in \mathbb{N}_0$ and the azimuthal index $\ell \in \mathbb{Z}$ (also known as the topological charge).

As both HG and LG beams form a complete set of orthogonal solutions for paraxial beams in free space, we can present any LG beam as a linear superposition of HG beams and vice versa. In particular, it can be shown that LG solutions $u^{LG}_{\pm 1,0}$ are equivalent to superposition of first order HG modes $u^{HG}_{1,0}$ and $u^{HG}_{0,1}$:

$$u^{LG}_{\pm 1,0} = \frac{1}{\sqrt{2}}(u^{HG}_{1,0} \pm i u^{HG}_{0,1}), \tag{3.12}$$

and, equivalently, HG modes in terms of LG modes are given as follows:

$$u^{HG}_{1,0} = \frac{1}{\sqrt{2}}(u^{LG}_{1,0} + u^{LG}_{-1,0}) \tag{3.13a}$$

$$u^{HG}_{0,1} = \frac{-i}{\sqrt{2}}(u^{LG}_{1,0} - u^{LG}_{-1,0}). \tag{3.13b}$$

Eqs. (3.12) and (3.13) will be useful when defining the cylindrically polarised fields, which are described as superposition of HG or LG beams with suitable polarisation vectors. With these equations, we can change from the HG representation to LG representation of cylindrically polarised beams and vice versa.

3.3 Angular spectrum of optical fields

Plane wave is the simplest solution to the Maxwell's equation, which, however, is unphysical, as it has infinite energy due to the constant amplitude in the transverse profile [76]. However, due to their simple nature, they still have important uses in describing electromagnetic fields, as many optical phenomena are explained by how a single plane wave is affected. Moreover, we can take an arbitrarily shaped optical beam, and describe it by a suitable linear superposition of plane waves, namely describe the beam in the form of angular spectrum representation [82]. In angular spectrum representation, the optical field is presented in the reciprocal space, namely the $\mathbf{k}$-space, describing the field as a sum of plane waves with different $\mathbf{k}$-vector.

We now assume a paraxial scalar electric field $\mathscr{E}(\mathbf{r}) = u(\mathbf{r})e^{ik_0 z}$, satisfying the paraxial Helmholtz equation (3.8), at an arbitrary constant point z. We expand our wave $\mathscr{E}(\mathbf{r})$ as a superposition of plane waves by taking a 2D Fourier transform in the transverse space:

$$\widetilde{\mathscr{E}}(\mathbf{K}, z) = \frac{1}{(2\pi)^2} \iint_{\mathbf{R}} \mathrm{d}^2 R\, E(\mathbf{r}) e^{-i\mathbf{K}\cdot\mathbf{R}}, \tag{3.14}$$

where $\mathbf{R} = \{r, \theta\}$ and $\mathbf{K} = \{k_\perp, \phi\}$ are the position- and wave-vectors in the transverse plane, respectively, in the cylindrical coordinates, and $\mathrm{d}^2 R = r\mathrm{d}r\mathrm{d}\theta$. The original field is

obtained through the inverse Fourier transform:

$$\mathscr{E}(\mathbf{r}) = \iint\limits_{\mathbf{K}} \mathrm{d}^2K\, \widetilde{\mathscr{E}}(\mathbf{K}, z) e^{i\mathbf{K}\cdot\mathbf{R}}, \tag{3.15}$$

where $\mathrm{d}^2K = k_\perp \mathrm{d}k_\perp \mathrm{d}\phi$. By inserting (3.15) into Eq. (3.8), and defining

$$k_z = \sqrt{k_0^2 - k_\perp^2} = k_0 \left(1 - \frac{k_\perp^2}{2k_0^2}\right) + \mathcal{O}(k_\perp^4), \tag{3.16}$$

we notice, that, in order to satisfy Helmholtz equation (3.4), the z-dependence of the Fourier spectrum is given as follows:

$$\widetilde{\mathscr{E}}(\mathbf{K}, z) = \widetilde{\mathscr{E}}(\mathbf{K}, 0) e^{ik_z z}. \tag{3.17}$$

Inserting (3.17) into (3.15), we obtain the angular spectrum representation of a paraxial field:

$$\mathscr{E}(\mathbf{r}) = \iint\limits_{\mathbf{K}} \mathrm{d}^2K\, \widetilde{\mathscr{E}}(\mathbf{K}, 0) e^{i\mathbf{K}\cdot\mathbf{R} + ik_0\left(1 - \frac{k_\perp^2}{2k_0^2}\right)z}. \tag{3.18}$$

To obtain the angular spectrum representation of a given field $E(\mathbf{r})$, we need to calculate its Fourier transform by Eq. (3.14) at some point $z = z_0$, usually imposed to $z_0 = 0$, for simplicity. The angular spectrum $\tilde{u}(\mathbf{K})$ is defined as [82]

$$\tilde{u}(\mathbf{K}) = \widetilde{\mathscr{E}}(\mathbf{K}, 0) = \frac{1}{(2\pi)^2} \iint\limits_{\mathbf{R}} \mathrm{d}^2R\, u(\mathbf{R}, 0) e^{-i\mathbf{K}\cdot\mathbf{R}}, \tag{3.19}$$

as $\mathscr{E}(\mathbf{R}, 0) = u(\mathbf{R}, 0)$. The physical interpretation of angular spectrum $\tilde{u}(\mathbf{K})$ is intuitive: It describes the amplitude profile of the beam, at $z = 0$, as a superposition of plane waves with transverse wave vectors, which, for paraxial beams, vanish really quickly as the magnitude of the transverse wave vector grows, as most of the plane waves are centered around the propagation direction $\hat{\mathbf{z}}$.

We now calculate the angular spectrum for Laguerre-Gaussian beams, which will be used in the later sections. By inserting Eq. (3.11) with $z = 0$ into (3.19), and calculating the integral, we have

$$\tilde{u}_{\ell,p}^{LG}(\mathbf{K}) = \frac{i^\ell w_0^2}{2\pi} \mathscr{N}_{\ell,p}^{LG} \left(\frac{k_\perp w_0}{\sqrt{2}}\right)^{|\ell|} e^{-\frac{k_\perp^2 w_0^2}{4}} L_p^{|\ell|}\left(\frac{k_\perp^2 w_0^2}{2}\right) e^{i\ell\phi}. \tag{3.20}$$

The above equation holds in free space. However, when propagating inside the TMD, we need to rescale up the wavevector of our beam by the square root of the dielectric function ϵ of the TMD material, namely $k_0 \mapsto \sqrt{\epsilon} k_0$, which can be taken into account by

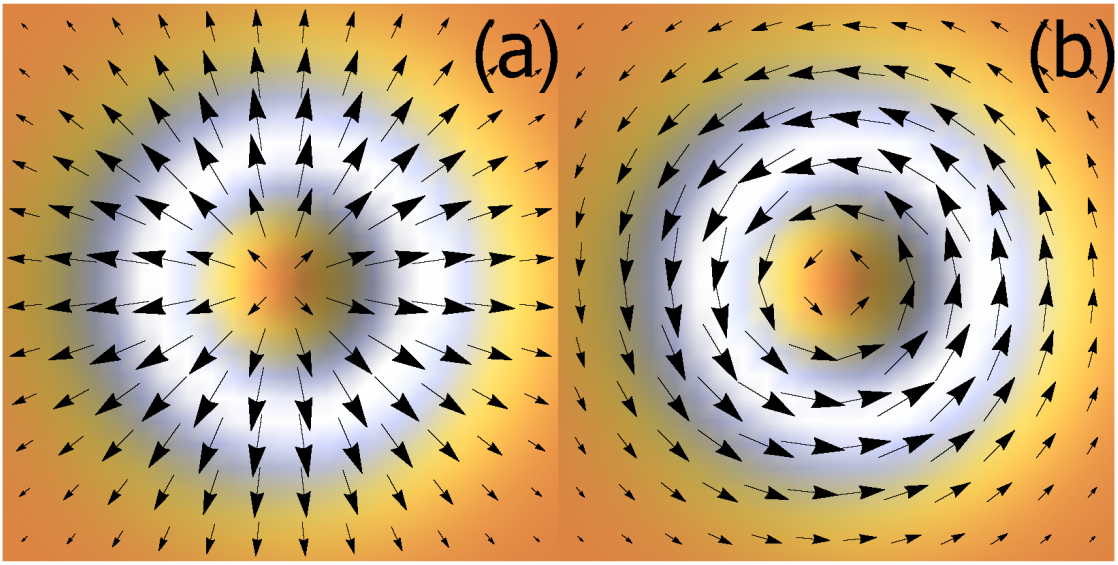

Figure 3.1. *Complex polarisation patterns for co-rotating (a) radially polarised mode* $\mathbf{u}_R^+$ *and (b) azimuthally polarised mode* $\mathbf{u}_A^+$*, defined by Eqs.* (3.22)*, with the characteristic doughnut-shaped intensity distribution underlayed.*

scaling down the norm of the transverse wavevector in (3.20) by a factor of $\sqrt{\epsilon}$, namely $\tilde{u}^{LG}_{\ell,p}(k_\perp, \phi) \mapsto \tilde{u}^{LG}_{\ell,p}(k_\perp/\sqrt{\epsilon}, \phi)$. For a monolayer MoS_2, the dielectric function is approximately $\epsilon \approx 25$, for photon energies equal to the bandgap energy $E_g \simeq 1.8$ eV [83].

3.4 Cylindrically polarised fields

Cylindrically polarised modes, such as radially or azimuthally polarised beams, present a nonuniform polarisation pattern across the transverse profile [35]. This means that the polarisation is dependent on the transverse position, and we cannot separate the amplitude profile and the polarisation of the beam as two independent values like in Eq. (3.5), as the change in the polarisation of the field, like passing through a polariser, will change the overall amplitude profile and vice versa. These unusual polarisations have many useful properties, such as yielding very tight optical focus, and generating strong axial electric [33] or magnetic [34] fields, and it is also possible to classically entangle the fields [84]. These properties are used in many applications, such as optical tweezing [85], single molecule spectroscopy [86], sensing [87], metrology [88], and material processing [89], to name a few.

Ref. [35] shows, that in the paraxial domain, radially and azimuthally polarised beams live in the four dimensional space spanned by the Cartesian product between the first order HG modes $\{u^{HG}_{1,0}, u^{HG}_{0,1}\}$ and the polarisation basis vectors $\{\hat{\mathbf{x}}, \hat{\mathbf{y}}\}$, namely

$$\{u^{HG}_{1,0}, u^{HG}_{0,1}\} \otimes \{\hat{\mathbf{x}}, \hat{\mathbf{y}}\} = \{u^{HG}_{1,0}\hat{\mathbf{x}}, u^{HG}_{1,0}\hat{\mathbf{y}}, u^{HG}_{0,1}\hat{\mathbf{x}}, u^{HG}_{0,1}\hat{\mathbf{y}}\}. \tag{3.21}$$

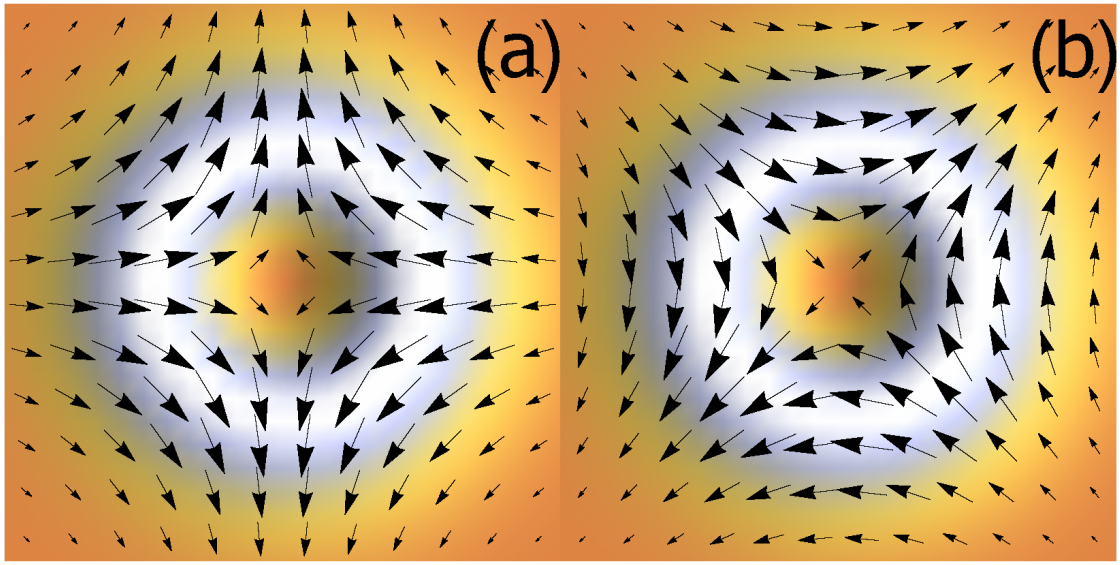

Figure 3.2. *Complex polarisation patterns for counter-rotating (a) radially polarised mode* $\mathbf{u}_R^-$ *and (b) azimuthally polarised mode* $\mathbf{u}_A^-$*, defined by Eqs.* (3.23)*, with the characteristic doughnut-shaped intensity distribution underlayed.*

With suitable superposition of these vectors, we can build four linearly independent, orthogonal vectors, forming a complete four dimensional basis, namely the co-rotating modes:

$$\mathbf{u}_R^+ = \frac{1}{\sqrt{2}}(u_{1,0}^{HG}\hat{\mathbf{x}} + u_{0,1}^{HG}\hat{\mathbf{y}}), \tag{3.22a}$$

$$\mathbf{u}_A^+ = \frac{1}{\sqrt{2}}(-u_{0,1}^{HG}\hat{\mathbf{x}} + u_{1,0}^{HG}\hat{\mathbf{y}}), \tag{3.22b}$$

and the counter-rotating modes:

$$\mathbf{u}_R^- = \frac{1}{\sqrt{2}}(-u_{1,0}^{HG}\hat{\mathbf{x}} + u_{0,1}^{HG}\hat{\mathbf{y}}), \tag{3.23a}$$

$$\mathbf{u}_A^- = \frac{1}{\sqrt{2}}(u_{0,1}^{HG}\hat{\mathbf{x}} + u_{1,0}^{HG}\hat{\mathbf{y}}). \tag{3.23b}$$

The non-uniform polarisation patterns and intensity distribution of these modes are shown in Fig. 3.1 and 3.2.

Explicit calculations in Ref. [35] show, that all of the modes above have zero total angular momentum (TAM). This can also be seen intuitively, by writing the Hermite-Gaussian modes as Laguerre-Gaussian modes given in Eq. (3.13), which results in following ex-

pression for the co-rotating modes:

$$\mathbf{u}_R^+ = \frac{1}{\sqrt{2}}(u_{1,0}^{LG}\hat{\boldsymbol{h}}_- + u_{-1,0}^{LG}\hat{\boldsymbol{h}}_+), \tag{3.24a}$$

$$\mathbf{u}_A^+ = \frac{i}{\sqrt{2}}(u_{1,0}^{LG}\hat{\boldsymbol{h}}_- - u_{-1,0}^{LG}\hat{\boldsymbol{h}}_+). \tag{3.24b}$$

In this case, spatial mode carries one unit of orbital angular momentum (OAM) and polarisation carries one unit of spin angular momentum (SAM), leading to zero global TAM, even though, locally, the beam carries angular momentum. Writing the same for counter-rotating modes has following expressions:

$$\mathbf{u}_R^- = \frac{-1}{\sqrt{2}}(u_{1,0}^{LG}\hat{\boldsymbol{h}}_+ + u_{-1,0}^{LG}\hat{\boldsymbol{h}}_-), \tag{3.25a}$$

$$\mathbf{u}_A^- = \frac{-i}{\sqrt{2}}(u_{1,0}^{LG}\hat{\boldsymbol{h}}_+ - u_{-1,0}^{LG}\hat{\boldsymbol{h}}_-), \tag{3.25b}$$

Now, as radially and azimuthally polarised modes are just sum of LG modes with circular polarisations, the vector potentials can be written then as: [1]

$$\boldsymbol{\mathscr{A}}_R^+ = \frac{A_0}{\sqrt{2}}(u_1^{LG}(\mathbf{r})\hat{\boldsymbol{h}}_- + u_{-1}^{LG}(\mathbf{r})\hat{\boldsymbol{h}}_+)e^{ik_0z-i\omega t}, \tag{3.26a}$$

$$\boldsymbol{\mathscr{A}}_A^+ = \frac{iA_0}{\sqrt{2}}(u_1^{LG}(\mathbf{r})\hat{\boldsymbol{h}}_- - u_{-1}^{LG}(\mathbf{r})\hat{\boldsymbol{h}}_+)e^{ik_0z-i\omega t}, \tag{3.26b}$$

$$\boldsymbol{\mathscr{A}}_R^- = \frac{-A_0}{\sqrt{2}}(u_1^{LG}(\mathbf{r})\hat{\boldsymbol{h}}_+ - u_{-1}^{LG}(\mathbf{r})\hat{\boldsymbol{h}}_-)e^{ik_0z-i\omega t}, \tag{3.26c}$$

$$\boldsymbol{\mathscr{A}}_A^- = \frac{-iA_0}{\sqrt{2}}(u_1^{LG}(\mathbf{r})\hat{\boldsymbol{h}}_+ + u_{-1}^{LG}(\mathbf{r})\hat{\boldsymbol{h}}_-)e^{ik_0z-i\omega t}. \tag{3.26d}$$

[1] From here on, we assume implicitly that $p = 0$, and denote $u_{\ell,0}^{LG}(\mathbf{r}) \equiv u_\ell^{LG}(\mathbf{r})$.

4. EXCITON-LIGHT INTERACTION WITH CYLINDRICALLY POLARISED BEAMS

In this chapter, we introduce the theory of light-matter interaction of TMD excitons. In particular, we show how radially polarised light excites the exciton states in monolayer TMDs. The LMI of excitons with light will be simulated by using Fermi golden rule to calculate the transition rate to the excitons bands, namely the spectral functions. This will give the indication how the particular TMD interacts with light and will also predict the PL spectra of the TMD given that thermal dynamics are also taken into account. We first look at the excitations of bright exciton states, then the excitations of brightened dark exciton states.

4.1 Exciton interaction with cylindrically polarised light

The average transition rate from a groundstate $|GS\rangle$ to an excited exciton state $|\Psi^S_{\mathbf{Q}}\rangle$, under periodic perturbation, is, according to Fermi golden rule, given by [90]

$$w^S_{\mathbf{Q}}(\omega) = \frac{2\pi}{\hbar}\left|\langle\Psi^S_{\mathbf{Q}}|\hat{H}_I|GS\rangle\right|^2 \delta(E^S_{\mathbf{Q}} - \hbar\omega), \tag{4.1}$$

where $E^S_{\mathbf{Q}}$ is the energy dispersion of the state, and $\delta(x)$ is the Dirac delta function. $\hat{H}_I$ is the light-matter interaction Hamiltonian, introduced through minimal coupling [91], which is, in the lowest order (assuming weak excitation of light), given by

$$\hat{H}_I = \frac{|e|}{2m_0}\boldsymbol{\mathscr{A}}^{\pm}_{\mu}(\mathbf{r},t)\cdot\hat{\mathbf{p}}, \tag{4.2}$$

where $\hat{\mathbf{p}}$ is the linear momentum operator, and $\boldsymbol{\mathscr{A}}^{\pm}_{\mu}$ is the vector potential of cylindrically polarised light, given by one of the equations in (3.26). Here, we denote $\mu = \{+,-\} \equiv \{R,A\}$ as the polarisation mode index, and $\pm$ in the superscript separates the co-rotating and counter-rotating modes, respectively.

In Appendix B, we show that the expectation values in Eq. (4.1), by using the definition of

the exciton states (2.1), are given as:

$$\langle \Psi^S_{\mathbf{Q}} | \hat{H}_I | GS \rangle = \frac{1}{\sqrt{\Omega}} \sum_{vc} \sum_{\mathbf{k}} \Lambda^{*S}_{vc,\mathbf{Q}}(\mathbf{k}) \langle \psi_{c,\mathbf{k}+\mathbf{Q}} | \hat{H}_I | \psi_{v,\mathbf{k}} \rangle, \tag{4.3}$$

The elements of the sum in Eq. (4.3) can be expanded further, using the definition of our interaction Hamiltonian and vector potential of co-rotating beams, given by Eqs.(3.26a) and (3.26b):

$$\begin{aligned} \langle \psi_{c,\mathbf{k}+\mathbf{Q}} | \hat{H}_I | \psi_{v,\mathbf{k}} \rangle = & \frac{A_0 |e| e^{-i\omega t}}{\sqrt{2} m_0} \Bigg[\iint\limits_{\mathbf{K}} \mathrm{d}^2 K \, \tilde{u}^{LG}_{+1}(\mathbf{K}) \hat{\boldsymbol{h}}_- \cdot \langle \psi_{c,\mathbf{k}+\mathbf{Q}} | e^{i\mathbf{K}\cdot\mathbf{R}} \hat{\mathbf{p}} | \psi_{v,\mathbf{k}} \rangle \\ & + \mu \iint\limits_{\mathbf{K}'} \mathrm{d}^2 K' \, \tilde{u}^{LG}_{-1}(\mathbf{K}') \hat{\boldsymbol{h}}_+ \cdot \langle \psi_{c,\mathbf{k}+\mathbf{Q}} | e^{i\mathbf{K}'\cdot\mathbf{R}} \hat{\mathbf{p}} | \psi_{v,\mathbf{k}} \rangle \Bigg], \end{aligned} \tag{4.4}$$

where we have expanded the LG beams into their angular spectrum given by Eq. (3.20), and implicitly assumed $z = 0$, i.e., that the beam waist is at the TMD. We get similar expressions for the counter-rotating modes given by Eqs. (3.26c) and (3.26d):

$$\begin{aligned} \langle \psi_{c,\mathbf{k}+\mathbf{Q}} | \hat{H}_I | \psi_{v,\mathbf{k}} \rangle = & \frac{A_0 |e| e^{-i\omega t}}{\sqrt{2} m_0} \Bigg[\iint\limits_{\mathbf{K}} \mathrm{d}^2 K \, \tilde{u}^{LG}_{+1}(\mathbf{K}) \hat{\boldsymbol{h}}_+ \cdot \langle \psi_{c,\mathbf{k}+\mathbf{Q}} | e^{i\mathbf{K}\cdot\mathbf{R}} \hat{\mathbf{p}} | \psi_{v,\mathbf{k}} \rangle \\ & - \mu \iint\limits_{\mathbf{K}'} \mathrm{d}^2 K' \, \tilde{u}^{LG}_{-1}(\mathbf{K}') \hat{\boldsymbol{h}}_- \cdot \langle \psi_{c,\mathbf{k}+\mathbf{Q}} | e^{i\mathbf{K}'\cdot\mathbf{R}} \hat{\mathbf{p}} | \psi_{v,\mathbf{k}} \rangle \Bigg]. \end{aligned} \tag{4.5}$$

In Appendix C, we write these states explicitly in Bloch wavefunction form [92], and use the low thickness of the TMD compared to the wave length of impinging light to write the following approximation [29]:

$$\langle \psi_{c,\mathbf{k}+\mathbf{Q}} | e^{i\mathbf{K}\cdot\mathbf{R}} \hat{\mathbf{p}} | \psi_{v,\mathbf{k}} \rangle \sim \delta(\mathbf{K} - \mathbf{Q}) \langle \psi_{c,\mathbf{k}} | \hat{\mathbf{p}} | \psi_{v,\mathbf{k}} \rangle. \tag{4.6}$$

When these equations above are inserted into Eq. (4.3), we notice that we have get terms proportional to ones in Eq. (2.2), and we then have

$$\langle \Psi^S_{\mathbf{Q}} | \hat{H}_I | GS \rangle = \frac{E_g A_0}{2\sqrt{2} i \hbar \Omega} \left[\tilde{u}^{LG}_{+1}(\mathbf{Q}) (\hat{\boldsymbol{h}}_- \cdot \mathbf{D}^{*S}_{\mathbf{Q}}) + \mu \tilde{u}^{LG}_{-1}(\mathbf{Q}) (\hat{\boldsymbol{h}}_+ \cdot \mathbf{D}^{*S}_{\mathbf{Q}}) \right] e^{-i\omega t}, \tag{4.7}$$

for the the co-rotating modes, and

$$\langle \Psi^S_{\mathbf{Q}} | \hat{H}_I | GS \rangle = \frac{E_g A_0}{2\sqrt{2} i \hbar \Omega} \left[\tilde{u}^{LG}_{+1}(\mathbf{Q}) (\hat{\boldsymbol{h}}_+ \cdot \mathbf{D}^{*S}_{\mathbf{Q}}) - \mu \tilde{u}^{LG}_{-1}(\mathbf{Q}) (\hat{\boldsymbol{h}}_- \cdot \mathbf{D}^{*S}_{\mathbf{Q}}) \right] e^{-i\omega t}, \tag{4.8}$$

for the counter-rotating modes.

4.2 Spectral functions of bright excitons excited by cylindrically polarised light

In this section, we look at how bright excitons interact with cylindrically polarised light. We first consider the case where there is not magnetic field present, and then the case where we have out-of-plane magnetic field causing a Zeeman shift on the energy levels.

With the definition of the dipole moments given in Eq. (2.7), we have that

$$(\hat{\boldsymbol{h}}_+ \cdot \mathbf{D}^{*\xi^\pm}_{b,\mathbf{Q}}) = \sqrt{\Omega} d_\parallel \tag{4.9a}$$

$$(\hat{\boldsymbol{h}}_- \cdot \mathbf{D}^{*\xi^\pm}_{b,\mathbf{Q}}) = \mp e^{-2i\varphi}\sqrt{\Omega} d_\parallel \tag{4.9b}$$

using the equations above, our expectation values are given as:

$$\langle \Psi^\xi_{\mathbf{Q}} | \hat{H}_I | GS \rangle = \frac{E_g A_0 d_\parallel}{2i\sqrt{2}\hbar\sqrt{\Omega}} \left[\mp \tilde{u}^{LG}_1(\mathbf{Q}) e^{-2i\varphi_Q} + \mu \tilde{u}^{LG}_{-1}(\mathbf{Q}) \right] e^{-i\omega t}, \tag{4.10a}$$

$$\langle \Psi^\xi_{\mathbf{Q}} | \hat{H}_I | GS \rangle = \frac{E_g A_0 d_\parallel}{2i\sqrt{2}\hbar\sqrt{\Omega}} \left[\tilde{u}^{LG}_1(\mathbf{Q}) \pm \mu \tilde{u}^{LG}_{-1}(\mathbf{Q}) e^{-2i\varphi} \right] e^{-i\omega t}, \tag{4.10b}$$

for the co-rotating and counter-rotating modes, respectively.

Inserting these two equations into Eq.(4.1), and integrating over all frequencies ω, we get the total rate of excitation of an exciton state $|\Psi^{\xi^\pm}_{b,\mathbf{Q}}\rangle$:

$$W^{\xi^\pm}_{b,\mathbf{Q}}(\boldsymbol{\mathscr{A}}^+_\mu) = \int_0^\infty \mathrm{d}\omega \, w^S_{\mathbf{Q}}(\omega) = \frac{\pi E_g^2 A_0^2 d_\parallel^2}{4\hbar^3\Omega} \left| \mp \tilde{u}^{LG}_1(\mathbf{Q}) e^{-2i\varphi_Q} + \mu \tilde{u}^{LG}_{-1}(\mathbf{Q}) \right|^2, \tag{4.11a}$$

$$W^{\xi^\pm}_{b,\mathbf{Q}}(\boldsymbol{\mathscr{A}}^-_\mu) = \int_0^\infty \mathrm{d}\omega \, w^S_{\mathbf{Q}}(\omega) = \frac{\pi E_g^2 A_0^2 d_\parallel^2}{4\hbar^3\Omega} \left| \tilde{u}^{LG}_1(\mathbf{Q}) \pm \mu \tilde{u}^{LG}_{-1}(\mathbf{Q}) e^{-2i\varphi_Q} \right|^2. \tag{4.11b}$$

Using Eq. (3.20), we can explicitly calculate the modulus terms in Eqs. (4.11a) and (4.11b):

$$\left| \mp \tilde{u}^{LG}_1(\mathbf{Q}) e^{-2i\varphi_Q} + \mu \tilde{u}^{LG}_{-1}(\mathbf{Q}) \right|^2 = 2 |\tilde{u}^{LG}_1(Q/\sqrt{\epsilon})|^2 \left(1 \pm \mu\right), \tag{4.12a}$$

$$\left| \tilde{u}^{LG}_1(\mathbf{Q}) \pm \mu \tilde{u}^{LG}_{-1}(\mathbf{Q}) e^{-2i\varphi_Q} \right|^2 = 2 |\tilde{u}^{LG}_1(Q/\sqrt{\epsilon})|^2 \left(1 \mp \mu \cos 4\varphi\right), \tag{4.12b}$$

where we have used the fact that modulus of the angular spectrum of LG beam is only dependent on the norm of the momentum, and that $|\tilde{u}^{LG}_{-1}(Q)|^2 = |\tilde{u}^{LG}_1(Q)|^2$. Also, because the interaction takes place inside the TMD, we have rescaled the momentum down in the angular spectrum by the factor of $\sqrt{\epsilon}$. This leads to following transition rates for the

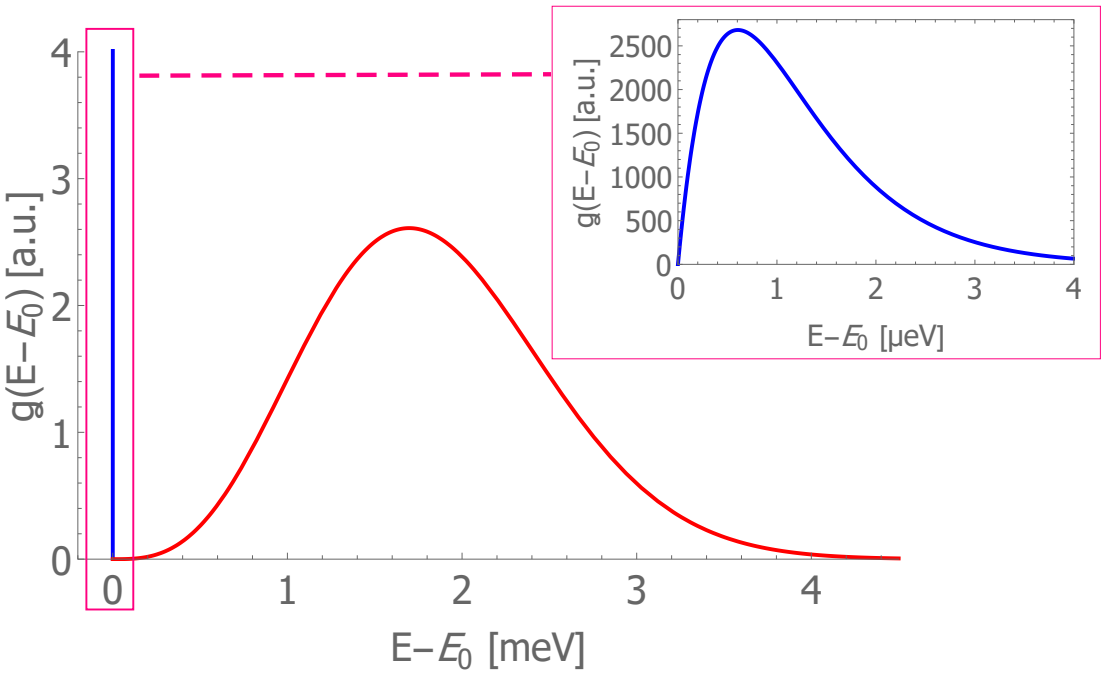

Figure 4.1. *Spectral density functions of excitons excited by co-rotating azimuthally polarised light (blue line) and co-rotating radially polarised light (red line). We see the spectral function of the light-like-band* $g^{\xi^+}_{\mathscr{A}^+_R}(E)$ *in meV scale, and we have zoomed in on the spectral function of the particle-like band* $g^{\xi^-}_{\mathscr{A}^+_A}(E)$*, which is in the* μ*eV scale.*

cylindrically polarised beams, for plane wave components with momentum $\mathbf{Q}$:

$$W^{\xi^+}_{b,\mathbf{Q}}(\mathscr{A}^+_A) = W^{\xi^-}_{b,\mathbf{Q}}(\mathscr{A}^+_R) = 0, \tag{4.13a}$$

$$W^{\xi^-}_{b,\mathbf{Q}}(\mathscr{A}^+_A) = W^{\xi^+}_{b,\mathbf{Q}}(\mathscr{A}^+_R) = \frac{\pi E_g^2 A_0^2 d_\parallel^2}{\hbar^3 \Omega} \left| \tilde{u}_1^{LG}(Q/\sqrt{\epsilon}) \right|^2, \tag{4.13b}$$

$$W^{\xi^+}_{b,\mathbf{Q}}(\mathscr{A}^-_A) = W^{\xi^-}_{b,\mathbf{Q}}(\mathscr{A}^-_R) = \frac{\pi E_g^2 A_0^2 d_\parallel^2}{2\hbar^3 \Omega} \left| \tilde{u}_1^{LG}(Q/\sqrt{\epsilon}) \right|^2 (1 + \cos 4\varphi)\,, \tag{4.13c}$$

$$W^{\xi^-}_{b,\mathbf{Q}}(\mathscr{A}^-_A) = W^{\xi^+}_{b,\mathbf{Q}}(\mathscr{A}^-_R) = \frac{\pi E_g^2 A_0^2 d_\parallel^2}{2\hbar^3 \Omega} \left| \tilde{u}_1^{LG}(Q/\sqrt{\epsilon}) \right|^2 (1 - \cos 4\varphi)\,. \tag{4.13d}$$

The spectral density function $\mathscr{g}(E)$ of an exciton band is estimated by integrating the transition rates over the whole exciton center-of-mass momentum $\mathbf{Q}$ space, thus obtaining the total transition rate for the exciton band, and then making a change of variables to integrating over the energies [29]:

$$W = \iint_{\mathbf{Q}} \mathrm{d}^2 Q\, W_{\mathbf{Q}} = \int \mathrm{d}E\, \mathscr{g}(E), \tag{4.14}$$

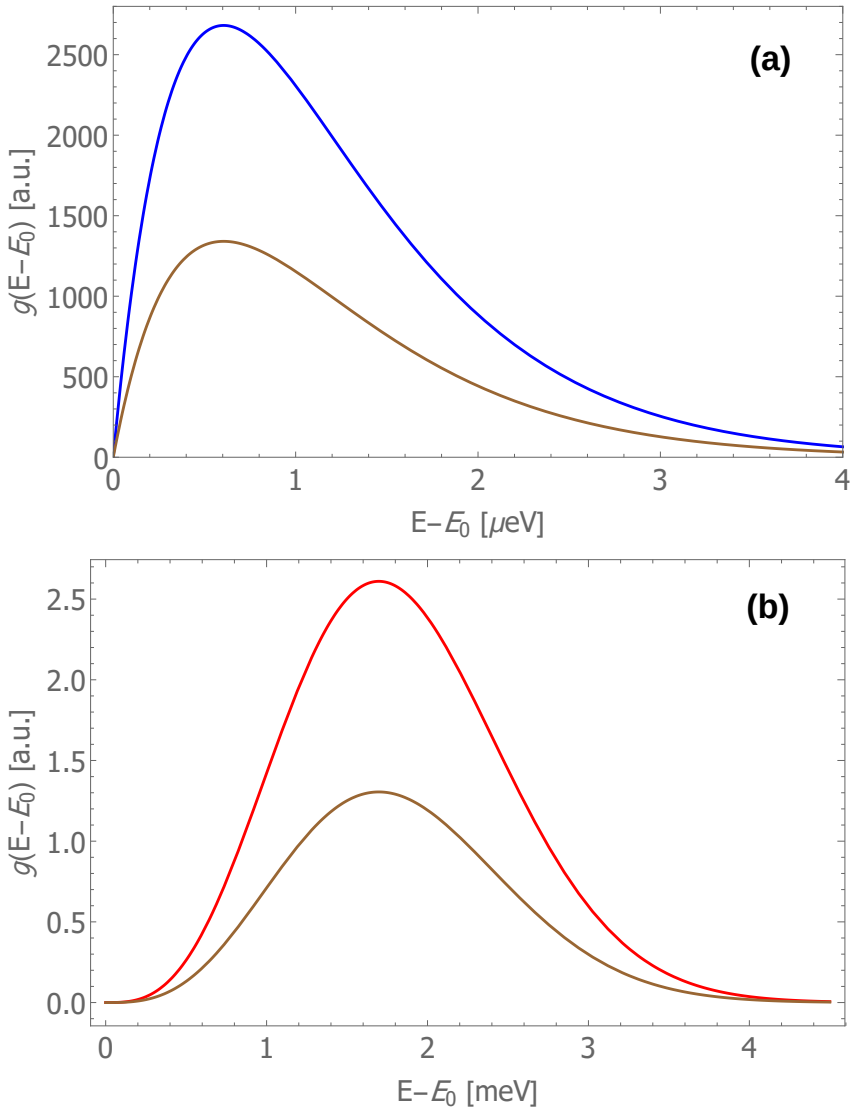

Figure 4.2. *Spectral density functions for counter-rotating cylindrically polarised beams (brown lines), where the transition energy is equally distributed for particle-like bands (panel (a)) and light-like bands (panel (b)). For comparison, we have plotted the spectral functions for co-rotating modes, as blue lines in panel (a), for azimuthally polarised light, and red lines in panel (b), for radially polarised light.*

For co-rotating azimuthally polarised beam, we have $W_b^{\xi^+}(\mathscr{A}_A^+) = 0$, and

$$W_b^{\xi^-}(\mathscr{A}_A^+) = \iint_{\mathbf{Q}} \mathrm{d}^2Q\, W_{b,\mathbf{Q}}^{\xi^-} = \frac{E_g^2 A_0^2 d_\parallel^2}{4\pi\hbar^3} \int_0^{2\pi} \mathrm{d}\varphi_Q \int_0^\infty \mathrm{d}Q\, Q |\tilde{u}_1^{LG}(Q/\sqrt{\epsilon})|^2$$
$$= \frac{E_g^2 A_0^2 d_\parallel^2}{2\hbar^3} \int_0^\infty \mathrm{d}Q\, Q |\tilde{u}_1^{LG}(Q/\sqrt{\epsilon})|^2, \tag{4.15}$$

and for ξ^- bands, Eq. (2.4a) gives us $Q = \sqrt{2M_b(E)}/\hbar$, where, for simplicity, we have imposed $E_0 = 0$, and when carrying out the change of variables, our integral becomes

$$W_b^{\xi^-}(\mathscr{A}_A^+) = \int \mathrm{d}E\, \eta \left(\frac{M_b}{\hbar^2}\right) \left(\frac{w_0^2}{2\epsilon}\right) \left(\frac{2M_b E}{\hbar^2}\right) e^{-\left(\frac{w_0^2}{2\epsilon}\right)\left(\frac{2M_b E}{\hbar^2}\right)}, \tag{4.16}$$

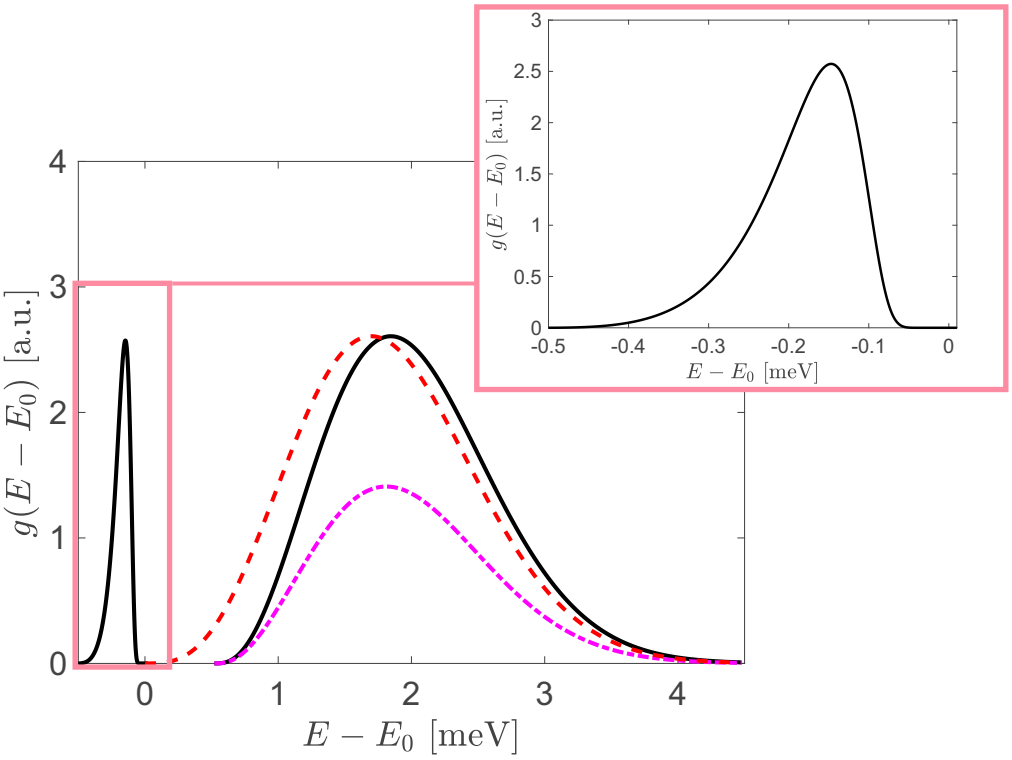

Figure 4.3. *Spectral density functions (black line) with out-of-plane magnetic field $|\mathbf{B}_\perp| = 10$ T, for co-rotating radially polarised beam. For comparison, we have plotted spectral functions for the case $|\mathbf{B}_\perp| = 0$ as dashed red curve for co-rotating radially polarised mode, and the spectral function of light-like band for counter-rotating modes as dashed magenta. We see that the presence of out-of-plane magnetic field brings nonzero spectral function for the particle-like band, as well as modifying the shape of the spectral functions.*

where $\eta = (E_g^2 A_0^2 d_\parallel^2 \pi w_0^2)/\hbar^3$. This means that

$$\mathscr{g}^{\xi^-}_{\boldsymbol{\mathcal{A}}_A^+}(E) = \eta \left(\frac{M_b}{\hbar^2}\right)\left(\frac{w_0^2}{2\epsilon}\right)\left(\frac{2M_b E}{\hbar^2}\right) e^{-\left(\frac{w_0^2}{2\epsilon}\right)\left(\frac{2M_b E}{\hbar^2}\right)}, \tag{4.17}$$

and, trivially, spectral density for the linear band is $\mathscr{g}^{\xi^+}_{\boldsymbol{\mathcal{A}}_A^+}(E) = 0$.

For co-rotating radially polarised beam, we have it other way around, namely $W^{\xi^-} = 0$, and

$$W^{\xi^+}_{b,\mathbf{Q}}(\boldsymbol{\mathcal{A}}_R^+) = \int \mathrm{d}E\, \eta \left(\frac{E}{(2\gamma)^2}\right)\left(\frac{w_0^2}{2\epsilon}\right)\left(\frac{E^2}{(2\gamma)^2}\right) e^{-\left(\frac{w_0^2}{2\epsilon}\right)\left(\frac{E^2}{(2\gamma)^2}\right)}, \tag{4.18}$$

where change of variables have been made with $Q = 2\gamma E$, from Eq.(2.4b), leading to spectral density function

$$\mathscr{g}^{\xi^+}_{\boldsymbol{\mathcal{A}}_R^+}(E) = \eta \left(\frac{E}{(2\gamma)^2}\right)\left(\frac{w_0^2}{2\epsilon}\right)\left(\frac{E^2}{(2\gamma)^2}\right) e^{-\left(\frac{w_0^2}{2\epsilon}\right)\left(\frac{E^2}{(2\gamma)^2}\right)}, \tag{4.19}$$

while trivially, $\mathscr{g}^{\xi^-}_{\boldsymbol{\mathcal{A}}_R^+}(E) = 0$. From here on, all the simulations of the spectral functions will

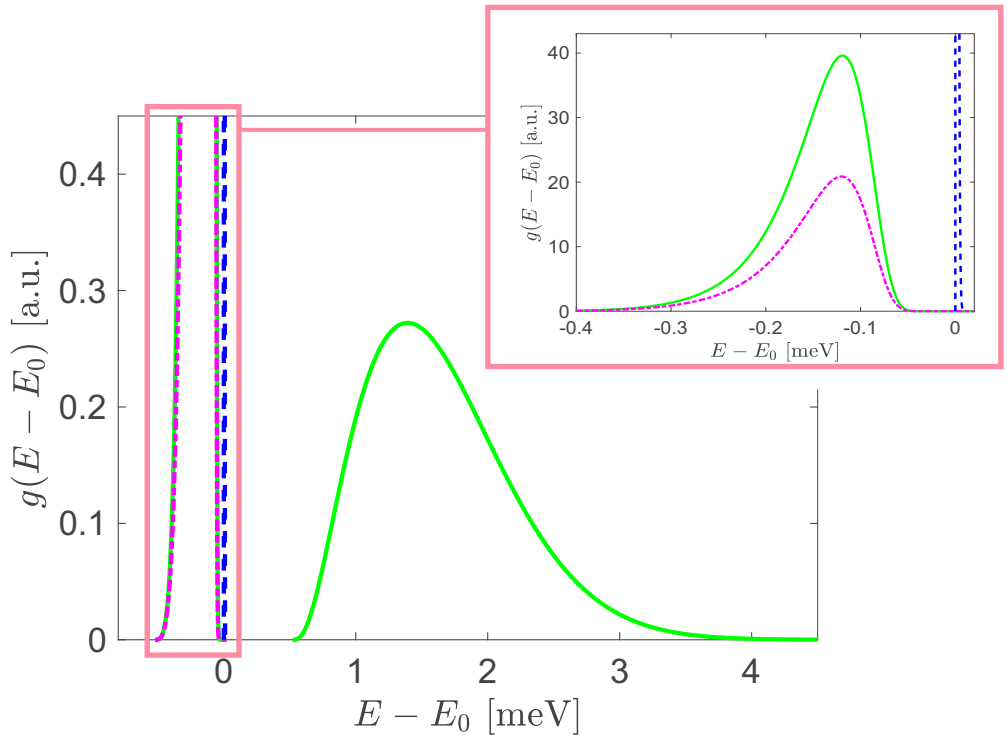

Figure 4.4. *Spectral density functions (green line) with out-of-plane magnetic field $|\mathbf{B}_\perp| = 10$ T, for co-rotating azimuthally polarised beam. For comparison, we have plotted spectral functions for the case $|\mathbf{B}_\perp| = 0$ as dashed blue curve for co-rotating azimuthally polarised beam, and the spectral function of particle-like band for counter-rotating modes as dashed magenta. The effect of out-of-plane magnetic field is to introduce nonzero spectral function for the light-like band as well as significantly broadening the spectral function of particle-like band.*

be done for MoS_2, and we use the following parameters for all the figures: Beam waist $w_0 = 1.5\ \mu$, parameter $\gamma = 1.47$ eV $\cdot$ Å, bright exciton effective mass $M_b = 1.4m_0$ [63], and dielectric function $\epsilon = 25$. The spectral functions of bright excitons for co-rotating cylindrically polarised modes are shown in Fig. 4.1. The results show, that co-rotating modes show selective photoexcitation of the bright exciton bands: co-rotating azimuthally polarised light only excites transition into the lower, parabolic particle-like band of the two bright exciton bands, where as for co-rotating radially polarised light, it is the opposite, namely it only excites transitions into the linear light-like band. This gives the possibility to tune exciton population in the bands by switching between the co-rotating cylindrically polarised modes.

For counter-rotating cylindrically polarised beams, on the other hand, we have

$$\begin{aligned} W^{\xi\pm}_{b,\mathbf{Q}}(\boldsymbol{\mathcal{A}}^-_\mu) &= \frac{1}{2}\frac{E_g^2 A_0^2 d_\parallel^2}{4\pi\hbar^3}\int_0^{2\pi} \mathrm{d}\varphi_Q\,(1 \pm \mu\cos 4\varphi_Q)\int_0^\infty \mathrm{d}Q\,Q|\tilde{u}^{LG}_{\pm 1}(Q/\sqrt{\epsilon})|^2 \\ &= \frac{1}{2}\frac{E_g^2 A_0^2 d_\parallel^2}{2\hbar^3}\int_0^\infty \mathrm{d}Q\,Q|\tilde{u}^{LG}_{\pm 1}(Q/\sqrt{\epsilon})|^2, \end{aligned} \tag{4.20}$$

as $\int_0^{2\pi} \mathrm{d}\varphi_Q \, \cos 4\varphi_Q = 0$. Thus, we arrive in a result that

$$\mathscr{g}^{\xi^-}_{\boldsymbol{\mathscr{A}}^-_\mu}(E) = \frac{1}{2}\mathscr{g}^{\xi^+}_{\boldsymbol{\mathscr{A}}^+_A}(E), \tag{4.21a}$$

$$\mathscr{g}^{\xi^+}_{\boldsymbol{\mathscr{A}}^-_\mu}(E) = \frac{1}{2}\mathscr{g}^{\xi^-}_{\boldsymbol{\mathscr{A}}^+_R}(E), \tag{4.21b}$$

i.e., both counter-rotating modes excite transitions equally for both bands, leading to the same result as for uniformly polarised LG beam with $\ell = 1$, reported in Ref [29]. The spectral functions of bright excitons for counter-rotating modes are shown in Fig. 4.2.

When out-of-plane magnetic field is present, we do the same as above, but now insert Eq. (2.12) into Eqs. (4.7), and insert those into (4.1), and get the following:

$$\widetilde{W}^{\xi^-}_{b,\mathbf{Q}}(\boldsymbol{\mathscr{A}}^+_\mu) = \frac{\pi E_g^2 A_0^2 d_\parallel^2}{4\hbar^3\Omega\left(\mathscr{N}^{\xi^-}_{b,\mathbf{Q}}\right)^2}\left|\tilde{u}^{LG}_1(\mathbf{Q})e^{-2i\varphi_Q} + \mu\,\kappa_1\tilde{u}^{LG}_{-1}(\mathbf{Q})\right|^2, \tag{4.22a}$$

$$\widetilde{W}^{\xi^+}_{b,\mathbf{Q}}(\boldsymbol{\mathscr{A}}^+_\mu) = \frac{\pi E_g^2 A_0^2 d_\parallel^2}{4\hbar^3\Omega\left(\mathscr{N}^{\xi^+}_{b,\mathbf{Q}}\right)^2}\left|-\tilde{u}^{LG}_1(\mathbf{Q})e^{-2i\varphi_Q} + \mu\,\kappa_2\tilde{u}^{LG}_{-1}(\mathbf{Q})\right|^2, \tag{4.22b}$$

$$\widetilde{W}^{\xi^-}_{b,\mathbf{Q}}(\boldsymbol{\mathscr{A}}^-_\mu) = \frac{\pi E_g^2 A_0^2 d_\parallel^2}{4\hbar^3\Omega\left(\mathscr{N}^{\xi^-}_{b,\mathbf{Q}}\right)^2}\left|\kappa_1\tilde{u}^{LG}_1(\mathbf{Q}) + \mu\,\tilde{u}^{LG}_{-1}(\mathbf{Q})e^{-2i\varphi_Q}\right|^2, \tag{4.22c}$$

$$\widetilde{W}^{\xi^+}_{b,\mathbf{Q}}(\boldsymbol{\mathscr{A}}^-_\mu) = \frac{\pi E_g^2 A_0^2 d_\parallel^2}{4\hbar^3\Omega\left(\mathscr{N}^{\xi^+}_{b,\mathbf{Q}}\right)^2}\left|\tilde{u}^{LG}_1(\mathbf{Q}) - \mu\,\kappa_2\tilde{u}^{LG}_{-1}(\mathbf{Q})e^{-2i\varphi_Q}\right|^2. \tag{4.22d}$$

Now, like we did above, we integrate over the momentum space $\mathbf{Q}$ to relate the transition rate with the spectral function:

$$\widetilde{W}^{\xi^-}_b(\boldsymbol{\mathscr{A}}^+_\mu) = \frac{E_g^2 A_0^2 d_\parallel^2}{2\hbar^3}\int_0^\infty \mathrm{d}Q\, Q\, \zeta_{-\mu}(Q)|\tilde{u}^{LG}_1(Q/\sqrt{\epsilon})|^2, \tag{4.23a}$$

$$\widetilde{W}^{\xi^+}_b(\boldsymbol{\mathscr{A}}^+_\mu) = \frac{E_g^2 A_0^2 d_\parallel^2}{2\hbar^3}\int_0^\infty \mathrm{d}Q\, Q\, \zeta_{\mu}(Q)|\tilde{u}^{LG}_1(Q/\sqrt{\epsilon})|^2, \tag{4.23b}$$

$$\widetilde{W}^{\xi^\pm}_b(\boldsymbol{\mathscr{A}}^-_\mu) = \frac{E_g^2 A_0^2 d_\parallel^2}{2\hbar^3}\int_0^\infty \mathrm{d}Q\, Q|\tilde{u}^{LG}_1(Q/\sqrt{\epsilon})|^2, \tag{4.23c}$$

where we have defined

$$\zeta_\mu(Q) \coloneqq 1 + \mu\,\frac{\gamma Q}{\sqrt{(g_b\mathscr{B}_\perp)^2 + \gamma^2 Q^2}}. \tag{4.24}$$

We notice that for counter-rotating modes, out-of-plane magnetic field does not modify the transition rates of the bright excitons band in the momentum space, thus affecting the spectral function only by the change in energy dispersion. For the co-rotating modes, we see that contrary to the case when $|\mathbf{B}_\perp| = 0$, we have nonzero transition rate for

both bands, for both cylindrically polarised modes, indicated by the ζ_μ function, which has values on the interval $[1,2]$ for $\mu=1$, and $[0,1]$ for $\mu=-1$. We see that when $Q\to\infty$, then $\zeta_\mu \to 1+\mu$, which means that for low Q, out-of-plane magnetic field makes the transition possible for both bands, but for increasing Q, less excitations are possible for the other band, depending on which cylindrical polarisation mode is employed.

We will not solve the exact spectral functions, as solving Q in Eqs. (2.9) would be really cumbersome. Instead, to plot the spectral functions in energy, we solve them pointwise and numerically. These spectral functions are shown in Fig. 4.3 for radially polarised, and in Fig. 4.4 for azimuthally polarised modes, where for the bright exciton g-factor we used the one for MoS_2, $g_b=-1.8$. We have also used $|\mathbf{B}_\perp|=10$ T for these plots. We see that because the magnetic field made the parabolic band have a linear region for small values of exciton center-of-mass momentum, we have significant broadening of the parabolic band spectral function, for all cylindrically polarised beams. Also, we see that now both co-rotating beams excite both exciton bands. The ratio between the total transitions to the particle-like band and the light-like band for radially polarised beam is about $\widetilde{W}_b^{\xi^-}(\boldsymbol{\mathcal{A}}_R^+)/\widetilde{W}_b^{\xi^+}(\boldsymbol{\mathcal{A}}_R^+)\sim 10\%$, and vice versa for the azimuthally polarised beam. This gives the possibility to fine-tune the exciton population in these bands by using tunable out-of-plane magnetic field on the TMD.

4.3 Spectral functions of dark excitons excited by cylindrically polarised light

First considering the case where out-of-plane magnetic field is neglected: By inserting Eqs. (2.22) into (4.7) and (4.8), and those into (4.1), and integrating over all frequencies ω, we get following equations for transition rates:

$$\widetilde{W}_{d,\mathbf{Q}}^{\xi^+}(\boldsymbol{\mathcal{A}}_\mu^+)=\frac{\pi E_g^2A_0^2d_\parallel^2}{2\hbar^3\Omega}\left|-\alpha(\mathbf{Q})^*\tilde{u}_1^{LG}(\mathbf{Q})-\mu\,\alpha(\mathbf{Q})\tilde{u}_{-1}^{LG}(\mathbf{Q})\right|^2, \tag{4.25a}$$

$$\widetilde{W}_{d,\mathbf{Q}}^{\xi^-}(\boldsymbol{\mathcal{A}}_\mu^+)=\frac{\pi E_g^2A_0^2d_\parallel^2}{2\hbar^3\Omega}\left|-\beta(\mathbf{Q})^*\tilde{u}_1^{LG}(\mathbf{Q})+\mu\,\beta(\mathbf{Q})\tilde{u}_{-1}^{LG}(\mathbf{Q})\right|^2, \tag{4.25b}$$

$$\widetilde{W}_{d,\mathbf{Q}}^{\xi^+}(\boldsymbol{\mathcal{A}}_\mu^-)=\frac{\pi E_g^2A_0^2d_\parallel^2}{2\hbar^3\Omega}\left|-\alpha(\mathbf{Q})\tilde{u}_1^{LG}(\mathbf{Q})-\mu\,\alpha(\mathbf{Q})^*\tilde{u}_{-1}^{LG}(\mathbf{Q})\right|^2. \tag{4.25c}$$

$$\widetilde{W}_{d,\mathbf{Q}}^{\xi^-}(\boldsymbol{\mathcal{A}}_\mu^-)=\frac{\pi E_g^2A_0^2d_\parallel^2}{2\hbar^3\Omega}\left|\beta(\mathbf{Q})\tilde{u}_1^{LG}(\mathbf{Q})+\mu\,\beta(\mathbf{Q})^*\tilde{u}_{-1}^{LG}(\mathbf{Q})\right|^2. \tag{4.25d}$$

Using Eqs. (2.21a), (2.21b) and (3.20), and integrating over the $\mathbf{Q}$-space, like in the

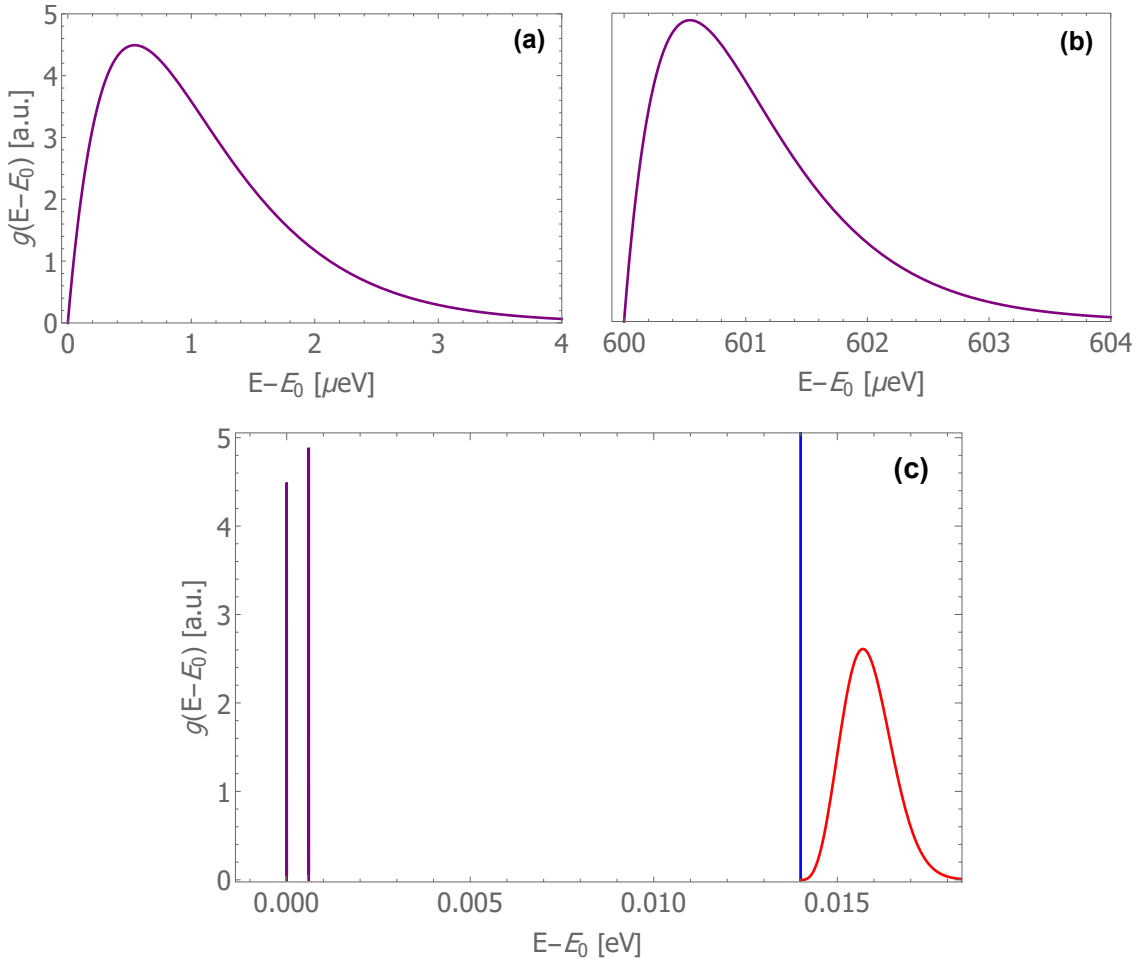

Figure 4.5. *Spectral density functions of brightened dark excitons, with parallel magnetic field $|\mathbf{B}_{\parallel}| = 10$ T, and no perpendicular magnetic field present, in panels (a) and (b). Purple line is for both co-rotating modes. In panel (c) we have plotted for comparison the bright exciton excitations, to show the effect of dark-bright exciton splitting, $\Delta = 14$ meV.*

previous section, we obtain the following expressions for the total transition rates:

$$\widetilde{W}_d^{\xi^-}(\boldsymbol{\mathscr{A}}_\mu^+) = \frac{E_g^2 A_0^2 d_\parallel^2}{2\hbar^3} \int_0^\infty \mathrm{d}Q\, Q\, a_1(Q) |\tilde{u}_1^{LG}(Q/\sqrt{\epsilon})|^2, \tag{4.26a}$$

$$\widetilde{W}_d^{\xi^+}(\boldsymbol{\mathscr{A}}_\mu^+) = \frac{E_g^2 A_0^2 d_\parallel^2}{2\hbar^3} \int_0^\infty \mathrm{d}Q\, Q\, b_1(Q) |\tilde{u}_1^{LG}(Q/\sqrt{\epsilon})|^2, \tag{4.26b}$$

$$\widetilde{W}_d^{\xi^-}(\boldsymbol{\mathscr{A}}_\mu^-) = \frac{E_g^2 A_0^2 d_\parallel^2}{2\hbar^3} \int_0^\infty \mathrm{d}Q\, Q \big(a_1(Q) + \mu a_2(Q)\big) |\tilde{u}_1^{LG}(Q/\sqrt{\epsilon})|^2, \tag{4.26c}$$

$$\widetilde{W}_d^{\xi^+}(\boldsymbol{\mathscr{A}}_\mu^-) = \frac{E_g^2 A_0^2 d_\parallel^2}{2\hbar^3} \int_0^\infty \mathrm{d}Q\, Q \big(b_1(Q) + \mu\, b_2(Q)\big) |\tilde{u}_1^{LG}(Q/\sqrt{\epsilon})|^2, \tag{4.26d}$$

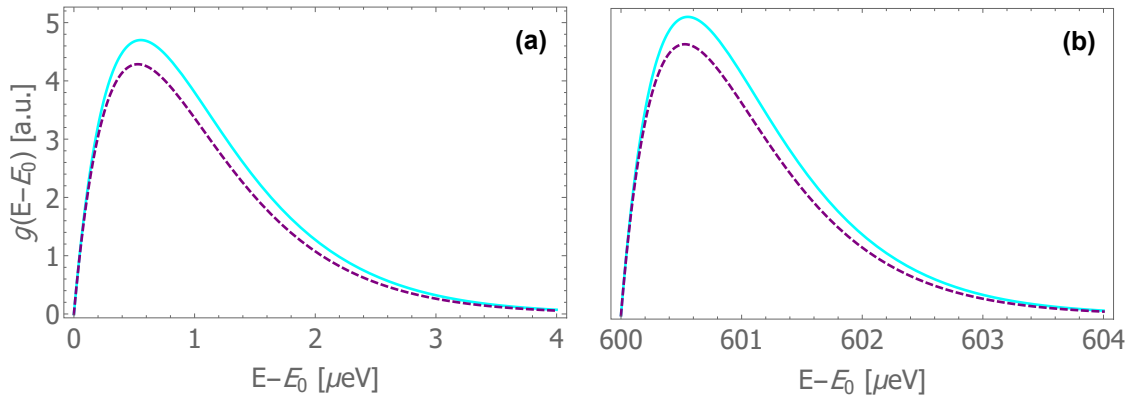

Figure 4.6. *Spectral density functions of brightened dark excitons, with parallel magnetic field $|\mathbf{B}_{\parallel}| = 10$ T, and no perpendicular magnetic field present. The cyan line is for counter-rotating radially polarised beam, and purple dashed line for counter-rotating azimuthally polarised beam.*

where

$$a_1(Q) = (g_{\parallel}\mathscr{B}_{\parallel})^2 \frac{(\Delta + \nu Q^2 + \gamma Q)^2 + (\gamma Q)^2}{(\Delta + \nu Q^2)^2 (\Delta + \nu Q^2 + 2\gamma Q)^2}, \tag{4.27a}$$

$$b_1(Q) = (g_{\parallel}\mathscr{B}_{\parallel})^2 \frac{(\Delta_1 + \nu Q^2 + \gamma Q)^2 + (\gamma Q)^2}{(\Delta_1 + \nu Q^2)^2 (\Delta_1 + \nu Q^2 + 2\gamma Q)^2}, \tag{4.27b}$$

$$a_2(Q) = (g_{\parallel}\mathscr{B}_{\parallel})^2 \frac{\gamma Q (\Delta + \nu Q^2 + \gamma Q)}{(\Delta + \nu Q^2)^2 (\Delta + \nu Q^2 + 2\gamma Q)^2}, \tag{4.27c}$$

$$b_2(Q) = (g_{\parallel}\mathscr{B}_{\parallel})^2 \frac{\gamma Q (\Delta_1 + \nu Q^2 + \gamma Q)}{(\Delta_1 + \nu Q^2)^2 (\Delta_1 + \nu Q^2 + 2\gamma Q)^2}. \tag{4.27d}$$

Using Eq. (2.14), we can do the change of variables and transform the integral to function of energy, giving us the spectral functions:

$$\widetilde{\mathscr{G}}^{\xi^-}_{d,\mathscr{A}^+_\mu}(E) = \eta\, a_1\big(f_1(E)\big) \left(\frac{M_d}{\hbar^2}\right) \left(\frac{w_0^2 f_1(E)^2}{2\epsilon}\right) e^{-\frac{w_0^2 f_1(E)^2}{2\epsilon}}, \tag{4.28a}$$

$$\widetilde{\mathscr{G}}^{\xi^+}_{d,\mathscr{A}^+_\mu}(E) = \eta\, b_1\big(f_2(E)\big) \left(\frac{M_d}{\hbar^2}\right) \left(\frac{w_0^2 f_2(E)^2}{2\epsilon}\right) e^{-\frac{w_0^2 f_2(E)^2}{2\epsilon}}, \tag{4.28b}$$

$$\widetilde{\mathscr{G}}^{\xi^-}_{d,\mathscr{A}^-_\mu}(E) = \eta \Big[a_1\big(f_1(E)\big) + \mu\, a_2\big(f_1(E)\big)\Big] \left(\frac{M_d}{\hbar^2}\right) \left(\frac{w_0^2 f_1(E)^2}{2\epsilon}\right) e^{-\frac{w_0^2 f_1(E)^2}{2\epsilon}}, \tag{4.28c}$$

$$\widetilde{\mathscr{G}}^{\xi^+}_{d,\mathscr{A}^-_\mu}(E) = \eta \Big[b_1\big(f_2(E)\big) + \mu\, b_2\big(f_2(E)\big)\Big] \left(\frac{M_d}{\hbar^2}\right) \left(\frac{w_0^2 f_2(E)^2}{2\epsilon}\right) e^{-\frac{w_0^2 f_2(E)^2}{2\epsilon}}, \tag{4.28d}$$

where

$$f_1(E) = \frac{\sqrt{2M_d E}}{\hbar}, \tag{4.29a}$$

$$f_2(E) = \frac{\sqrt{2M_d(E-\delta)}}{\hbar}. \tag{4.29b}$$

Spectral functions for brightened dark excitons are in Fig. 4.5 for co-rotating cylindrically

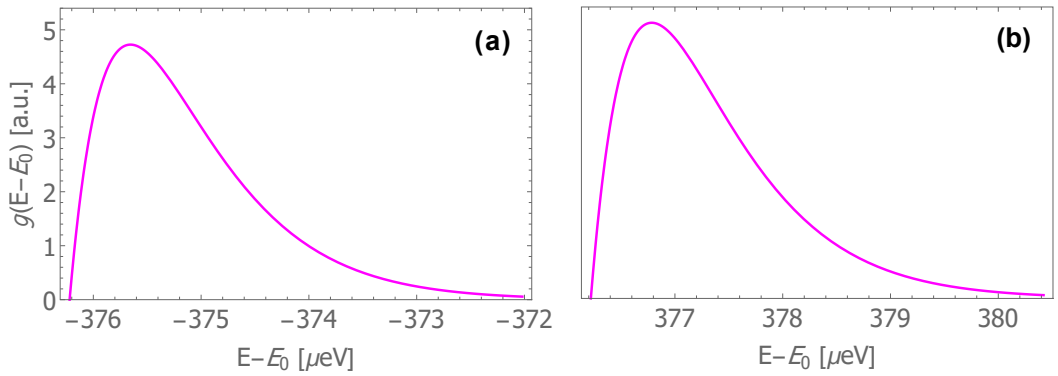

Figure 4.7. *Spectral density functions of brightened dark excitons, with parallel magnetic field $|\mathbf{B}_{\parallel}| = 10$ T, and perpendicular magnetic field $|\mathbf{B}_{\perp}| = 3$ T. Panel (a) is for the K valley, and panel (b) for the K' valley. The Zeeman interaction lowers the energy of the state in the K valley by about 400 meV, hence the negative energies in the x-axis in panel (a), and, in contrast, increases the energy of the K' valley state by the same amount, leading to positive energies in the x-axis in panel (b). The spectral functions are the same for all cylindrically polarised modes.*

polarised modes, and in Fig. 4.6 for counter-rotating modes. We have used $|\mathbf{B}_{\parallel}| = 10$ T for these figures. We have used the dark exciton effective mass of MoS_2 $M_d = 1.5m_0$ [63], and also its latest measured bright/dark exciton splitting value $\Delta = 14$ meV [26], and dark/gray exciton splitting $\delta = 0.6$ meV, which is actually for WSe_2, but there is not a clear value for MoS_2 [26], so we use this one. The ratio between the total transitions of brightened dark states to the ones of bright states are about $\widetilde{W}_b^{\xi^-}(\boldsymbol{\mathscr{A}}_\mu^\pm)/\widetilde{W}_b^{\xi^-}(\boldsymbol{\mathscr{A}}_\mu^\pm) \sim 0.2\%$, which is corroborated by the previous studies. Even though the amount of excitations is really low, these dark excitons can be seen in the PL spectra, when thermal population is taken into account in equilibrium, and the dark excitons can sometimes even dominate the PL spectra at low temperatures [21, 22, 27].

The spectral functions are the same for co-rotating modes. For the counter-rotating modes, as these spectral functions have an extra term, we see higher spectral function for the counter-rotating radially polarised beam and lower it for azimuthally polarised beams, compared to the co-rotating modes. This added or subtracted amount is about 5% of the peak of co-rotating modes.

When the out-of-plane magnetic field is present, we have neglected the exchange interaction for brightened states. We now insert Eq. (2.27) into (4.7) and (4.8), and those into (4.1), and integrate over all the frequencies and then over the $\mathbf{Q}$-space, and get

$$\widetilde{W}_d^{\xi}(\boldsymbol{\mathscr{A}}_\mu^\pm) = \frac{E_g^2 A_0^2 d_\parallel^2}{\hbar^3} \int_0^\infty \mathrm{d}Q\, Q |\Delta_B^\xi(Q)|^2 |\tilde{u}_1^{LG}(Q/\sqrt{\epsilon})|^2, \tag{4.30}$$

using Eq. (2.24), we obtain the spectral function

$$\widetilde{\mathscr{g}}_{d,\boldsymbol{\mathscr{A}}_\mu^+}^{\xi}(E) = \eta\, |\Delta_B^\xi\big(f_\xi(E)\big)|^2 \left(\frac{2M_b}{\hbar^2}\right) \left(\frac{w_0^2 f_\xi(E)^2}{2\epsilon}\right) e^{-\frac{w_0^2 f_\xi(E)^2}{2\epsilon}}, \tag{4.31}$$

where $f_\xi(E) = \sqrt{2M_d(E - \xi g_d \mathscr{B}_\perp)}/\hbar$.

Spectral functions for the K and K' valley excitons are shown in Fig. 4.7, where the value of dark exciton g-factor is the one for MoS_2, namely $g_d = -6.5$. These spectral functions do not differ much from the ones obtained without the out-of-plane magnetic field, but now the splitting between the energy states is caused by the Zeeman interaction and not the valley exchange interaction.

5. TIGHTLY FOCUSED CYLINDRICALLY POLARISED FIELDS

So far, we have considered electromagnetic fields of form $u(\mathbf{r})e^{ik_0 z}\hat{\mathbf{f}}$, which are not actually solutions to the Maxwell equation, as they do not satisfy the transversality condition. A bona fide electromagnetic field with more complex amplitude pattern than a plane wave has a longitudinal component in the electric and/or magnetic field [93]. This longitudinal component is typically really weak for paraxial fields. However, tightly focused fields, especially cylindrically polarised ones, can have a strong longitudinal component, which can be useful in some applications. In this chapter, we are interested in the full vectorial form of the magnetic field of cylindrically polarised modes, as with sufficiently intense light beam, we could induce brightening of the dark excitons in TMDs.

5.1 Full vector solutions of tightly focused cylindrically polarised light

To obtain the proper vectorial form of the electric and magnetic field, we follow the method shown in Ref. [94], where the vector potentials of cylindrically polarised modes in Eq. (3.26) get demoted into the role of Hertz potentials of the electromagnetic field [76, 77]. We obtain the TM (transverse magnetic) electric and magnetic field via following equations:

$$\boldsymbol{\mathscr{E}}_{\boldsymbol{\mathscr{A}}_\mu^\pm} = \nabla \times (\nabla \times \boldsymbol{\mathscr{A}}_\mu^\pm), \tag{5.1a}$$

$$\mathbf{B}_{\boldsymbol{\mathscr{A}}_\mu^\pm} = \frac{1}{c^2}\frac{\partial}{\partial t}(\nabla \times \boldsymbol{\mathscr{A}}_\mu^\pm), \tag{5.1b}$$

and the TE (transverse electric) fields can be derived by exchanging the role of the electric and magnetic field, and applying an extra minus sign between the TE electric field and TM magnetic field, namely letting $\mathbf{B}_{TM} \mapsto -\boldsymbol{\mathscr{E}}_{TE}$ and $\boldsymbol{\mathscr{E}}_{TM} \mapsto \mathbf{B}_{TE}$.

From Eq. (5.1a), we obtain the full vectorial expressions of the TM electric fields for cylindrically polarised beams, given explicitly, in their unnormalised form, at the plane $z = 0$, and $t = 0$, in the cylindrical coordinates $\{r, \theta, z\}$, as follows:

$$\mathscr{E}^r_{\mathscr{A}^+_R} = \frac{r}{k^2 w_0^9} e^{-\frac{r^2}{w_0^2}} \left[k^4 w_0^8 + 4k^2 w_0^4 \left(r^2 - 2w_0^2\right) + 4\left(r^4 - 6r^2 w_0^2 + 6w_0^4\right) \right], \tag{5.2a}$$

$$\mathscr{E}^\theta_{\mathscr{A}^+_R} = 0, \tag{5.2b}$$

$$\mathscr{E}^z_{\mathscr{A}^+_R} = \frac{2}{k w_0^7} i e^{-\frac{r^2}{w_0^2}} \left[k^2 w_0^4 \left(w_0^2 - r^2\right) - 2\left(r^4 - 4r^2 w_0^2 + 2w_0^4\right) \right], \tag{5.2c}$$

for the co-rotating radially polarised field,

$$\mathscr{E}^r_{\mathscr{A}^+_A} = 0, \tag{5.3a}$$

$$\mathscr{E}^\theta_{\mathscr{A}^+_A} = \frac{1}{k^2 w_0^9} r e^{-\frac{r^2}{w_0^2}} \left[k^4 w_0^8 + 4\left(r^4 - 6r^2 w_0^2 + 6w_0^4\right) \right], \tag{5.3b}$$

$$\mathscr{E}^z_{\mathscr{A}^+_A} = 0, \tag{5.3c}$$

for the co-rotating azimuthally polarised field,

$$\mathscr{E}^r_{\mathscr{A}^-_R} = \frac{r\cos(2\theta)}{-k^2 w_0^9} e^{-\frac{r^2}{w_0^2}} \left[k^4 w_0^8 - 4k^2 w_0^4 \left(w_0^2 - r^2\right) + 4\left(r^4 - 6r^2 w_0^2 + 6w_0^4\right) \right], \tag{5.4a}$$

$$\mathscr{E}^\theta_{\mathscr{A}^-_R} = \frac{1}{k^2 w_0^9} r\sin(2\theta) e^{-\frac{r^2}{w_0^2}} \left[k^4 w_0^8 - 4k^2 w_0^6 + 4\left(r^4 - 6r^2 w_0^2 + 6w_0^4\right) \right], \tag{5.4b}$$

$$\mathscr{E}^z_{\mathscr{A}^-_R} = \frac{2}{k w_0^7} i r^2 \cos(2\theta) e^{-\frac{r^2}{w_0^2}} \left[k^3 w_0^4 + 2k\left(r^2 - 3w_0^2\right) \right] \tag{5.4c}$$

for the counter-rotating radially polarised field, and

$$\mathscr{E}^r_{\mathscr{A}^-_A} = \frac{r\sin(2\theta)}{k^2 w_0^9} e^{-\frac{r^2}{w_0^2}} \left[k^4 w_0^8 - 4k^2 w_0^4 \left(w_0^2 - r^2\right) + 4\left(r^4 - 6r^2 w_0^2 + 6w_0^4\right) \right], \tag{5.5a}$$

$$\mathscr{E}^\theta_{\mathscr{A}^-_A} = \frac{1}{k^2 w_0^9} r\cos(2\theta) e^{-\frac{r^2}{w_0^2}} \left[k^4 w_0^8 - 4k^2 w_0^6 + 4\left(r^4 - 6r^2 w_0^2 + 6w_0^4\right) \right], \tag{5.5b}$$

$$\mathscr{E}^z_{\mathscr{A}^-_A} = \frac{-2}{k w_0^7} i r^2 \sin(2\theta) e^{-\frac{r^2}{w_0^2}} \left[k^3 w_0^4 + 2k\left(r^2 - 3w_0^2\right) \right], \tag{5.5c}$$

for the counter-rotating azimuthally polarised field.

We obtain the TM magnetic fields from in similar manner, using Eq. (5.1b):

$$B^r_{\mathscr{A}^+_R} = 0, \tag{5.6a}$$

$$B^\theta_{\mathscr{A}^+_R} = -\frac{ir}{c w_0^5} e^{-\frac{r^2}{w_0^2}} \left(k^2 w_0^4 + 2r^2 - 4w_0^2 \right), \tag{5.6b}$$

$$B^z_{\mathscr{A}^+_R} = 0, \tag{5.6c}$$

for the co-rotating radially polarised (electric) field,

$$B^r_{\mathscr{A}^+_A} = \frac{ir}{cw_0^5} e^{-\frac{r^2}{w_0^2}} \left(k^2 w_0^4 + 2r^2 - 4w_0^2\right), \tag{5.7a}$$

$$B^\theta_{\mathscr{A}^+_A} = 0, \tag{5.7b}$$

$$B^z_{\mathscr{A}^+_A} = \frac{2}{cw_0^3} k e^{-\frac{r^2}{cw_0^2}} \left(r^2 - w_0^2\right), \tag{5.7c}$$

for the co-rotating azimuthally polarised (electric) field,

$$B^r_{\mathscr{A}^-_R} = \frac{ir\sin(2\theta)}{cw_0^5} e^{-\frac{r^2}{w_0^2}} \left(k^2 w_0^4 + 2r^2 - 4w_0^2\right), \tag{5.8a}$$

$$B^\theta_{\mathscr{A}^-_R} = \frac{ir\cos(2\theta)}{cw_0^5} e^{-\frac{r^2}{w_0^2}} \left(k^2 w_0^4 + 2r^2 - 4w_0^2\right), \tag{5.8b}$$

$$B^z_{\mathscr{A}^-_R} = \frac{2}{cw_0^3} k r^2 \sin(2\theta) e^{-\frac{r^2}{w_0^2}}, \tag{5.8c}$$

for the counter-rotating radially polarised (electric) field, and

$$B^r_{\mathscr{A}^-_A} = \frac{ir\cos(2\theta)}{cw_0^5} e^{-\frac{r^2}{w_0^2}} \left(k^2 w_0^4 + 2r^2 - 4w_0^2\right), \tag{5.9a}$$

$$B^\theta_{\mathscr{A}^-_A} = -\frac{ir\sin(2\theta)}{cw_0^5} e^{-\frac{r^2}{w_0^2}} \left(k^2 w_0^4 + 2r^2 - 4w_0^2\right), \tag{5.9b}$$

$$B^z_{\mathscr{A}^-_A} = \frac{2}{cw_0^3} k r^2 \cos(2\theta) e^{-\frac{r^2}{w_0^2}}, \tag{5.9c}$$

for the counter-rotating azimuthally polarised (electric) field. The TE electric and magnetic fields can be obtained by exchanging the roles of electric and magnetic fields, together with an extra minus sign, as described above.

Fig. 5.1 shows the polarisation structure and the intensity distribution of the in-plane magnetic fields $|\mathbf{B}_\parallel|^2 = |\mathbf{B}_x|^2 + |\mathbf{B}_y|^2$ of the cylindrically polarised modes. The beam is defined by the beam waist $w_0 = 1$ μm and wavelength $\lambda \simeq 700$ nm. We have normalised the magnetic field values with respect to the maximum values of the co-rotating radially polarised mode, which has the highest values for the parallel magnetic fields, due to it not having a longitudinal component, in contrast to other modes, as will be shown in Fig. 5.2. Note that we see that the polarisation structure of the magnetic field is the opposite to the one for the electric field, as magnetic field has to be perpendicular to the electric field at every point, i.e., for radially polarised mode, we have azimuthally polarised magnetic field and vice versa, which is expected as the electric and magnetic field have to be perpendicular to each other at every point in space.

Fig. 5.2 shows the intensity distribution of the longitudinal component of the magnetic field $|\mathbf{B}_\perp|^2 = |\mathbf{B}_z|^2$, where the parameters used are the same as above. The values are

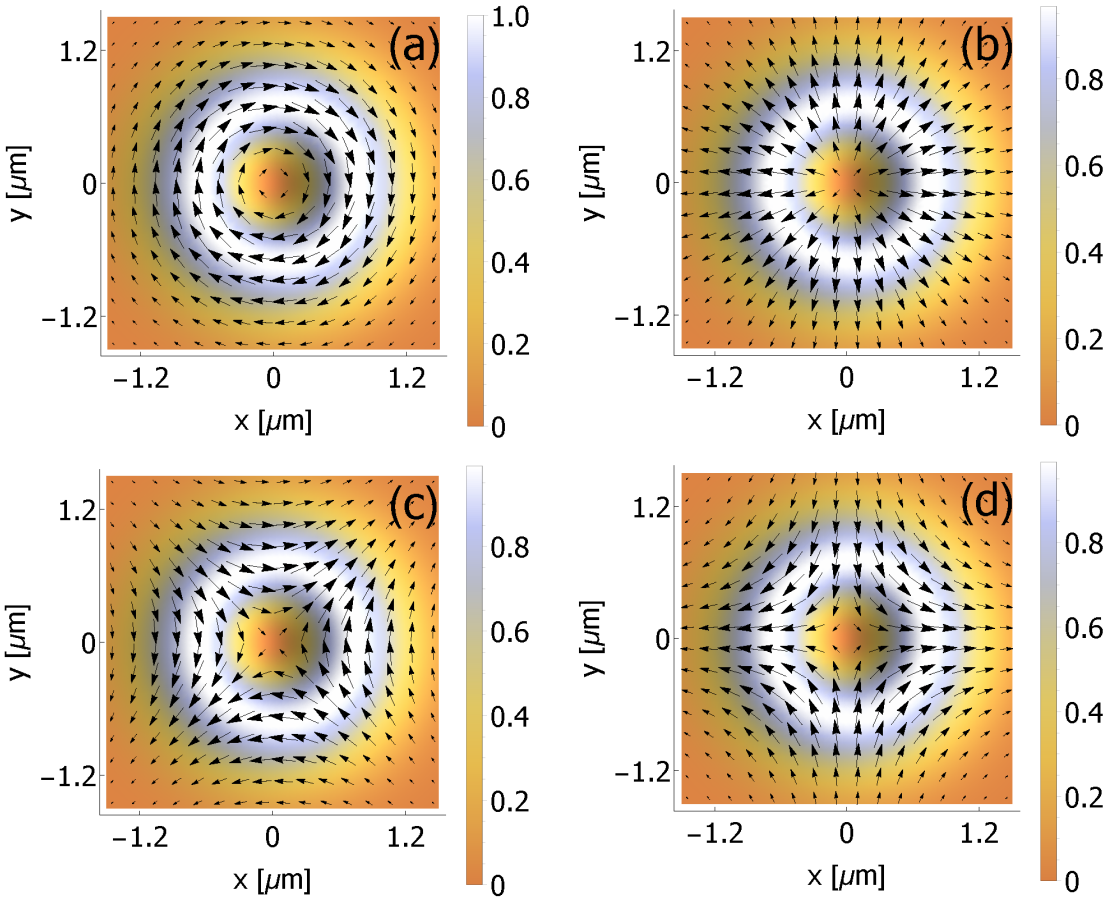

Figure 5.1. *In-plane magnetic field intensity distribution* $|\mathbf{B}_{\parallel}|^2 = |\mathbf{B}_x|^2 + |\mathbf{B}_y|^2$*, for tightly focused cylindrically polarised modes, and the polarisation profile of those modes. In panel (a) is for the co-rotating radially polarised modes, and in panel (b) we have for the co-rotating azimuthally polarised mode. In panels (c) and (d) we have in-plane magnetic fields for the counter-rotating radially and azimuthally polarised modes, respectively. The values are normalised with respect to the maximum value of the co-rotating radially polarised mode. Note that we see that the polarisation structure is the opposite to the electric field, as magnetic field has to be perpendicular to the electric field at every point. The parameters that define our beam are* $w_0 = 1$ *μm, and wavelength* $\lambda \simeq 700$ *nm.*

normalised with respect to the maximum value of parallel magnetic field for the co-rotating radially polarised mode, shown in Fig. 5.1. We see that the co-rotating radially polarised mode does not have longitudinal magnetic field, while the co-rotating azimuthally polarised beam has a strong magnetic field at its focus. For both counter-rotating modes, we see a four-leaf clover structure for the magnetic field. The strongest longitudinal magnetic fields are achieved for the co-rotating azimuthally polarised mode, whereas the counter-rotating modes have considerably lower values.

In order to have a significant impact on the exciton states in TMD, such as brighten the dark excitons, the magnetic field should be of the order of Teslas, as discussed in Chapter 4. To achieve such high values, the beam power would need to be really large, even for tightly focused beam. This perhaps could be possible using ultrashort pulses, which can achieve high peak power, while having considerably low average power. There is

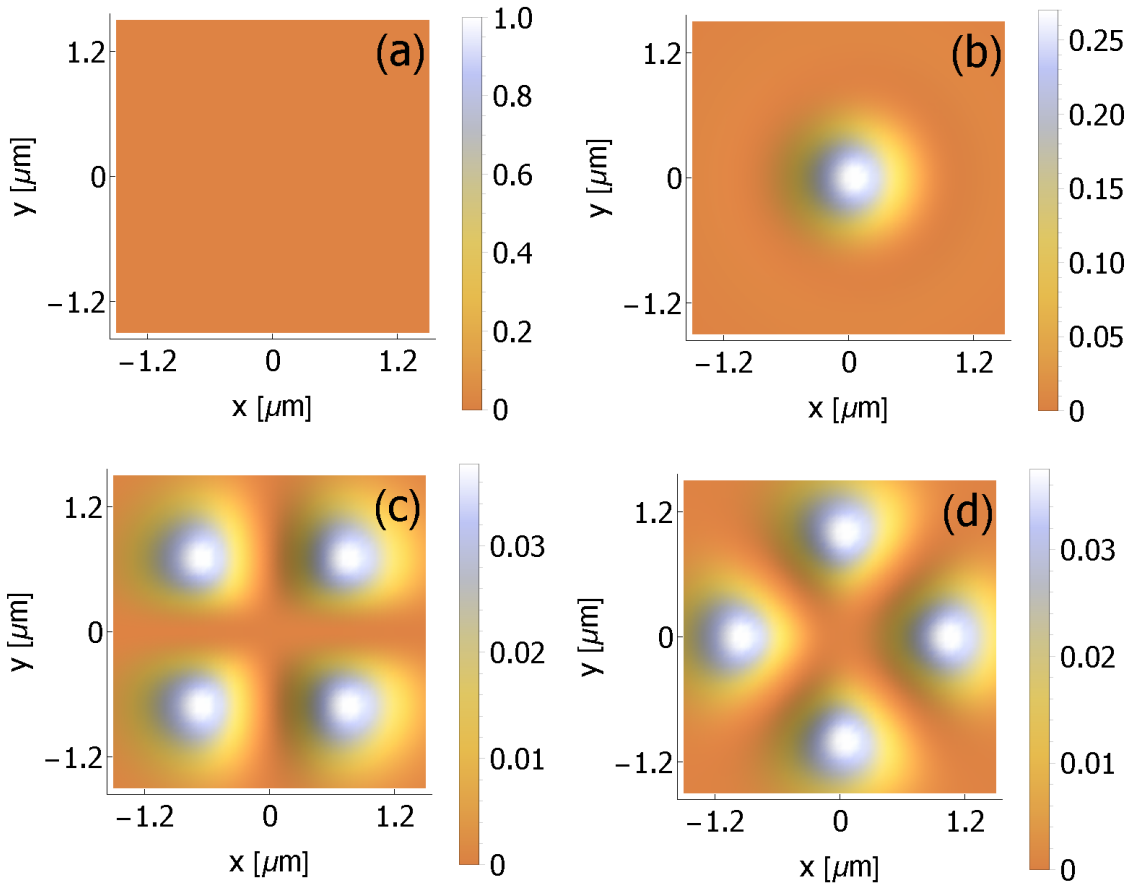

Figure 5.2. *Longitudinal magnetic field intensity distribution $|\mathbf{B}_\perp|^2 = |\mathbf{B}_z|^2$, for tightly focused cylindrically polarised electromagnetic modes. Panel (a) is for the co-rotating radially polarised mode, which has no longitudinal component for the magnetic field, and in panel (b) we have for the co-rotating azimuthally polarised mode, which has a strong magnetic field at its focus. In panel (c) and (d) we have the longitudinal magnetic fields for the counter-rotating radially and azimuthally polarised modes, respectively, with four-leaf clover structure for both modes. The values are normalised with respect to the maximum value of parallel magnetic field for the co-rotating radially polarised mode. The magnetic field is substantially smaller for the counter-rotating modes than for the co-rotating azimuthally polarised mode. The parameters that define our beam are $w_0 = 1$ μm, and wavelength $\lambda \simeq 700$ nm.*

a damage threshold limit for the peak fluence of the beam, where the TMD becomes damaged, thus the power of the beam cannot beam arbitrarily high [95]. This makes it challenging to achieve this strong magnetic fields for the light beams, as the high beam power combined with the tight focusing might lead to damaged TMD sample, thus making experimental realisations impossible. Nevertheless, the magnetic fields for cylindrically polarised modes are higher than for uniformly polarised light beams, and perhaps with very short pulse these magnetic fields can be achieved, as using the magnetic field of these beams would be really interesting prospect.

In order to simulate the LMI of TMD excitons for tightly focused cylindrically polarised light beams, we would first need to redefine the vector potential of our light, as the paraxial vector potential is not a good vector potential anymore, and is demoted into the role of a Hertz potential, and the new vector potential for the TM fields would be $\boldsymbol{\mathcal{A}}_{TF}(\mathbf{r}, t) =$

$-\int_0^t \mathrm{d}t' \nabla \times (\nabla \times \boldsymbol{\mathscr{A}}_{PA}(\mathbf{r}, t'))$, where TF stands for tightly focused and PA stands for paraxial. For the TE fields, the vector potential would be $\boldsymbol{\mathscr{A}}_{TF}(\mathbf{r}, t) = \nabla \times \boldsymbol{\mathscr{A}}_{PA}(\mathbf{r}, t)$. Also, the angular spectrum of our fields would need to be recalculated, as the beam is not a sum of LG beams anymore, but a superposition of its partial derivatives.

6. CONCLUSION AND OUTLOOK

In this thesis, we investigated the dynamics of exciton fine structure in monolayer TMDs excited by cylindrically polarised light. We also looked at the case when an external magnetic field is present, which, depending on the orientation of the magnetic field, can change the exciton bands of TMD and also brighten the dark excitons to couple with light in the case of the magnetic field being in the plane of the TMD.

We did the simulations for MoS_2, due to its material characteristics being best known at this moment. The formulas given here are, however, completely general and can be used for any of the TMDs mentioned in this thesis, given that their characteristic parameters are known. We used all four different modes of the cylindrically polarised, namely the co- and counter-rotating radially polarised modes and the co- and counter-rotating azimuthally polarised modes, all of which are the four basis vectors of the space spanned by the transverse orthogonal linear polarisation vectors and the first order HG-modes.

The LMI of excitons with light was simulated by calculating the spectral functions of the exciton bands as a function of energy, using the Fermi golden rule. The spectral function of an exciton can be regarded as the distribution of the total rate of transition to the band, giving the energy distribution of photons which will excite the exciton band. This will give the indication how the particular TMD interacts with light and will also predict the PL spectra of the TMD given that thermal dynamics are also taken into account.

First, we investigated the bright exciton interaction with the cylindrically polarised light beams. The results indicated that the counter-rotating modes do not lead to different spectral function compared to the uniformly polarised LG beams with $|\ell| = 1$, reported in Ref. [29]. Co-rotating modes, on the other hand, show selective photoexcitation of the bright exciton bands: co-rotating azimuthally polarised light only excites transition into the lower, parabolic particle like band of the two bright exciton bands, whereas for co-rotating radially polarised light it is the other way around: it only excites transitions into the linear light-like band, giving the possibility to tune exciton population in the bands by switching between the co-rotating cylindrically polarised modes.

The bright exciton states start to exhibit different response to light when they are under a magnetic field which is perpendicular to the TMD plane: the Zeeman interaction with an out-of-plane magnetic field $|\mathbf{B}_\perp| = 10$ T split the two bands apart by a few hundred

meV. The magnetic field also made the parabolic band linear for small values of exciton center-of-mass momentum, i.e., photon energies close to the band edge. This lead to significant broadening of the parabolic band spectral function, for each cylindrically polarised beam. Also, contrary to the case when $\mathbf{B}_\perp = 0$, both co-rotating beams can now excite transitions to both bands. For radially polarised beams, the ratio between the total transitions into the particle-like band and the light-like band was about 10%, and vice versa for azimuthally polarised beam, for the case when $|\mathbf{B}_\perp| = 10$ T. This gives the possibility to fine-tune the exciton population in these bands by using tunable out-of-plane magnetic field on the TMD.

After investigating the dynamics of bright exciton states, we turned our attention on the dark exciton states and their LMI when the in-plane magnetic field was present, which lead to these states to couple with light. We used the in-plane magnetic field with magnitude $|\mathbf{B}_\parallel| = 10$ T, and did not consider its direction, as it did not have an impact in our case. For all cylindrically polarised modes, the brightened dark states had the total transition rate of about 0.2% of the transition rate of the bright ones, leading to low amount of excitations even with this considerably strong magnetic field. The result is similar to ones obtained in experimental studies, and these low amount of excitations can be seen in the PL spectra, when thermal population is taken into account in equilibrium, which can make the dark excitons even dominate the PL spectra [21, 22, 27].

For the co-rotating modes, the spectral functions for brightened excitons were the same. For the counter-rotating modes, these spectral functions had an extra term, which lowered the spectral functions for the counter-rotating radially polarised beam and lowered it for azimuthally polarised beams, compared to the co-rotating modes. This added term was pretty small however, about 5% of the peak of co-rotating modes, and might be hard to be seen in the absorption spectra in experiments, but might give the possibility to tune the dark exciton population with this dependence on the cylindrical polarisation mode.

We finally looked at the case when also out-of-plane magnetic field was present. In this case, we neglected the exchange interactions between the electrons and holes, and only looked at the transitions in the single-valley of the Brillouin zone. In this case, the spectral functions were the same for all cylindrically polarised modes, and the magnitude of the spectral functions were similar to the case when out-of-plane magnetic field was not present. In this case, Zeeman interaction with out-of-plane magnetic field $|\mathbf{B}_\perp| = 3$ T caused also an about 800 meV splitting between the dark exciton levels, similar to the splitting caused by the exchange interaction.

Last, we looked at how tightly focused cylindrically polarised fields could be used in generating the magnetic fields needed for brightening the dark excitons. We showed that by going from the paraxial to nonparaxial case, we need to demote our paraxial vector potential to a Hertz potential, which gives solutions where strongly focused electromagnetic

field with co-rotating azimuthally polarised electric field has a strong longitudinal magnetic field component at its focus, as well as all field components becoming stronger when focused. However, to achieve magnetic fields of the order of Teslas, as needed to have a noticeable effect on the exciton states, we would need to use an ultrashort pulsed beam with high peak power, which could lead to damaged TMD sample [95]. Nevertheless, the magnetic field of tightly focused cylindrically polarised light beams are larger than uniformly polarised ones, thus, in principle, using the magnetic field of these beams is an interesting prospect.

Future work would be to reproduce these calculations with tightly focused beams, for which the vector potential of the paraxial case is not a good vector potential anymore, and is demoted into the role of a Hertz potential, and the calculations would need to be done with the new vector potential, and because the field does not consist of LG-modes anymore but its derivatives, we would also calculate new angular spectra and use them.

REFERENCES

[1] Novoselov, K. S. et al. Electric Field Effect in Atomically Thin Carbon Films. *Science* 306.5696 (2004), pp. 666–669. DOI: 10.1126/science.1102896.

[2] Novoselov, K. S. et al. Two-dimensional atomic crystals. *Proceedings of the National Academy of Sciences* 102.30 (2005), pp. 10451–10453. DOI: 10.1073/pnas.0502848102.

[3] Novoselov, K. S. et al. A roadmap for graphene. *Nature (London)* 490.7419 (2012), pp. 192–200. ISSN: 0028-0836. DOI: 10.1038/nature11458.

[4] Nair, R. R. et al. Fine Structure Constant Defines Visual Transparency of Graphene. *Science* 320.5881 (2008), pp. 1308–1308. DOI: 10.1126/science.1156965.

[5] Liu, X. et al. Emerging Low-Dimensional Materials for Nonlinear Optics and Ultrafast Photonics. *Advanced Materials* 29.14 (2017), p. 1605886. DOI: https://doi.org/10.1002/adma.201605886.

[6] Butler, S. Z. et al. Progress, Challenges, and Opportunities in Two-Dimensional Materials Beyond Graphene. *ACS Nano* 7.4 (2013). PMID: 23464873, pp. 2898–2926. DOI: 10.1021/nn400280c.

[7] Rasmussen, F. A. and Thygesen, K. S. Computational 2D Materials Database: Electronic Structure of Transition-Metal Dichalcogenides and Oxides. *The Journal of Physical Chemistry C* 119.23 (2015), pp. 13169–13183. DOI: 10.1021/acs.jpcc.5b02950.

[8] Wilson, J. and Yoffe, A. The transition metal dichalcogenides discussion and interpretation of the observed optical, electrical and structural properties. *Advances in physics* 18.73 (1969), pp. 193–335. ISSN: 0001-8732. DOI: 10.1080/00018736900101307.

[9] Shishidou, T. et al. Effect of GGA on the half-metallicity of the itinerant ferromagnet CoS_2. *Phys. Rev. B* 64.18 (Oct. 2001), p. 180401. DOI: 10.1103/PhysRevB.64.180401.

[10] Fivaz, R. and Mooser, E. Electron-Phonon Interaction in Semiconducting Layer Structures. *Phys. Rev.* 136.3A (Nov. 1964), A833–A836. DOI: 10.1103/PhysRev.136.A833.

[11] Ye, J. T. et al. Superconducting Dome in a Gate-Tuned Band Insulator. *Science* 338.6111 (2012), pp. 1193–1196. DOI: 10.1126/science.1228006.

[12] Wang, G. et al. Colloquium: Excitons in atomically thin transition metal dichalcogenides. *Rev. Mod. Phys.* 90.2 (Apr. 2018), p. 021001. DOI: 10.1103/RevModPhys.90.021001.

[13] Jariwala, D. et al. Emerging Device Applications for Semiconducting Two-Dimensional Transition Metal Dichalcogenides. *ACS Nano* 8.2 (2014). PMID: 24476095, pp. 1102–1120. DOI: 10.1021/nn500064s.

[14] Mak, K. F. et al. Atomically Thin $\mathrm{MoS_2}$: A New Direct-Gap Semiconductor. *Phys. Rev. Lett.* 105.13 (Sept. 2010), p. 136805. DOI: 10.1103/PhysRevLett.105.136805.

[15] Xiao, D. et al. Coupled Spin and Valley Physics in Monolayers of $\mathrm{MoS_2}$ and Other Group-VI Dichalcogenides. *Phys. Rev. Lett.* 108.19 (May 2012), p. 196802. DOI: 10.1103/PhysRevLett.108.196802.

[16] Zhu, Z. Y. et al. Giant spin-orbit-induced spin splitting in two-dimensional transition-metal dichalcogenide semiconductors. *Phys. Rev. B* 84.15 (Oct. 2011), p. 153402. DOI: 10.1103/PhysRevB.84.153402.

[17] Splendiani, A. et al. Emerging Photoluminescence in Monolayer MoS2. *Nano Letters* 10.4 (2010). PMID: 20229981, pp. 1271–1275. DOI: 10.1021/nl903868w.

[18] Bernardi, M. et al. Extraordinary Sunlight Absorption and One Nanometer Thick Photovoltaics Using Two-Dimensional Monolayer Materials. *Nano Letters* 13.8 (2013). PMID: 23750910, pp. 3664–3670. DOI: 10.1021/nl401544y.

[19] Britnell, L. et al. Strong Light-Matter Interactions in Heterostructures of Atomically Thin Films. *Science* 340.6138 (2013), pp. 1311–1314. DOI: 10.1126/science.1235547.

[20] Zhao, L. et al. Strong exciton-photon interaction and lasing of two-dimensional transition metal dichalcogenide semiconductors. *Nano research* 14.6 (Sept. 2020), pp. 1937–1954. ISSN: 1998-0124. DOI: 10.1007/s12274-020-3073-5.

[21] Feierabend, M. et al. Brightening of spin- and momentum-dark excitons in transition metal dichalcogenides. *2D materials* 8.1 (Oct. 2020), pp. 15013–. ISSN: 2053-1583. DOI: 10.1088/2053-1583/abb876.

[22] Molas, M. R. et al. Brightening of dark excitons in monolayers of semiconducting transition metal dichalcogenides. *2D Materials* 4.2 (Jan. 2017), p. 021003. DOI: 10.1088/2053-1583/aa5521.

[23] Slobodeniuk, A. O. and Basko, D. M. Spin–flip processes and radiative decay of dark intravalley excitons in transition metal dichalcogenide monolayers. *2D Materials* 3.3 (Aug. 2016), p. 035009. DOI: 10.1088/2053-1583/3/3/035009.

[24] Molas, M. R. et al. Probing and Manipulating Valley Coherence of Dark Excitons in Monolayer $\mathrm{WSe_2}$. *Phys. Rev. Lett.* 123.9 (Aug. 2019), p. 096803. DOI: 10.1103/PhysRevLett.123.096803.

[25] Zhang, X.-X. et al. Magnetic brightening and control of dark excitons in monolayer $\mathrm{WSe_2}$. *Nature nanotechnology* 12.9 (June 2017), pp. 883–888. ISSN: 1748-3387. DOI: 10.1038/nnano.2017.105.

[26] Robert, C. et al. Measurement of the spin-forbidden dark excitons in MoS2 and MoSe2 monolayers. *Nature communications* 11.1 (2020), pp. 4037–4037. ISSN: 2041-1723. DOI: 10.1038/s41467-020-17608-4.

[27] Vasconcelos, R. et al. Dark exciton brightening and its engaged valley dynamics in monolayer $\mathrm{WSe_2}$. *Phys. Rev. B* 98.19 (Nov. 2018), p. 195302. DOI: 10.1103/PhysRevB.98.195302.

[28] Brem, S. et al. Phonon-Assisted Photoluminescence from Indirect Excitons in Monolayers of Transition-Metal Dichalcogenides. *Nano letters* 20.4 (Feb. 2020), pp. 2849–2856. ISSN: 1530-6984. DOI: 10.1021/acs.nanolett.0c00633.

[29] Simbulan, K. B. et al. Selective Photoexcitation of Finite-Momentum Excitons in Monolayer MoS_2 by Twisted Light. *ACS nano* 15.2 (Feb. 2021), pp. 3481–3489. ISSN: 1936-0851. DOI: 10.1021/acsnano.0c10823.

[30] Wu, L. et al. Polarized photoluminescence spectroscopy in WS_2, WSe_2 atomic layers and heterostructures by cylindrical vector beams. *Chinese Physics B* 30.8 (Aug. 2021), p. 087802. DOI: 10.1088/1674-1056/abf3b6.

[31] Borghardt, S. et al. Radially polarized light beams from spin-forbidden dark excitons and trions in monolayer WSe2. *Opt. Mater. Express* 10.5 (May 2020), pp. 1273–1285. DOI: 10.1364/OME.388913.

[32] Robert, C. et al. Fine structure and lifetime of dark excitons in transition metal dichalcogenide monolayers. *Phys. Rev. B* 96.15 (Oct. 2017), p. 155423. DOI: 10.1103/PhysRevB.96.155423.

[33] Quabis, S. et al. Focusing light to a tighter spot. *Optics Communications* 179.1 (2000), pp. 1–7. ISSN: 0030-4018. DOI: https://doi.org/10.1016/S0030-4018(99)00729-4.

[34] Zurita-Sánchez, J. R. and Novotny, L. Multipolar interband absorption in a semiconductor quantum dot. II. Magnetic dipole enhancement. *J. Opt. Soc. Am. B* 19.11 (Nov. 2002), pp. 2722–2726. DOI: 10.1364/JOSAB.19.002722.

[35] Holleczek, A. et al. Classical and quantum properties of cylindrically polarized states of light. *Opt. Express* 19.10 (May 2011), pp. 9714–9736. DOI: 10.1364/OE.19.009714.

[36] Quinteiro, G. F. et al. Formulation of the twisted-light–matter interaction at the phase singularity: Beams with strong magnetic fields. *Phys. Rev. A* 95.1 (Jan. 2017), p. 012106. DOI: 10.1103/PhysRevA.95.012106.

[37] Geim, A. K. and Novoselov, K. S. The rise of graphene. *Nature materials* 6.3 (2007), pp. 183–191. ISSN: 1476-1122. DOI: 10.1038/nmat1849.

[38] Ganatra, R. and Zhang, Q. Few-Layer MoS_2: A Promising Layered Semiconductor. *ACS nano* 8.5 (Mar. 2014). PMID: 24660756, pp. 4074–4099. ISSN: 1936-0851. DOI: 10.1021/nn405938z.

[39] Radisavljevic, B. et al. Single-layer MoS2 transistors. *Nature nanotechnology* 6.3 (2011), pp. 147–150. ISSN: 1748-3387. DOI: 10.1038/nnano.2010.279.

[40] Mueller, T. and Malic, E. Exciton physics and device application of two-dimensional transition metal dichalcogenide semiconductors. *NPJ 2D materials and applications* 2.1 (2018). ISSN: 2397-7132. DOI: 10.1038/s41699-018-0074-2.

[41] Chhowalla, M. et al. The chemistry of two-dimensional layered transition metal dichalcogenide nanosheets. *Nature chemistry* 5.4 (2013), pp. 263–275. ISSN: 1755-4330. DOI: 10.1038/nchem.1589.

[42] Ataca, C. et al. Stable, Single-Layer MX2 Transition-Metal Oxides and Dichalcogenides in a Honeycomb-Like Structure. *The Journal of Physical Chemistry C* 116.16 (2012), pp. 8983–8999. DOI: 10.1021/jp212558p.

[43] Zhan, Y. et al. Large-Area Vapor-Phase Growth and Characterization of MoS2 Atomic Layers on a SiO2 Substrate. *Small* 8.7 (2012), pp. 966–971. DOI: https://doi.org/10.1002/smll.201102654.

[44] Cappelluti, E. et al. Tight-binding model and direct-gap/indirect-gap transition in single-layer and multilayer MoS_2. *Phys. Rev. B* 88.7 (Aug. 2013), p. 075409. DOI: 10.1103/PhysRevB.88.075409.

[45] Zhao, W. et al. Origin of Indirect Optical Transitions in Few-Layer MoS2, WS2, and WSe2. *Nano Letters* 13.11 (2013). PMID: 24168432, pp. 5627–5634. DOI: 10.1021/nl403270k.

[46] Roldán, R. et al. Electronic properties of single-layer and multilayer transition metal dichalcogenides MX2 (M = Mo, W and X = S, Se). *Annalen der Physik* 526.9-10 (2014), pp. 347–357. DOI: https://doi.org/10.1002/andp.201400128.

[47] Wang, Q. H. et al. Electronics and optoelectronics of two-dimensional transition metal dichalcogenides. *Nature nanotechnology* 7.11 (2012), pp. 699–712. ISSN: 1748-3387. DOI: 10.1038/nnano.2012.193.

[48] Han, B. et al. Exciton States in Monolayer $\mathrm{MoSe_2}$ and $\mathrm{MoTe_2}$ Probed by Upconversion Spectroscopy. *Phys. Rev. X* 8.3 (Sept. 2018), p. 031073. DOI: 10.1103/PhysRevX.8.031073.

[49] Yao, W. et al. Valley-dependent optoelectronics from inversion symmetry breaking. *Phys. Rev. B* 77.23 (June 2008), p. 235406. DOI: 10.1103/PhysRevB.77.235406.

[50] Sallen, G. et al. Robust optical emission polarization in MoS_2 monolayers through selective valley excitation. *Phys. Rev. B* 86.8 (Aug. 2012), p. 081301. DOI: 10.1103/PhysRevB.86.081301.

[51] Cao, T. et al. Valley-selective circular dichroism of monolayer molybdenum disulphide. *Nature communications* 3.1 (2012), pp. 887–887. ISSN: 2041-1723. DOI: 10.1038/ncomms1882.

[52] Zeng, H. et al. Valley polarization in MoS2 monolayers by optical pumping. *Nature nanotechnology* 7.8 (2012), pp. 490–493. ISSN: 1748-3387. DOI: 10.1038/nnano.2012.95.

[53] Zibouche, N. et al. Transition-metal dichalcogenides for spintronic applications. *Annalen der Physik* 526.9-10 (Aug. 2014), pp. 395–401. DOI: https://doi.org/10.1002/andp.201400137.

[54] Ahn, E. C. 2D materials for spintronic devices. *NPJ 2D materials and applications* 4.1 (June 2020). ISSN: 2397-7132. DOI: 10.1038/s41699-020-0152-0.

[55] Xu, X. et al. Spin and pseudospins in layered transition metal dichalcogenides. *Nature physics* 10.5 (Apr. 2014), pp. 343–350. ISSN: 1745-2473. DOI: 10.1038/nphys2942.

[56] Mak, K. F. et al. Control of valley polarization in monolayer MoS_2 by optical helicity. *Nature nanotechnology* 7.8 (June 2012), pp. 494–498. ISSN: 1748-3387. DOI: 10.1038/nnano.2012.96.

[57] Ramasubramaniam, A. Large excitonic effects in monolayers of molybdenum and tungsten dichalcogenides. *Phys. Rev. B* 86.11 (Sept. 2012), p. 115409. DOI: 10.1103/PhysRevB.86.115409.

[58] Schäfer, W. and Wegener, M. *Semiconductor Optics and Transport Phenomena*. Advanced Texts in Physics. Berlin, Heidelberg: Springer Berlin Heidelberg, 2002. ISBN: 9783642082719.

[59] Hönerlage, B. and Pelant, I. *Symmetry and Symmetry-Breaking in Semiconductors: Fine Structure of Exciton States*. Vol. 279. Springer Tracts in Modern Physics (Volume 279). Cham: Springer International Publishing AG, 2018. ISBN: 3319942344.

[60] Koch, S. W. et al. Semiconductor excitons in new light. *Nature materials* 5.7 (2006), pp. 523–531. ISSN: 1476-1122. DOI: 10.1038/nmat1658.

[61] Yu, H. et al. Valley excitons in two-dimensional semiconductors. *National Science Review* 2.1 (Jan. 2015), pp. 57–70. ISSN: 2095-5138. DOI: 10.1093/nsr/nwu078.

[62] Chernikov, A. et al. Exciton Binding Energy and Nonhydrogenic Rydberg Series in Monolayer WS_2. *Phys. Rev. Lett.* 113.7 (Aug. 2014), p. 076802. DOI: 10.1103/PhysRevLett.113.076802.

[63] Qiu, D. Y. et al. Nonanalyticity, Valley Quantum Phases, and Lightlike Exciton Dispersion in Monolayer Transition Metal Dichalcogenides: Theory and First-Principles Calculations. *Phys. Rev. Lett.* 115.17 (Oct. 2015), p. 176801. DOI: 10.1103/PhysRevLett.115.176801.

[64] Zhu, B. et al. Exciton Binding Energy of Monolayer WS_2. *Scientific reports* 5.1 (Mar. 2015), pp. 9218–. ISSN: 2045-2322. DOI: 10.1038/srep09218.

[65] Ugeda, M. M. et al. Giant bandgap renormalization and excitonic effects in a monolayer transition metal dichalcogenide semiconductor. *Nature materials* 13.12 (Aug. 2014), pp. 1091–1095. ISSN: 1476-1122. DOI: 10.1038/nmat4061.

[66] Lu, Z. et al. Magnetic field mixing and splitting of bright and dark excitons in monolayer $MoSe_2$. *2D Materials* 7.1 (Nov. 2019), p. 015017. DOI: 10.1088/2053-1583/ab5614.

[67] Robert, C. et al. Excitonic properties of semiconducting monolayer and bilayer MoTe2. *Phys. Rev. B* 94.15 (Oct. 2016), p. 155425. DOI: 10.1103/PhysRevB.94.155425.

[68] Malic, E. et al. Dark excitons in transition metal dichalcogenides. *Phys. Rev. Materials* 2.1 (Jan. 2018), p. 014002. DOI: 10.1103/PhysRevMaterials.2.014002.

[69] Rohlfing, M. and Louie, S. G. Electron-Hole Excitations in Semiconductors and Insulators. *Phys. Rev. Lett.* 81.11 (Sept. 1998), pp. 2312–2315. DOI: 10.1103/PhysRevLett.81.2312.

[70] Peng, G.-H. et al. Distinctive Signatures of the Spin- and Momentum-Forbidden Dark Exciton States in the Photoluminescence of Strained WSe_2 Monolayers under Thermalization. *Nano Letters* 19.4 (Mar. 2019). PMID: 30860847, pp. 2299–2312. DOI: 10.1021/acs.nanolett.8b04786.

[71] Kormányos, A. et al. $\mathbf{k}\cdot\mathbf{p}$ theory for two-dimensional transition metal dichalcogenide semiconductors. *2D Materials* 2.2 (Apr. 2015), p. 022001. DOI: 10.1088/2053-1583/2/2/022001.

[72] Kormányos, A. et al. Spin-Orbit Coupling, Quantum Dots, and Qubits in Monolayer Transition Metal Dichalcogenides. *Phys. Rev. X* 4.1 (Mar. 2014), p. 011034. DOI: 10.1103/PhysRevX.4.011034.

[73] Dery, H. and Song, Y. Polarization analysis of excitons in monolayer and bilayer transition-metal dichalcogenides. *Phys. Rev. B* 92.12 (Sept. 2015), p. 125431. DOI: 10.1103/PhysRevB.92.125431.

[74] Wang, G. et al. In-Plane Propagation of Light in Transition Metal Dichalcogenide Monolayers: Optical Selection Rules. *Phys. Rev. Lett.* 119.4 (July 2017), p. 047401. DOI: 10.1103/PhysRevLett.119.047401.

[75] Echeverry, J. P. et al. Splitting between bright and dark excitons in transition metal dichalcogenide monolayers. *Phys. Rev. B* 93.12 (Mar. 2016), p. 121107. DOI: 10.1103/PhysRevB.93.121107.

[76] Jackson, J. D. *Classical electrodynamics*. 3. ed. New York: Wiley, 1998. ISBN: 0-471-43132-X.

[77] Stratton, J. A. *Electromagnetic theory*. New York: McGraw-Hill, 1941. ISBN: 0-07-062150-0.

[78] Born, M. et al. *Principles of Optics: Electromagnetic Theory of Propagation, Interference and Diffraction of Light*. 7th ed. Cambridge University Press, 1999. DOI: 10.1017/CBO9781139644181.

[79] Siegman, A. E. *Lasers*. Mill Valley, Calif: University Science Books, 1986. ISBN: 1-68015-237-8.

[80] Saleh, B. E. A. *Fundamentals of photonics*. Third edition. Wiley series in pure and applied optics. Hoboken, N.J: John Wiley & Sons, 2019. ISBN: 9781119506867.

[81] Arfken, G. B. *Mathematical methods for physicists*. 6th ed. Boston: Elsevier, 2005. ISBN: 0-12-059876-0.

[82] Mandel, L. and Wolf, E. *Optical Coherence and Quantum Optics*. Cambridge University Press, 1995. DOI: 10.1017/CBO9781139644105.

[83] Li, Y. et al. Measurement of the optical dielectric function of monolayer transition-metal dichalcogenides: $\mathrm{MoS_2}$, $\mathrm{MoSe_2}$, $\mathrm{WS_2}$, and $\mathrm{WSe_2}$. *Phys. Rev. B* 90.20 (Nov. 2014), p. 205422. DOI: 10.1103/PhysRevB.90.205422.

[84] Gabriel, C. et al. Entangling Different Degrees of Freedom by Quadrature Squeezing Cylindrically Polarized Modes. *Phys. Rev. Lett.* 106.6 (Feb. 2011), p. 060502. DOI: 10.1103/PhysRevLett.106.060502.

[85] Zhan, Q. Trapping metallic Rayleigh particles with radial polarization. *Opt. Express* 12.15 (July 2004), pp. 3377–3382. DOI: 10.1364/OPEX.12.003377.

[86] Sick, B. et al. Orientational Imaging of Single Molecules by Annular Illumination. *Phys. Rev. Lett.* 85.21 (Nov. 2000), pp. 4482–4485. DOI: 10.1103/PhysRevLett.85.4482.

[87] Berg-Johansen, S. et al. Classically entangled optical beams for high-speed kinematic sensing. *Optica* 2.10 (Oct. 2015), pp. 864–868. DOI: 10.1364/OPTICA.2.000864.

[88] Töppel, F. et al. Classical entanglement in polarization metrology. *New Journal of Physics* 16.7 (July 2014), p. 073019. DOI: 10.1088/1367-2630/16/7/073019.

[89] Meier, M. et al. Material processing with pulsed radially and azimuthally polarized laser radiation. *Applied Physics A* 86.3 (2007), pp. 329–334. ISSN: 0947-8396. DOI: 10.1007/s00339-006-3784-9.

[90] Shankar, R. *Principles of Quantum Mechanics*. Boston, MA: Springer US, 1994. ISBN: 0306447908.

[91] Loudon, R. *The Quantum Theory of Light*. OUP Oxford, 2000. ISBN: 9780191589782.

[92] Hofmann, P. *Solid state physics: an introduction*. 2nd ed. Physics textbook. Berlin: Wiley, 2015. ISBN: 3527412824.

[93] Aiello, A. and Ornigotti, M. Near field of an oscillating electric dipole and cross-polarization of a collimated beam of light: Two sides of the same coin. *American Journal of Physics* 82.9 (2014), pp. 860–868. DOI: 10.1119/1.4876936.

[94] Ornigotti, M. and Aiello, A. Radially and azimuthally polarized nonparaxial Bessel beams made simple. *Opt. Express* 21.13 (July 2013), pp. 15530–15537. DOI: 10.1364/OE.21.015530.

[95] Solomon, J. M. et al. Ultrafast multi-shot ablation and defect generation in monolayer transition metal dichalcogenides. *AIP Advances* 12.1 (2022), p. 015217. DOI: 10.1063/5.0078054.

APPENDIX A: EXCITON BASIS FUNCTIONS FROM SECOND QUANTISATION LANGUAGE

The exciton band energies $E^S_{\mathbf{Q}}$ and the electron-hole amplitudes in Eq. (2.1) are determined by the BSE [63, 69, 70]:

$$E_{cv,\mathbf{k},\mathbf{Q}}\Lambda^S_{vc,\mathbf{Q}}(\mathbf{k}) + \sum_{v'c'\mathbf{k}'} \langle vc,\mathbf{k},\mathbf{Q}|\hat{K}^{e-h}|v'c',\mathbf{k}',\mathbf{Q}\rangle \Lambda^S_{v'c',\mathbf{Q}}(\mathbf{k}') = E^S_{\mathbf{Q}}\Lambda^S_{vc,\mathbf{Q}}(\mathbf{k}), \quad \text{(A.1)}$$

where $|nn',\mathbf{k},\mathbf{Q}\rangle = \hat{c}^\dagger_{n,\mathbf{k}+\mathbf{Q}}\hat{c}_{n',\mathbf{k}}|GS\rangle$, $E_{cv,\mathbf{k},\mathbf{Q}} = E_{c,\mathbf{k}+\mathbf{Q}} - E_{v,\mathbf{k}}$ is the energy of free electron-hole pair, and $\hat{K}^{e-h}$ is the electron-hole interaction kernel consisting of both the direct Coulomb interaction term as well as the exchange interaction term. The detailed expressions of these terms are given in Ref. [63]

BSE equation is, in general, calculated numerically, with various methods, such as DFT and *GW*-method [7, 63], and the calculations become more accurate when a large amount of valence and conduction band basis states are used, with several hundred wavevectors at each band, leading to computationally heavy calculations [69], which can lead to heavily varying results, depending on the computational details [72].

To develop a semi-analytical model of exciton functions, the exciton states are calculated at the K and K' valleys, with $\mathbf{Q} = \mathbf{0}$, and those solutions are then taken as basis functions. In the limit $||\mathbf{Q}|| \ll 1$, the solutions then are given by intermixed states of these basis states, given by the Hamiltonian of the system, which usually is approximated with group theory and $\mathbf{k}\cdot\mathbf{p}$-expansion, using the symmetries of the system. [63, 71]

For the lowest four exciton states, two bright and two dark, at small $\mathbf{Q}$ limit, namely

$||\mathbf{Q}|| \ll 1$, the basis functions are given by single-valley pseudospinors [23, 24, 63]:

$$|\Psi^{K}_{b,\mathbf{Q}}\rangle \approx |e^{i\mathbf{Q}\cdot\mathbf{R}}\Psi^{K}_{b,\mathbf{0}}\rangle \equiv \begin{pmatrix} 1 \\ 0 \\ 0 \\ 0 \end{pmatrix}, \tag{A.2a}$$

$$|\Psi^{K'}_{b,\mathbf{Q}}\rangle \approx |e^{i\mathbf{Q}\cdot\mathbf{R}}\Psi^{K'}_{b,\mathbf{0}}\rangle \equiv \begin{pmatrix} 0 \\ 1 \\ 0 \\ 0 \end{pmatrix}, \tag{A.2b}$$

$$|\Psi^{K}_{b,\mathbf{Q}}\rangle \approx |e^{i\mathbf{Q}\cdot\mathbf{R}}\Psi^{K}_{d,\mathbf{0}}\rangle \equiv \begin{pmatrix} 0 \\ 0 \\ 1 \\ 0 \end{pmatrix}, \tag{A.2c}$$

$$|\Psi^{K'}_{b,\mathbf{Q}}\rangle \approx |e^{i\mathbf{Q}\cdot\mathbf{R}}\Psi^{K'}_{d,\mathbf{0}}\rangle \equiv \begin{pmatrix} 0 \\ 0 \\ 0 \\ 1 \end{pmatrix} \tag{A.2d}$$

where $|e^{i\mathbf{Q}\cdot\mathbf{R}}\Psi^{S}_{\tau,\mathbf{0}}\rangle = \frac{1}{\sqrt{\Omega}}\sum_{vc,\mathbf{k}} \Lambda^{S}_{\tau,vc,\mathbf{0}}(\mathbf{k})|vc,\mathbf{k},\mathbf{Q}\rangle$, and $\mathbf{R}$ is the center-of-mass position of the exciton at the plane of TMD.

The general form of the exciton bands are mixed states of the four basis functions given above. The effective Hamiltonian is dependent on the external potentials present on the system. For example, if external in-plane magnetic field is not present, bright and dark states are decoupled, so that they can be factored out into two 2x2 effective Hamiltonians. The effective Hamiltonian in various cases are given in Refs. [22–24, 29, 63]

APPENDIX B: CALCULATING THE EXPECTATION VALUES OF THE INTERACTION HAMILTONIAN

By inserting Eq. (2.1) into (4.1), we get the following expression for the expecation value:

$$\langle \Psi^S_{\mathbf{Q}} | \hat{H}_I | GS \rangle = \frac{1}{\Omega} \sum_{vc} \sum_{\mathbf{k}} \Lambda^{*S}_{vc,\mathbf{Q}}(\mathbf{k}) \langle GS | \hat{c}_{c,\mathbf{k}+\mathbf{Q}} \hat{c}^\dagger_{v,\mathbf{k}} \hat{H}_I | GS \rangle. \tag{B.1}$$

We now insert the resolution of identity ($\mathbb{I} = \sum_{n\mathbf{k}} |\psi_{n,\mathbf{k}}\rangle\langle\psi_{n,\mathbf{k}}|$), where $|\psi_{n,\mathbf{k}}\rangle$ is the Bloch-wavefunction of the quasiparticle in band n, on the left and right side of the interaction Hamiltonian $\hat{H}_I$, leading to following expression:

$$\begin{aligned}\langle \Psi^S_{\mathbf{Q}} | \hat{H}_I | GS \rangle = \frac{1}{\Omega} \sum_{vc\mathbf{k}} \sum_{n\mathbf{k}'} \sum_{m\mathbf{k}''} & \Lambda^{*S}_{vc,\mathbf{Q}}(\mathbf{k}) \langle GS | \hat{c}_{c,\mathbf{k}+\mathbf{Q}} \hat{c}^\dagger_{v,\mathbf{k}} | \psi_{n,\mathbf{k}'} \rangle \\ & \times \langle \psi_{n,\mathbf{k}'} | \hat{H}_I | \psi_{m,\mathbf{k}''} \rangle \langle \psi_{m,\mathbf{k}''} | GS \rangle. \end{aligned} \tag{B.2}$$

As $\hat{c}_{c,\mathbf{k}+\mathbf{Q}} \hat{c}^\dagger_{v,\mathbf{k}}$ are operators for different bands, they commute, we thus can calculate $\hat{c}_{c,\mathbf{k}+\mathbf{Q}} |\psi_{n,\mathbf{k}'}\rangle = \delta_{c,n}\delta_{\mathbf{k}+\mathbf{Q},\mathbf{k}'} |GS\rangle$. Then, by definition, $\hat{c}^\dagger_{v,\mathbf{k}} |GS\rangle = |\psi_{v,\mathbf{k}}\rangle$, we thus have an expression

$$\langle \Psi^S_{\mathbf{Q}} | \hat{H}_I | GS \rangle = \frac{1}{\Omega} \sum_{vc\mathbf{k}} \sum_{m,\mathbf{k}''} \langle GS | \psi_{v,\mathbf{k}} \rangle \langle \psi_{c,\mathbf{k}+\mathbf{Q}} | \hat{H}_I | \psi_{m,\mathbf{k}''} \rangle \langle \psi_{m,\mathbf{k}''} | GS \rangle \tag{B.3}$$

Finally, using that $\langle GS | \psi_{v,\mathbf{k}} \rangle \langle \psi_{m,\mathbf{k}''} | GS \rangle = \delta_{m,v}\delta_{\mathbf{k},\mathbf{k}''}$, we have the Eq. (4.3) in the main text:

$$\langle \Psi^S_{\mathbf{Q}} | \hat{H}_I | GS \rangle = \frac{1}{\sqrt{\Omega}} \sum_{vc} \sum_{\mathbf{k}} \Lambda^{*S}_{vc,\mathbf{Q}}(\mathbf{k}) \langle \psi_{c,\mathbf{k}+\mathbf{Q}} | \hat{H}_I | \psi_{v,\mathbf{k}} \rangle. \tag{B.4}$$

APPENDIX C: ELECTRIC DIPOLE APPROXIMATION OF THE INTERACTION HAMILTONIAN

The Bloch wavefunctions in the $\mathbf{k}$-space $|\psi_{n,\mathbf{k}}\rangle$ are explicitly written as follows:

$$|\psi_{n,\mathbf{k}}\rangle = e^{i\mathbf{k}\cdot\mathbf{r}}|u_n(\mathbf{k})\rangle, \tag{C.1}$$

Using Eq. (C.1), our terms $\langle\psi_{c,\mathbf{k}+\mathbf{Q}}|e^{i\mathbf{K}\cdot\mathbf{r}}\hat{\mathbf{p}}|\psi_{v,\mathbf{k}}\rangle$ in Eqs. (4.4) and (4.5) have the following form:

$$\langle\psi_{c,\mathbf{k}+\mathbf{Q}}|e^{i\mathbf{K}\cdot\mathbf{r}}\hat{\mathbf{p}}|\psi_{v,\mathbf{k}}\rangle = \langle u_c(\mathbf{k}+\mathbf{Q})|e^{-i(\mathbf{k}+\mathbf{Q})\cdot\mathbf{r}}e^{i\mathbf{K}\cdot\mathbf{r}}\hat{\mathbf{p}}e^{i\mathbf{k}\cdot\mathbf{r}}|u_v(\mathbf{k})\rangle. \tag{C.2}$$

By writing $\hat{\mathbf{p}} = -i\hbar\nabla$ [90], we can see that $\hat{\mathbf{p}}e^{i\mathbf{k}\cdot\mathbf{r}}|u_v(\mathbf{k})\rangle = e^{i\mathbf{k}\cdot\mathbf{r}}(\hbar\mathbf{k}+\hat{\mathbf{p}})|u_v(\mathbf{k})\rangle$, leading to term

$$\langle\psi_{c,\mathbf{k}+\mathbf{Q}}|e^{i\mathbf{K}\cdot\mathbf{r}}\hat{\mathbf{p}}|\psi_{v,\mathbf{k}}\rangle = \langle u_c(\mathbf{k}+\mathbf{Q})|e^{i(\mathbf{K}-\mathbf{Q})\cdot\mathbf{r}}(\hbar\mathbf{k}+\hat{\mathbf{p}})|u_v(\mathbf{k})\rangle. \tag{C.3}$$

We now insert the resolution of identity in $\mathbf{r}$, namely $\mathbb{I} = \int_{L^3}\mathrm{d}^3r\,|\mathbf{r}\rangle\langle\mathbf{r}|$, to transform from Bloch wavefunctions in the $\mathbf{k}$-space into the ones in the direct space:

$$\langle\psi_{c,\mathbf{k}+\mathbf{Q}}|e^{i\mathbf{K}\cdot\mathbf{r}}\hat{\mathbf{p}}|\psi_{v,\mathbf{k}}\rangle = \int_{L^3}\mathrm{d}^3r\,e^{i(\mathbf{K}-\mathbf{Q})}\psi^*_{c,\mathbf{k}+\mathbf{Q}}(\mathbf{r})(\hbar\mathbf{k}+\hat{\mathbf{p}})\psi_{v,\mathbf{k}}(\mathbf{r}), \tag{C.4}$$

where $\psi^*_{c,\mathbf{k}+\mathbf{Q}}(\mathbf{r}) = \langle u_c(\mathbf{k}+\mathbf{Q})|\mathbf{r}\rangle$, and $\psi_{v,\mathbf{k}}(\mathbf{r}) = \langle\mathbf{r}|u_v(\mathbf{k})\rangle$. We use the following expansion for the $\psi_{n,\mathbf{k}}(\mathbf{r})$, deriving from the $\mathbf{k}\cdot\mathbf{p}$-approximation:

$$\psi_{n,\mathbf{k}}(\mathbf{r}) \sim \frac{1}{L^{3/2}}u_{n,0}(\mathbf{r}), \tag{C.5}$$

where $u_{n,0}(\mathbf{r})$ has the periodicity of the crystal lattice of TMD [92]. We then have

$$\langle\psi_{c,\mathbf{k}+\mathbf{Q}}|e^{i\mathbf{K}\cdot\mathbf{r}}\hat{\mathbf{p}}|\psi_{v,\mathbf{k}}\rangle = \frac{1}{L^3}\int_{L^3}\mathrm{d}^3r\,e^{i(\mathbf{K}-\mathbf{Q})\cdot\mathbf{r}}u^*_{c,0}(\mathbf{r})(\hbar\mathbf{k}+\hat{\mathbf{p}})u_{v,0}(\mathbf{r}). \tag{C.6}$$

The integral above covers the whole volume of TMD. We will now replace it with an integral over a single unit cell, and sum the contributions of all unit cells covering the whole volume

of TMD. We do this by making the following substitutions:

$$\mathbf{r} \mapsto \mathbf{r} + \mathbf{R}_n^b, \tag{C.7a}$$

$$\frac{1}{L^3}\int_{L^3} \mathrm{d}^3 r \;\mapsto\; \frac{1}{N}\sum_{n=1}^{N}\int_{l^3}\frac{\mathrm{d}^3 r}{l^3}, \tag{C.7b}$$

where $\mathbf{R}_n^b = n\mathbf{R}^b$, where $\mathbf{R}^b$ is the Bravais lattice vector. We then have

$$\langle \psi_{c,\mathbf{k}+\mathbf{Q}} | e^{i\mathbf{K}\cdot\mathbf{r}}\hat{\mathbf{p}} | \psi_{v,\mathbf{k}}\rangle = \frac{1}{N}\sum_{n=1}^{N} e^{i(\mathbf{K}-\mathbf{Q})\cdot\mathbf{R}_n^b}\int_{l^3}\frac{\mathrm{d}^3 r}{l^3} u_{c,0}^*(\mathbf{r})(\hbar\mathbf{k}+\hat{\mathbf{p}})u_{v,0}(\mathbf{r}). \tag{C.8}$$

We have the expression of Kronecker delta $\frac{1}{N}\sum_{n=1}^{N} e^{i(\mathbf{K}-\mathbf{Q})\cdot\mathbf{R}_n^b} \sim \delta_{\mathbf{K},\mathbf{Q}}$. In the limit of infinite sheet of TMD, we can transform the Kronecker delta into Dirac delta, $\delta_{\mathbf{K},\mathbf{Q}} \mapsto \delta(\mathbf{K}-\mathbf{Q})$. We now revert the approximation of Eq. (C.5) to obtain

$$\begin{aligned}
\frac{\mathrm{d}^3 r}{l^3} u_{c,0}^*(\mathbf{r})(\hbar\mathbf{k}+\hat{\mathbf{p}})u_{v,0}(\mathbf{r}) &\sim \int_{l^3} \mathrm{d}^3 r \psi_{c,\mathbf{k}+\mathbf{Q}}^*(\mathbf{r})(\hbar\mathbf{k}+\hat{\mathbf{p}})\psi_{v,\mathbf{k}}(\mathbf{r}) \\
&= \int_{l^3} \mathrm{d}^3 r \langle u_c(\mathbf{k}+\mathbf{Q})|\mathbf{r}\rangle(\hbar\mathbf{k}+\hat{\mathbf{p}})\langle \mathbf{r}|u_v(\mathbf{k})\rangle \\
&= \langle u_c(\mathbf{k}+\mathbf{Q})|\hbar\mathbf{k}|u_v(\mathbf{k})\rangle + \langle u_c(\mathbf{k}+\mathbf{Q})|\hat{\mathbf{p}}|u_v(\mathbf{k})\rangle \\
&= \langle u_c(\mathbf{k}+\mathbf{Q})|\hat{\mathbf{p}}|u_v(\mathbf{k})\rangle,
\end{aligned} \tag{C.9}$$

as $\langle u_c(\mathbf{k})|\hbar\mathbf{k}|u_v(\mathbf{k})\rangle = \hbar\mathbf{k}\langle u_c(\mathbf{k}+\mathbf{Q})|u_v(\mathbf{k})\rangle = 0$, as the band wavefunctions are orthogonal with respect to band n. By the example of Ref. [29], if we expand $u_c(\mathbf{k}+\mathbf{Q})$ into series, and neglect the weakest term in the series, we arrive in the electric dipole approximations of the interaction Hamiltonian terms:

$$\langle \psi_{c,\mathbf{k}} | e^{i\mathbf{K}\cdot\mathbf{r}}\hat{\mathbf{p}} | \psi_{v,\mathbf{k}}\rangle \sim \delta(\mathbf{K}-\mathbf{Q})\langle \psi_{c,\mathbf{k}}|\hat{\mathbf{p}}|\psi_{v,\mathbf{k}}\rangle. \tag{C.10}$$